EVALUATING THE RATE

OF LEAKAGE THROUGH DEFECTS

IN A GEOMEMBRANE

A Thesis Submitted to the College of

Graduate and Postdoctoral Studies

In Partial Fulfillment of the Requirements

For the Degree of Master of Science

In the Department of Civil, Geological, and Environmental Engineering

University of Saskatchewan

Saskatoon

By

HALEY LOUISE CUNNINGHAM

Permission to Use

In presenting this thesis/dissertation in partial fulfillment of the requirements for a Postgraduate degree from the University of Saskatchewan, I agree that the Libraries of this University may make it freely available for inspection. I further agree that permission for copying of this thesis/dissertation in any manner, in whole or in part, for scholarly purposes may be granted by the professor or professors who supervised my thesis/dissertation work or, in their absence, by the Head of the Department or the Dean of the College in which my thesis work was done. It is understood that any copying or publication or use of this thesis/dissertation or parts thereof for financial gain shall not be allowed without my written permission. It is also understood that due recognition shall be given to me and to the University of Saskatchewan in any scholarly use which may be made of any material in my thesis/dissertation.

Requests for permission to copy or to make other uses of materials in this thesis/dissertation in whole or part should be addressed to:

Department of Civil, Geological, and Environmental Engineering
57 Campus Drive
University of Saskatchewan
Saskatoon, Saskatchewan S7N 5A9 Canada

OR

Dean
College of Graduate and Postdoctoral Studies
University of Saskatchewan
116 Thorvaldson Building, 110 Science Place
Saskatoon, Saskatchewan S7N 5C9 Canada

Abstract

Geomembranes are impermeable barriers when they remain intact. However, there is potential for damage to occur during and after installation. The development of defects in a geomembrane is critical when evaluating a barrier system for quality control and quality assurance purposes. Tears and punctures are common defect types that have been evaluated extensively in literature.

The majority of experimental procedures to date used small-scale permeameters to develop empirical equations for flow through a defect. Thus it is difficult to firmly conclude the expected flow rate through defects in field-like conditions. The main objective of this research project was to evaluate flow through a geomembrane defect using a large-scale constant head apparatus.

A large-scale constant head apparatus was developed to allow for the measurement of flow through a geomembrane defect of known dimensions when overlain by soil. This research only evaluated flow rate through a defect with sand overlying the geomembrane. A zero pressure boundary condition was maintained by allowing the water to flow freely for collection, thus representing a system similar to that of a secondary drainage layer.

The specific objectives of the research were to: i) compile a database of experimental results obtained through the use of the large scale apparatus for various defect shapes and sizes, geomembrane thicknesses, and applied slopes; ii) develop 3D numerical model representative of the experimental geomembrane flow system to evaluate the underlying phenomena; iii) assess the effects of a geomembrane thickness and slope on the flow rate through the selected geomembrane defect; and iv) to provide correction factors for the selected defects based on experimental and numerical results.

The results of the physical model for circular defects were compared to both the applicable empirical solution and finite element models (FEM). A 2-dimensional axisymmetric FEM was developed as an approximation to the experimental results for circular defects without a horizontal hydraulic gradient or slope. A 3-dimensional FEM was developed for all geomembrane defects tested experimentally. Currently there are no empirical equations proposed for geomembrane systems with elongated defects or defects on a sloped geomembrane surface.

The experimental flow rates were most similar to the 3D FEM results, followed by the 2D FEM results, then Bonaparte et al.'s (1989) empirical estimations, respectively. Both of the finite element models and empirical estimations overestimated experimental flow rates through circular defects.

The 3D FEM models resulted in high localised hydraulic gradients immediately surrounding the defect. These findings support the assumption that the inconsistencies between the experimental results with the empirical and numerical estimations are due to high velocity, non-Darcian flow properties occurring immediately around the defect.

FEMs cannot examine the flow regimes occurring within the pore-spaces in the material immediately near the defect. Further examination is required to explicitly determine that the overestimation of flow rates between the experimental results and the empirical and numerical estimations is the result of high velocity, non-Darcian flow effects.

Acknowledgements

I would like to acknowledge my academic advisor Ian Fleming for providing me with guidance and assistance throughout my research. I would like to recognise my academic committee of Terry Fonstand and Lee Barbour for their encouragement and direction they provided.

In addition, I would like to thank Soil Vision and GeoSlope for providing me with the numerical modelling software I required for the completion of my master thesis.

Dedication

To Dexter and Henry.

Table of Contents

List of Tables

List of Figures

Chapter 1 Introduction

1.1 Background

Geomembranes are used in a variety of different applications including landfill barriers and liquid containment. An important consideration in regards to the use of geomembranes is the potential for damages during and after installation. Leakage through geomembranes occurs due to damages from imperfect seaming, tears, punctures, etc. (Touze-Foltz et al., 1999). Leakage through circular, square, and tear-like, slit, or elongated defects are typically analyzed for the advective flow disregarding permeation through the geomembrane itself.

A number of empirical solutions (Bonaparte et al., 1989; Giroud & Bonaparte, 1989a, 1998b; Giroud et al., 1992; Touze-Foltz and Giroud, 2003, 2005) have been developed to evaluate the flow rates through circular and elongated defects on flat horizontal geomembrane surfaces. Analytical solutions (Giroud et al., 1997c; Rowe and Booker, 1998; Touze-Foltz et al., 1999, 2001) have also been developed for various geomembrane systems.

Experimental procedures within literature typically use small-scale permeameters to measure the expected flow rate through a defect within a set system (Brown et al., 1987; Giroud & Bonaparte, 1989a, 1989b; Walton et al., 1997). Due to the lack of large-scale models supporting the empirical and analytical equations, it is difficult to conclude if these equations are representative of field results.

Factors affecting the rate of leakage through a defect are influenced by the configuration of the entire geomembrane-soil system. The characteristics of overlying and underlying material, contact condition between the geomembrane and underlying material interface, transmissivity of interface gap, size and shape of defect, roughness of defect edges, etc. are all parameters that have been evaluated for their effects on the flow rate through a geomembrane defect.

This research involves the use of a large-scale experimental model for a system with a geomembrane overlain by a permeable medium and underlain by a higher permeable medium. The apparatus consists of upstream and downstream compartments which allow for head to be held constant with the geomembrane-soil system in the large centre compartment. Consideration will

be given to four circular and two elongated defects of various size along with the analysis of the influence of geomembrane thickness. The apparatus allows for a slope to be applied to the system, allowing for the evaluation of the influence of slope on the resulting flow rates. Experimental results will be obtained and evaluated against the results of simulation obtained using 2D and 3D finite element numerical models.

1.2 Research Objectives

The overall objective of this work is to evaluate flow rates through geomembrane defects in a large-scale model and determine the cause of discrepancies between the current empirical equation and the experimental results achieved from the large-scale model. Experimental and numerical models will be part of the analysis. The experimental component of the work was completed using a large-scale constant head apparatus. The defect was positioned directly over a drain connected to a tube of water allowing for the bottom boundary condition of the defect to be set to a pressure head. Collecting the overflow water from this back pressure tube allows for a flow rate to be determined. Figure 1.1 shows a schematic of the experimental setup of the constant head apparatus.

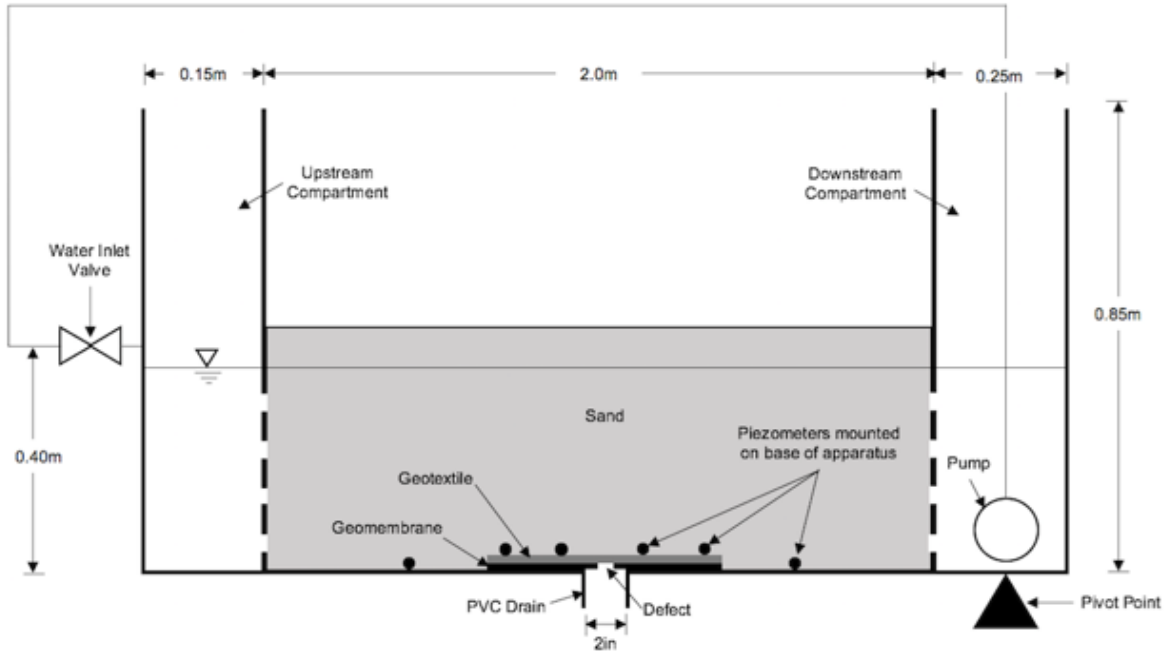

Figure 1.1 Schematic of large-scale constant head apparatus

2D and 3D finite element software will be used to numerically model the experimental results. This work was expected to lead to a better evaluation of the expected flow rates through geomembrane defects in field systems.

The project specific objectives are as follows:

1. To provide a database of experimental results of flow rates through the selected geomembrane defect shapes and sizes, geomembrane thicknesses, and applied slopes using the selected experimental system;
2. Develop 3D numerical model representative of the experimental geomembrane flow system to evaluate the underlying phenomena;
3. Assess the effects of a geomembrane thickness and slope on the flow rate through the selected geomembrane defect; and
4. To provide correction factors for the selected defects based on experimental and numerical results.

1.3 Scope

The purpose of this work is limited to evaluate flow rates through a defect in a geomembrane using experimental methods within a large-scale constant head apparatus and propose correction factors to allow for a more accurate estimation of flow. The primary focus of the work will be on circular defects on flat geomembrane surfaces with no applied slope or micro-topography. Secondary testing will analyse flow rates through elongated defects and investigate the influence of an applied slope and horizontal hydraulic gradient in the overlying material on the flow rate through a geomembrane defect. This work will consist of conducting a literature review, an experimental program and the completion of numerical modelling of simulated experimental results.

Work that was out of scope for this project was:

1. The determination of effects on the flow because of micro topography surrounding a defect and or the defect being located on a wrinkle;
2. The effects on the flow rates due to sand or other particles blocking the defect opening; and
3. The effects of different liquids on the flow rate.

1.4 Organization of Thesis

This thesis consists of five main chapters. Chapter 1 introduces the purpose of the research project. Chapter 2 consists of the literature review completed for the project. The methodology and procedures for the laboratory program and finite element modelling are discussed in Chapter 3. Chapter 4 presents the results obtained through the completion of the laboratory program. Chapter 5 summarizes the laboratory program findings and conclusions achieved through the completion of the research.

Chapter 2 Literature Review

2.1 Introduction

Chapter 2 discusses the past literature relevant to the research project. Proposed empirical solutions for flow through geomembrane defects are discussed for the various systems involving the permeability of overlying and underlying materials as well as defect characteristics. The corresponding analytical solution is discussed but is not subject to comparison to the experimental results.

Additional sections briefly discuss the current research completed on the analysis of effects of geomembrane slope, geomembrane thickness and the flow through porous media. No research has been completed on the influence on flow through a geomembrane defect that is located on a sloped surface. Minimal research has been completed on analyzed the effect of geomembrane thickness on flow rates through defects. Most authors analyse the flow through a geomembrane defect assuming Darcy's law applies. However, no research has been completed on the potential influence on flow rate due to high velocity, non-Darcian flow occurring in the porous media immediately around the defect.

2.2 Flow through Geomembrane Defects

2.2.1 General

Current equations for analysing the flow rate through geomembrane defects are typically used to estimate the leakage conditions of liner systems such as landfills. Within the literature, some equations are stated to be empirical. Meaning that the equations are derived and based on achieved experimental results. However, equations proposed by authors such as Giroud and Bonaparte (1989a, 1989b), Giroud et al. (1989, 1992), and Touze-Foltz and Giroud (2003, 2005) are not fully empirically based. Most are based on some experimental results along with either analytical or numerically based model results.

2.2.2 Current Empirical Equations

Past research for estimating flow through geomembrane defects was completed by many authors such as Giroud and Bonaparte (1989a, 1989b), Giroud et al. (1992, 1995, 1997b), Touze-Foltz and Giroud (2003, 2005). Literature has examined various geomembrane systems to analyse the influences of different components on the flow through a defect in a geomembrane. Geomembrane system refers to the composition of the geomembrane and the surrounding materials. Single-lined, double-lined, compacted clay layer with an overlying geomembrane, and composite liners are all examples of geomembrane systems.

The majority of authors have experimentally measured flow rates through a geomembrane system using small-scale permeameter-like apparatuses. Few authors such as Brown et al. (1987), Priyantha et al. (1988), and Chai et al. (2005) have completed experiments to analyse flow through geomembrane defects using large-scale apparatuses.

Characteristics of a geomembrane defect such as size and shape are important in estimated flow rate through a defect. Circular defects are most commonly analysed in literature. However, authors have also investigated flow rates through square, finite length (rectangular), and infinite length defects. Area of a defect is a common parameter within developed equations. Shape of a defect can dictate the method in which the flow rate is estimated. Bernoulli's equation for free flow through an orifice and radial flow calculations are commonly used for the development of non-linear flow equations for circular defects.

Giroud and Bonaparte first published research examining the flow rates through geomembrane defects. The research completed by Giroud and Bonaparte (1989a, 1989b) was conducted based on published and unpublished experimental data as well as some analytical studies on defect flow rates. Data presented in this study was based on the leakage of water through defects. Defects of various shape and size were evaluated by Giroud and Bonaparte (1989a, 1989b). Pinhole defects (small circular defects with diameters smaller than the thickness of the geomembrane) have flow characterized by Poiseuille's equation:

$$Q = \frac{\pi \rho g h_w d^4}{128 \eta T_g} \tag{2.1}$$

where Q is the flow rate (m^3/s), ρ is fluid density (kg/m^3), g is gravity (m/s^2), h_w is hydraulic head above geomembrane (m), d is pinhole diameter (m), η is dynamic fluid viscosity (kg/(ms)), and T_g is geomembrane thickness (m).

Large circular defects (defect area is greater than 1.0E-04) were considered to be governed by free orifice flows illustrated by Bernoulli's equation:

$$Q = Ca\sqrt{2gh_w} \tag{2.2}$$

where C is the sharpness coefficient related to edges of the orifice (value of 0.6 is recommend by authors for sharp edges), and a is area of the defect (m^2).

The validity of Bernoulli's equation is lost when the hydraulic conductivity of the soil underlying the geomembrane is less than approximately 10^{-3} m/s for small defect sizes, as the soil would then be limiting the leakage and free orifice flow would not apply (Brown et al., 1987). Thus influencing the development of the empirical equations for estimating flow through geomembrane defects placed on low hydraulic conductivity soils by Giroud and Bonaparte (1989).

Equations for infinite length and finite length or seam defects are typically developed through analytical methods (Priyantha et al., 1988; Giroud et al., 1992; Giroud, 1997). Touze-Foltz and Giroud (2003) present empirical equations for defects of infinite length (ratio of the length and width of the defect is large). Foose et al. (2001) and Giroud et al. (1992) proposed equations for seam defects for different contact conditions. Contact condition refers to the transmissivity between the geomembrane and the underlying material. Giroud and Touze-Foltz (2005) developed equations for infinite and finite length defects using empirical equations developed for circular defects in combination with previous analytical equations developed for uniform width and infinite length defects for composite liners.

Giroud et al. (1992) established equations for a range of hydraulic head in the case of a square, infinite length, and long (rectangular) defects placed on a layer of low permeability to form a composite system. The authors developed the analytical flow rate equations based on assumptions of the different defect shapes wetted area. Steady-state flow conditions and the material surrounding the defect being fully saturated were assumed.

Hydraulic head above the geomembrane defect is an important factor for estimating flow rate and is occasionally a limiting factor for the use of developed equations. The hydraulic head difference in which the geomembrane defect system is exposed, governs the flow rate through the defect (Giroud and Bonaparte, 1997a). Drawdown of hydraulic head caused by the defect is not typically considered within equations, rather the average hydraulic head above a defect is commonly used. The phreatic surface is typically assumed to be contained fully within the material overlying the geomembrane.

For the occurrence of a defect within a geomembrane, a depression in the phreatic surface above the defect is likely to occur due to the migration of fluid through the defect (Giroud et al., 1997b). When applying hydraulic head within an equation, assuming the hydraulic head immediately above and away from the geomembrane defect would result in an over estimation of flow rate through the defect (Giroud et al., 1997c). Figure 2.1 shows that the hydraulic head immediately above the defect is h_0 and hydraulic head away from the defect is h (h is out of the zone of influence of the defect causing the depression in phreatic surface).

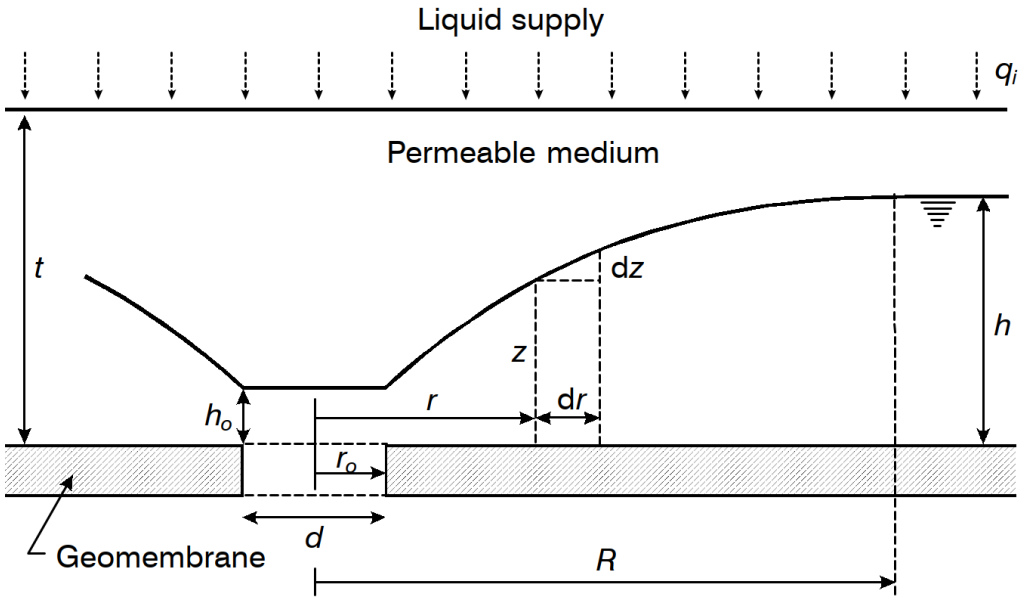

Figure 2.1 Definition of parameters (Giroud et al., 1997c)

Hydraulic characteristics of the materials overlying and underlying the geomembrane are critical factors that govern the flow rate through a geomembrane defect. Most authors have analysed how

the flow through a defect is influenced by the surrounding materials characteristics, such as hydraulic conductivity of the materials within the geomembrane system.

Bonaparte et al. (1989) indicate that high-permeable material above or below a geomembrane are expected to not have a significant effect on the leakage rate of a defect; flow can be estimated by assuming free flow through the defect. If the geomembrane is overlain by a medium-permeable material, flow towards the defect will be impeded and the flow rate will be less than assumed in a case with free flow.

The equation for a geomembrane system overlain by a medium-permeable material (such as sand or fine gravel) and underlain with a high permeable material (such as a geonet or coarse gravel) was developed by assuming the radial flow equation is the lower bound and Bernoulli's is used as upper bound solution. A satisfactory approximation could be made for flow rate based on averaging logarithms of leakage rates obtained from upper and lower bound solutions.

Thus Bonaparte et al. (1989) suggested the following equation:

$$Q = 3a^{0.75}h^{0.75}k_d^{0.5} \tag{2.3}$$

where k_d is hydraulic conductivity of the overlying soil (m/s), h is hydraulic head above the defect (m), and a is the area of the defect (m^2). For the results of this equation to be valid the hydraulic conductivity of the overlying drainage material should be greater than 10^{-6}m/s and the head over the geomembrane is less than the thickness of the overlying drainage material.

Many authors have investigated the influence of lower permeable medium underlying the geomembrane (Giroud, 1997; Rowe and Booker, 1998; Touze-Foltz et al., 1999; Touze-Foltz et al., 2001; Touze-Foltz and Giroud, 2005). Flow through geomembrane defects within a composite liner system are common due to the wide range of industrial applications of composite systems.

Flow within the surrounding porous material is typically assumed to be laminar and thus Darcy's equation is applicable (Giroud and Bonaparte, 1989a; Giroud et al., 1997a, 1997b, 1997c). Research regarding flow through geomembrane defects does not investigate the influence of potential turbulent flow effects within or surrounding a geomembrane defect.

Other factors such as edge roughness of the defect and contact condition between the geomembrane and underlying material have been analysed by authors. Edge roughness assumes that the edges of the defect are not perfectly smooth. Authors typically apply a factor to the equation to compensate for the influence of edge roughness. The contact condition factor for excellent contact was determined through the investigation of interface transmissivity equations initially proposed by Rowe (1998) and modified by Touze-Foltz and Giroud (2003). Similar to edge roughness, authors provide a range of values that can be applied to the equation depending on the contact condition that exists between the geomembrane and the underlying material.

2.3 Summary of the Analytical Equation for Flow through Geomembrane Defects with Overlying and Underlying Permeable Media

An analytical equation was proposed by Giroud et al. (1997c) for a defect in a geomembrane that is overlain and underlain by permeable media. This equation estimates the advective flow through a geomembrane defect for a system with an overlying material that is less permeable that the material underlying the geomembrane.

Giroud et al. (1997c) equation tends towards Bernoulli's equation for free flow through an orifice as the overlying materials hydraulic conductivity tends towards infinity. Bernoulli's equation can result in an overestimation of the flow rate through a defect. This is due to a depression in the phreatic surface surrounding the defect which is not taken into consideration when head is calculated in typical methods (Giroud et al., 1997c).

The resulting analytical equation was as follows:

$$h = \left\{ \frac{a\, q_i}{2\, k_{OM}\, \pi} + \frac{Q}{a\, q_i} \left[ln\ ln\ \left(\frac{Q}{a\, q_i} \right) - 1 \right] + \frac{1}{4\, g^2} \left(\frac{Q}{0.6\, a} \right)^4 \right\}^{1/2} \tag{2.4}$$

where *h* is hydraulic head at distance R (m), q_i is the supply rate of the liquid to the permeable media per unit area (m/s), k_{OM} is the hydraulic conductivity of the overlying material (m/s), *a* is area of the defect (m), and g is gravity (m/s^2). The analytical equation cannot be solved directly for flow rate through the defect and thus iterations must be completed to obtain Q when h, a, k_{OM}, and q_i are known.

Giroud et al. (1997c) developed graphical solutions to illustrate the results of the analytical equation for various defect sizes. At lower heads the flow rate is a function of a, k_{OM}, q_i, and $h^{1.85}$. As the head increases the flow rate as increases changes into a transition flow regime and finally converges to Bernoulli's equation.

In application of this analytical equation, for a given head, h, and hydraulic conductivity of the overlying material, k_{OM}, the flow rate through the defect, Q, will increase with increasing defect size. However, the defect size is only significant as the Q(h) curves approach Bernoulli's equation. At lower Q values where the h and k_{OM} are small the size of the defect is negligible.

2.4 Influence of Geomembrane Thickness on Flow through Geomembrane Defects

Geomembrane thickness has been one of the factors authors have evaluated for its influence on flow through geomembrane defects. Experimental testing with various types and thicknesses of geomembranes have been completed to evaluate the significance of geomembrane thickness on flow rate through a defect.

Some authors have found from their testing that the geomembrane thickness has little effect on the defect flow rate or other factors that were deemed significantly more influential than that of geomembrane thickness (Brown et al., 1987; Priyantha et al., 1988; Benson et al., 1995; Rowe et al., 2016).

Rowe et al. (2016) evaluated the effect of geomembrane thickness in a system with tailings overlying and silty sand or pea gravel underlying the geomembrane. The tailings material had lower permeability than that of the both underlying materials. Most of the testing was completed using a 1mm thick geomembrane and to evaluate thickness effects a 2mm geomembrane was used.

The flow rate achieved using the 2mm geomembrane was slightly lower than the average leakage rate for the 1mm geomembrane. However, the flow rate from the 2mm geomembrane test fell within the range of flow rates measured from the 1mm geomembrane tests (Rowe et al., 2016). Rowe et al. (2016) concluded that the geomembrane thickness has minimal effect on defect flow rate however due to insufficient data a firm conclusion of this effect could not be stated.

Walton and Sagar (1990) proposed an analytical solution for flow through circular defects developed using cylindrical and Cartesian coordinate system equations. The solution proposed for the effect of geomembrane thickness with a series of defects assuming saturated, steady-state flow conditions. Boundary conditions appropriate for the flow analysis completed by Walton and Sagar (1990) are a fixed head as the upper boundary of the defect and a fixed head at a distance from the defect.

The analyses were for a geomembrane overlays a compacted clay layer with relatively high permeable material above and below the geomembrane-compacted clay system. Figure 2.1 is a schematic for a thick geomembrane geometry. The schematic illustrates that head loss occurs entering or exiting the hole ($H_3 – H_2$) and head loss occurs within the stem of the defect ($H_2 – H_1$).

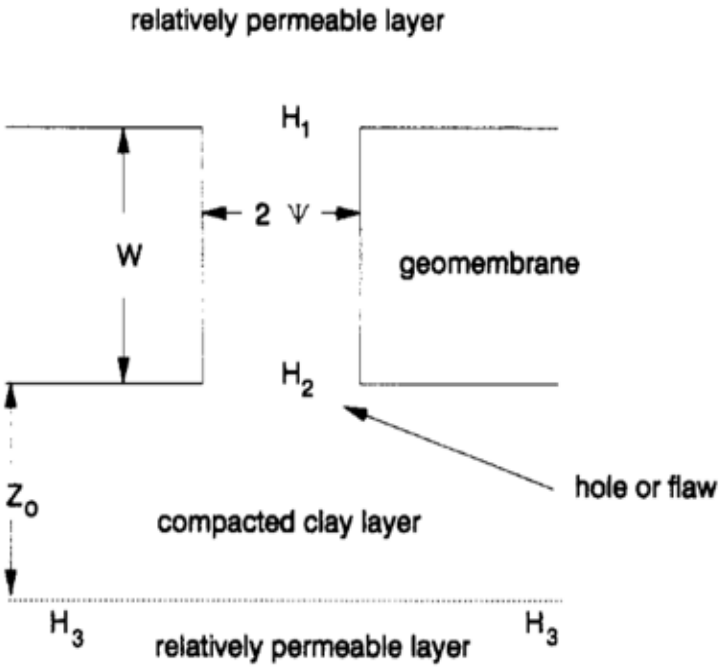

Figure 2.2 Schematic of thick geomembrane simulation geometry (Walton and Sagar, 1990)

Flow rates are reduced due to the resistance of flow occurring throughout the stem of the geomembrane defect (Walton and Sagar, 1990). Indicting that there will be a decrease in flow rate as the thickness of the geomembrane increases. Additionally, Walton and Sagar (1990) state that the significant of both size and shape of the defect decreases as the geomembrane thickness increases.

The equation developed by Walton and Sagar (1990) for a circular defect in a geomembrane of finite thickness was as follows:

$$q_t \cong \frac{1}{\frac{\omega}{\pi}+\frac{1}{q}} = \frac{Q}{(H_1-H_3)\psi K} \tag{2.5}$$

where q_t is the dimensionless flow rate for the finite thickness defect, q is the dimensionless flow rate for the infinitesimal thickness case defect, Q is the total flow rate through the defect (m^3/s), H_1 and H_3 are head values (m), $\omega = W/\psi$ where W is the finite thickness of the geomembrane and ψ is the defect radius, and K is the conductivity of the relatively high permeable material in the stem of the defect (m/s).

The equation for a slit defect in a geomembrane of finite thickness was developed based on the same assumptions as the circular defects. Walton and Sagar (1990) developed the following equation to approximate the total flow through a slit defect:

$$q_t \cong \frac{1}{\frac{\omega}{2}+\frac{1}{q}} = \frac{Q}{K(H_1-H_3)} \tag{2.6}$$

2.5 Influence of Slope on Flow through a Geomembrane Defect

Common applications of geomembranes such as landfill liners, embankment liners, tailings pond liners, etc. require the placement of the geomembrane liner on a slope. Few authors have analysed the effect of the slope on flow through a geomembrane defect.

The slope of the geomembrane is only taken into consideration in proposed equations for the calculation of hydraulic head above the defect (Giroud et al., 1992; Giroud et al., 1997a; Giroud et al., 1997c; Giroud, 1997). Giroud et al. (1997a) analyse the flow in leakage collection layers due to geomembrane defects on a slope. However, the authors used Bernoulli's equation to estimate the flow through the geomembrane defect and did not examine the effect of slope on the defect flow rate.

However, the effect of slope on the flow rate through a geomembrane defect has not been analysed. This research project will address this gap in knowledge with regards to the flow rate through a small circular geomembrane defect on various slopes.

2.6 Turbulent Flow

2.6.1 Non-Darcy Flow through Porous Media

Authors of empirical and analytical equations indicate the assumption that laminar flow, following Darcy's law, is occurring within the porous material surrounding the geomembrane defect (Bonaparte et al., 1989; Touze-Foltz, Rowe, & Duquennoi, 1999; Giroud & Bonaparte, 1989; Giroud, Khire, & Soderman, 1997; Walton et al., 1997).

Darcy's law governs the flow rate through porous media at low velocity and linear non-turbulent conditions. Darcy's law is as follows:

$$Q = -k \frac{dh}{dL} A \tag{2.7}$$

where Q is volumetric flow rate (m^3/s), k is hydraulic conductivity of the porous media (m/s), dh/dL is the hydraulic gradient over a distance of L, and A is the cross-sectional area of flow (m^2).

At higher velocities the flow within a porous media may experience non-Darcy flow. The onset of non-linear (turbulent) flow can be characterized through the use of the Reynolds number (Re). Chilton and Colburn (1931) completed experiments to evaluate the fluid flow through packed particles and redefined the Reynolds number for flow through porous media:

$$Re = \frac{\rho D_p \nu}{\mu} \tag{2.8}$$

where ρ is density of the fluid (g/cm^3), ν is the superficial velocity (cm/s), μ is fluid viscosity (Pa*s), and D_p is particle diameter (cm). Superficial velocity refers to the velocity of the fluid moving through the porous medium (Zeng and Grigg, 2006).

Reynolds numbers indicating the onset of turbulent flow regime is not the same among authors. Reynolds numbers between 1 and 10 are typically accepted as the onset of non-Darcy flow (dependent on grain size of porous media) (Fourar et al., 2004). Ma and Ruth (1993) used numerical analysis of the microscopic flow within porous media and found that the onset of turbulent flow occurs at a Reynolds number of approximately 10. Bear (1972) indicates that the Reynolds number for the beginning of turbulent flow is between 3 and 10.

Many authors have developed both analytical and empirical equations for determining the effects of non-Darcy effects on flow through porous media (Hassanizadeh and Gray, 1987; Ma and Ruth, 1992, 1993).

Both the Reynolds number and Forchheimer numbers can been used to evaluate turbulent flow regimes in porous media. Forchheimer (1901) proposed an empirical equation that takes into consideration the deviation from Darcy's law due to high Reynolds number.

$$-\frac{\Delta P}{L} = \frac{\mu}{K_f} V + \beta \rho V^2 \tag{2.9}$$

where ΔP is the pressure drop, L is the sample length, K_f is Forchheimer's permeability, β is the non-Darcy flow (inertial) coefficient, and V is Darcy's velocity.

Authors have varying opinions as to the cause of non-Darcy effects within a porous media. Hassanizadeh and Gray (1987) concluded that the onset of turbulent flows is caused by microscopic viscous forces. Whereas, Barak (1987) discusses the increase in Reynolds number due to the development of tortuous streamlines inside pores and the formation of local vortices caused by microscopic inertial forces. Many authors support this view of inertial forces being the cause of turbulent flow (e.g. Mei and Auriault, 1991; and Ma and Ruth, 1993).

Fourar et al. (2004) found that for 3D flow problems Forchheimer's (1901) equation is a good approximation when there are inertial effects occurring within a porous media. Zeng and Grigg (2006) found that a modified Forchheimer equation is a better way for evaluating fluid flow in non-Darcian situations based on findings made by Ma and Ruth (1993).

No authors have previously examined the effects of non-Darcian flow characteristics on the flow through a geomembrane defect. High flow velocity gradients occurring immediately around the defect would indicate the potential onset of non-Darcy flow.

2.6.2 Reynolds Number for Flow through a Defect in a Geomembrane

The application of Reynolds number has not be used by authors to analyse the flow regime that occurs through a defect in a geomembrane. Flow regimes can be identified through the calculation of a Reynolds number. The Reynolds number expression is a ratio of inertial forces to viscous

forces in the fluid. Reynolds number can be determined for flow through circular and non-circular pipes to identify laminar or turbulent flow regimes. As discussed in Section 1.6.1, Equation 2.22 is the expression to determine Reynolds number. For flow through a pipe the particle diameter in Equation 2.22 is substituted for the hydraulic diameter of the pipe.

$$Re = \frac{\rho D_h v}{\mu} \tag{2.10}$$

Where D_h is the hydraulic diameter (m). Hydraulic diameter of a circular pipe is equal to the diameter of the pipe. Non-circular pipes, such as a rectangular shaped pipe, has a hydraulic diameter of:

$$D_h = \frac{2ab}{a+b} \tag{2.11}$$

Where a is the width of the rectangle (m) and b is the length of the rectangle (m).

Reynolds number ranges can be separated into laminar, transitional, and turbulent flow regimes. Reynolds numbers for laminar flow is typically less than 2000, transition flow ranges from 2000 to 4000, and turbulent flow is typically greater than 4000 (De Nevers, 1991).

Chapter 3 Methodology

3.1 Introduction

A laboratory program was completed to determine the flow through geomembrane defects at a large-scale. After measuring the flow rates through numerous geomembrane defects with various controlled parameters (e.g. geomembrane size and shape, hydraulic head, hydraulic gradient, geomembrane thickness, and slope of a geomembrane) the results were compared with those of 2D axisymmetric and 3D finite element models (FEM). This chapter outlines the tests performed and procedures used to determine the properties of materials used and the experiments performed to measure flow rates through geomembrane defects.

3.2 Theory

3.2.1 Sieve Analysis

The grain size distribution of a material can be determined following the standard test method for particle size analysis of soil (ASTM D422). A sieve analysis allows for the evaluation of the distribution of particle sizes larger than 75µm. Determining the gradation of the particles smaller then 75µm is completed through a sedimentation process using a hydrometer. Gradation is an important property that can indicate physical and hydraulic characteristics of the material.

3.2.2 Water Retention Curve

Unsaturated characteristics of a material can be estimated through the use of a water retention curve (WRC). The WRC is expressed as a function of the desaturation dependent on pore-size distribution. A WRC illustrates the relationship between volumetric water content and matric suction of a material (Fredlund & Xing, 1994).

Van Genuchten (1980) proposed a closed form solution of the relationship between suction and volumetric water content which is commonly used to estimate the WRC of a material.

$$\theta = \theta_r + \frac{(\theta_s - \theta_r)}{[1+(\alpha\psi)^n]^m} \quad (3.1)$$

Where:

θ = volumetric water content;

θ_r = residual volumetric water content;

θ_s = saturated volumetric water content;

ψ = soil suction value (kPa);

α = fitting parameter related to the air-entry value of the material (1/kPa);

n = fitting parameter related to slope at the inflection point of desaturation; and

m = fitting parameter related to the functions curvature at high suctions ($m = 1 - 1/n$).

Using the Van Genuchten equation, a curve can be fitted to match the drying or wetting curve from experimental data for a material. The major soil parameters of air-entry value, residual and saturated water contents can then be estimated.

Fredlund and Xing (1994) proposed a closed form solution for characterizing WRC for soils. This solution is more suitable than the Van Genuchten (1980) when developing WRC's for soils with higher suction properties due to the upper limit of the solution; where the suction reaches 10^6kPa the volumetric water content is zero (Fredlund & Xing, 1994).

$$\theta = \theta_s \left[\frac{1}{\ln\left[\exp(1) + \left(\frac{\psi}{a}\right)^n\right]} \right]^m \tag{3.2}$$

Figure 3.1 illustrates a general water retention curve and where the major parameters correspond to on a WCC.

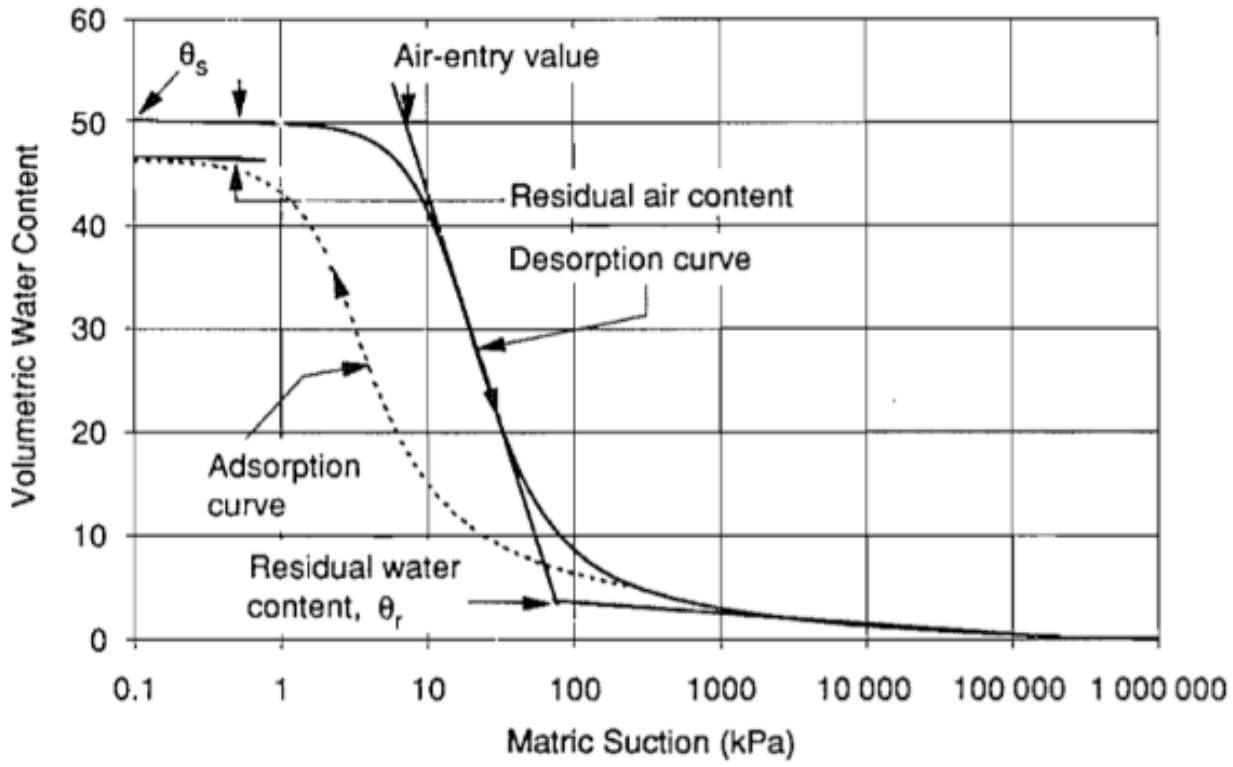

Figure 3.1 Water retention curve (Fredlund & Xing, 1994)

3.2.3 Constant Head Permeameter Test

The constant head permeameter test is based on Darcy's law. In which the hydraulic conductivity of a material can be determined by measuring a flow rate through a material of known area and determining a hydraulic head distribution profile throughout the permeameter cell.

$$q = k\, i\, A \tag{3.3}$$

Where:

q = flow rate of a liquid (m^3/s);

k = hydraulic conductivity or coefficient of permeability (m/s);

i = hydraulic gradient (m/m); and

A = cross-sectional area of material (m^2).

The hydraulic gradient is calculated using:

$$i = \frac{\Delta h}{L} \tag{3.4}$$

Where:

Δh = total head loss across a given length of the test specimen (m); and

L = given length over which the total head loss occurs (m).

3.2.4 Gradient Ratio Test

The gradient ratio test is based on the performance of the soil-geotextile system. This test examines the change in permeability of a soil-geotextile interface over a range of applied hydraulic gradients following ASTM D5101. The determination of a gradient ratio is completed through comparing the hydraulic gradient across the geotextile to that of the sand.

$$i_{m-n} = \frac{h_m - h_n}{l_{n-m}} \tag{3.5}$$

Where:

h_m = hydraulic head on piezometer 'm' (m);

h_n = hydraulic head on piezometer 'n' (m); and

l_{n-m} = length of soil between manometers being analyzed (m).

The gradient ratio is then calculated by:

$$GR = \frac{i_{1-2}}{i_{2-3}} \tag{3.6}$$

Where:

i_{1-2} = gradient across the geotextile (m/m); and

i_{2-3} = gradient across the soil (m/m).

If the gradient ratio of the system is greater than 1 then clogging is occurring in the geotextile and if it is less than 1 then piping is occurring through the geotextile.

3.3 Sizing of Geotextile

A non-woven needle punched geotextile was used in the large-scale constant head apparatus to separate the sand and geomembrane. Tests were completed with different sizes of geotextile to evaluate the potential influence of geotextile size on flow through the geomembrane defect. This was evaluated to ensure the geotextile does not cause any observer effects.

Trials were completed with geotextiles of size 10cm by 10cm, 25cm by 25cm, and 50cm by 50cm being placed over the geomembrane. Trials where completed both with the geomembrane flat and with a slope of approximately 1.0%.

3.4 Control Tests for Sand

Control tests were completed at the beginning of testing for each geomembrane defect. The control test consisted of measuring the hydraulic conductivity of the sand within the large-scale constant head apparatus. This was completed to ensure that the hydraulic conductivity of the sand was consistent between tests and potential effects such as layering when sand was placed in the large-scale apparatus did not influence the materials conductivity.

The sand was initial saturated by filling the upstream and downstream compartments of the apparatus with water until the sand was saturated to a few centimeters below the surface. Thus minimizing the amount of unsaturated flow and ensuring all the flow occurred within the sand and not above the surface of the sand.

The apparatus was placed on a slight slope (2.5%) to encourage the flow to move from the upstream compartment to the downstream compartment where it was allowed to drain from the outlet tube and be collected. The water collected over a set amount of time was then turned into a flow rate to allow for a hydraulic conductivity to be determined. Water was pumped into the upstream compartment at a flow rate that allowed for a constant head to be maintained.

Head measurements were recorded at the upstream and downstream compartments for each trial to determine the head difference across the sand. Manometers were used to take head measurements within the sand to allow for the evaluation of the head distribution throughout the sand.

3.5 Laboratory Program using the Large-Scale Constant Head Apparatus

3.5.1 Experimental Design

The experimental design involved the determination of experimental testing requirements to allow for all project objectives to be achieved. Experiments were designed to allow for the measurement of flow rates in response to different selected factors. These factors include defect dimensions (size and shape), hydraulic head, hydraulic gradient, slope, and geomembrane thickness. The selected experimental testing trials allowed for the different factors to be isolated and their influences to be determined. The primary tests evaluated flow through circular defects on a flat geomembrane.

The various geomembrane defect sizes where tested with the same set of experimental trials using 60mil smooth geomembrane. These trials consisted of five different target hydraulic heads and three horizontal hydraulic gradients. This set of testing allowed for the determination of the effect of defect dimensions, hydraulic head, and hydraulic gradient.

These trials were also applied to the tests involving the evaluation of flow through a 0.0050m diameter defect with geomembrane thicknesses of 80mil and 120mil. This allowed for the evaluation of the effects of geomembrane thickness on flow rate.

Secondary testing was completed on a circular defect with an applied slope and small hydraulic heads and two rectangular (elongated) defects using the same set of testing as the primary trials with no slope. A circular defect diameter of 0.0050m was used for the slope trials. Allowing for a comparison to the primary tests and the effects of an applied slope.

Elongated defects were selected to represent a seam-like defects. The same set of trials used in the primary tests were used for these elongated defects. Thus, allowing for the effects of hydraulic head and horizontal hydraulic gradient on flow rate through this type of defect to be determined.

The following section describes the procedure for setup of the experimental trials and how the experiments were carried out in the large-scale constant head apparatus.

3.5.2 Apparatus Design and Assembly

The experimental apparatus was designed at the University of Saskatchewan (Figure 3.11). This apparatus is approximately 2.5m long, 1.8m wide, and 1.5m high. There are three main compartments an upstream, downstream, and central compartment. The two end compartments allowed for the desired hydraulic head above the geomembrane defect to be set. The central compartment contained the geomembrane defect, geotextile, and sand system.

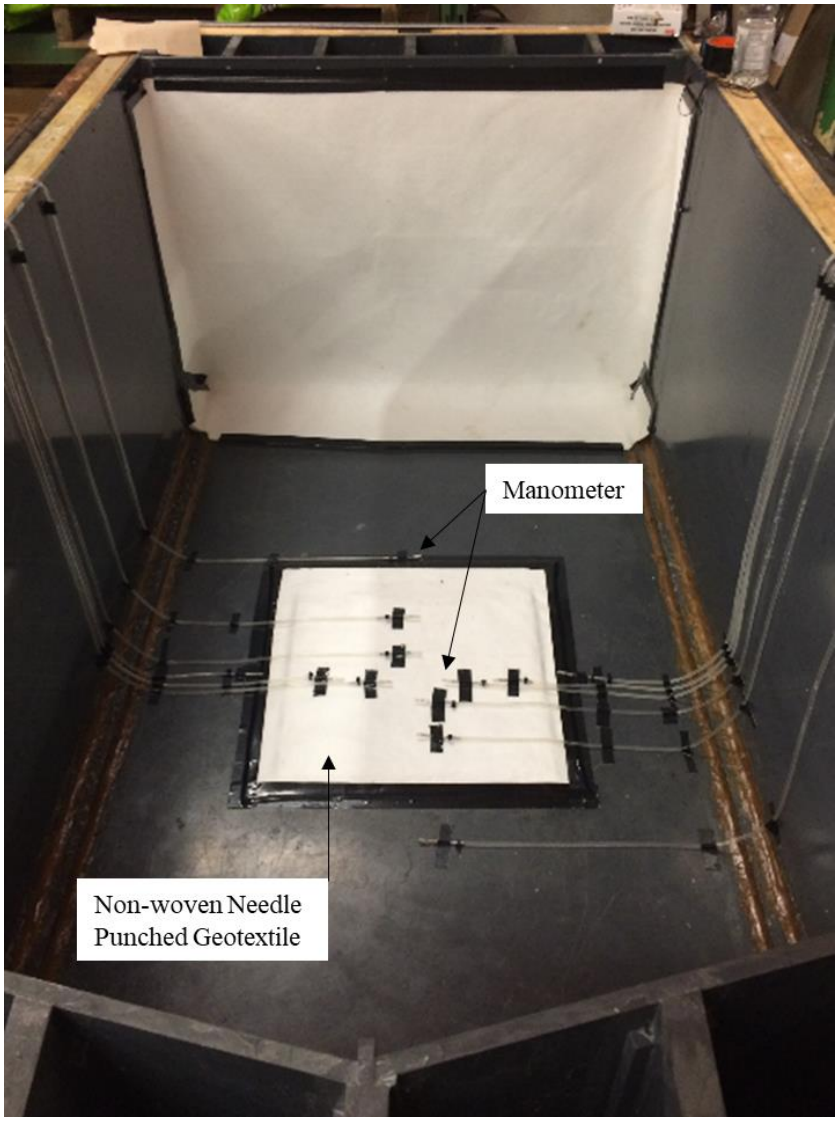

Figure 3.2 Large-scale constant head apparatus

The geomembrane was cut to a size of approximately 18in by 18in where the select defect was located at the centre of the geomembrane. The defect was then secured to the base of the apparatus

with silicon and position as such over the drain and the metal support bars to allow the edges of the defect to be supported but not interfere with the flow. A piece of non-woven needle punched geotextile that was larger than the geomembrane was then secured over top of the geomembrane using tape.

Circular holes were created in the geomembrane using an electric drill with the selected drill bit size. Elongated defects were created using the Epilog Laser Fusion cutter at the University of Saskatchewan were the correct size of defect was specified and slowly cut into the geomembrane.

Attached to the drain under the apparatus was a two-inch cap with a pipe fitting drilled connecting to a 1in tube. The height of this outlet tube was then set at the same height as the geomembrane defect. This was done by using a laboratory stand and clamp to hold the tube and allow the water to freely drain. During testing this tube was completely filled with water and the overflow was collected to measure the flow rate through the defect.

Twelve manometers were taped at various distances around the defect to allow for the measurement of hydraulic heads surrounding the defect (as seen in Figure 3.11). The manometers (Figure 3.12) consisted of 1/8in stiff tube connected to a small stainless-steel tube connected to another length of 1/8in tubing. The 1/8in clear tube secured to the base of the apparatus has a piece of tore nonwoven geotextile placed loosely in the end to prevent clogging with sand as well as not interfere with hydraulic head measurements.

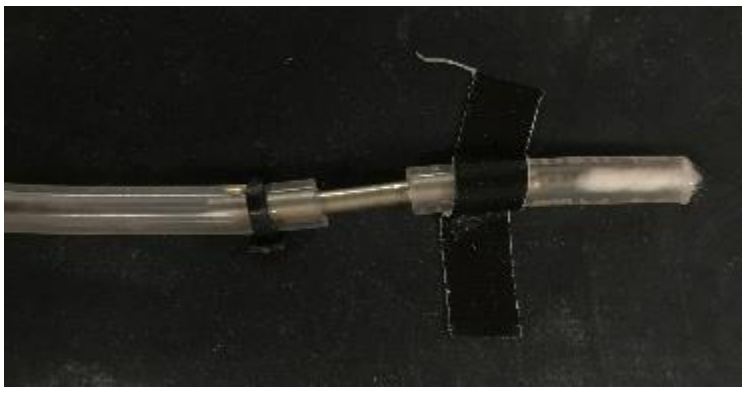

Figure 3.3 Manometer end used to measure experimental hydraulic head

The manometers were attached to two manometer boards. The 1/8in tubing is connected at the manometer board with larger 9/16in tubing to ensure capillary effects are minimal in the

manometer board measurements; capillary rise within the 9/16in tubing was calculated to be approximately 0.002m.

To complete the assembly of the apparatus, sand was placed into the central compartment to a depth of approximately 0.40m. A pump was located in the downstream compartment to move water to the upstream compartment when a hydraulic gradient was required. At the end of the hose attached to the pump there was a gate valve to set the needed flow rate to maintain a constant hydraulic head and gradient.

At the downstream end of the apparatus there is a pivot point. This allows for the upstream end to be raised to a selected height causing the system to be sloped.

3.5.3 Initial Conditions

The initial conditions for the tests were kept the same between experiments to ensure consistency for results. After assembly, water was pumped into the two end compartments to allow the sand to saturate from the bottom upwards. Testing was separated into three sets of testing; one for each of the three hydraulic gradients.

At the beginning of each set of testing, the sand was saturated to a hydraulic head of approximately 0.30m. Then water was pumped out of the end compartments in descending order of hydraulic head (i.e. starting at 0.30m then 0.25m, 0.20m, 0.15m, and ending at 0.10m). This was then repeated for the next two sets of testing with different hydraulic heads.

3.5.4 Boundary Conditions

The boundary condition at the bottom of the defect was a pressure head. A pressure head of 0.0m was applied for all the defect sizes. The 0.025m diameter defect was tested with three different back pressures at this boundary (0.0m, 0.02m, and 0.05m).

The two ends of the apparatus connected to the upstream and downstream compartments are constant head boundaries. The end compartments set the hydraulic head at either end of the apparatus. The other two sides and the base of the apparatus are considered no flow boundaries.

3.5.5 Testing Procedure

Both the end compartments were initially set to a head of 0.30m at the beginning of each set of trials. Table 3.3 illustrates the trials for each of the three testing sets. Trial 11 was not able to be completed for most defect sizes with a back pressure of 0.0m due to limitations of apparatus with required hydraulic head.

Table A Outline of testing for circular and elongated defects with a flat geomembrane

Testing Set	Trial No.	Hydraulic Gradient (m/m)	Hydraulic Head over Defect (m)
1	1	0.000	0.100
	2	0.000	0.150
	3	0.000	0.200
	4	0.000	0.250
	5	0.000	0.300
2	6	0.025	0.100
	7	0.025	0.150
	8	0.025	0.200
	9	0.025	0.250
	10	0.025	0.288
3	11*	0.075	0.100
	12	0.075	0.150
	13	0.075	0.200
	14	0.075	0.250
	15	0.075	0.300

* Note: Trial no. 11 could not be completed.

For testing set 1, the hydraulic head was lowered by using pumps in both end compartments. Testing sets 2 and 3 used only one pump in the downstream compartment to remove water. The downstream compartment was pumped and set at the desired hydraulic head. The upstream hydraulic head was allowed to lower and create the chosen hydraulic gradient. Once the upstream hydraulic head was reached, the water being pumped from the downstream end was diverted to the upstream compartment to allow for the desired constant head to be maintained in both end compartments.

The hydraulic head within the system was allowed to reach equilibrium prior to the beginning of flow rates being measured. For the tests with a hydraulic gradient, the pumping rate was set to

allow for equilibrium to be reached. This was monitored using the manometers placed at the base of the apparatus. Once these measurements stabilized at the appropriate head the flow rate measurements began.

The same testing procedures and sets of testing trials were done for the secondary testing of the elongated defects. The circular defect with an induced slope used a different set of hydraulic heads with the same procedures as described above with an applied slope. The slope was applied by using a hydraulic jack to raise the upstream end of the apparatus.

3.6 Numerical Modelling Program

3.6.1 Introduction

Numerical modelling was completed to allow for a comparison with the experimental results. The numerical finite element models allowed for the evaluation of parameters, such as hydraulic gradients immediately around the defect, that were not able to be measured experimentally. FEMs were completed in 2-dimensions and 3-dimensions using GeoStudio (2016) and SoilVision (2017) software solvers SEEP/W and SVFLUX/GE, respectively.

The 2D finite element models could only be used to develop an axisymmetric system for estimating the flow rate through a defect in a geomembrane. Axisymmetric conditions were never tested experimentally. However, the axisymmetric models were used as an approximation to allow for the comparison of the experimental results to 2D numerical model estimations.

3.6.2 2-Dimensional and 3-Dimensional Numerical Modelling Theory

3.6.3 General

Numerical models were developed to simulate the flow through geomembrane defects using 2D axisymmetric and 3D FEMs. The 2D axisymmetric models were developed in SEEP/W and SVFLUX/GE. The 3D models were developed in only SVFLUX/GE.

The SEEP/W software is a 2D steady-state or transient FEM that allows for the analysis of flow through porous media in unsaturated and saturated conditions. The SVFLUX/GE software is a

steady-state or transient FEM that allows for similar analysis as SEEP/W with the capability of both 2D and 3D analysis. Model inputs are summarized in the following theory.

3.6.4 GeoStudio: SEEP/W

3.6.4.1 Material Inputs

There are two required material input functions for the SEEP/W finite element models: volumetric water characteristic curve and hydraulic conductivity function.

The input functions were either measured through laboratory testing or estimated within the modelling software through known functions and properties. Measured functions allow for a higher degree of accuracy within the models; however, unknown parameters should be estimated and not ignored within the model.

Unknown functions can be estimated through the input of a known or predicted grain size distribution curve, with additional input parameters of saturated volumetric water content and the coefficient of volume compressibility. After these parameters are input into the model, the volumetric water characteristic curve and hydraulic conductivity function can be input or estimated if required. Anisotropy of the materials hydraulic conductivity can be taken into consideration in the model.

The prediction of a materials hydraulic conductivity function can be completed with the known input parameter of saturated hydraulic conductivity, which was measured in the laboratory for the sand and geotextile. There are two options for estimating this function within SEEP/W, which are Fredlund and Xing (1994) and van Genuchten (1980).

3.6.4.2 Boundary Conditions

Boundary conditions are required to be input for a defined mesh region within the FEM. Allowable hydraulic boundary conditions are total head, pressure head, total flux, unit flux, and unit gradient. A unit flux condition was applied to the no flow boundaries on the two length-wise sides of the model to represent the sidewalls of the test apparatus. A constant head condition was applied to the other two opposing ends within the model to represent the applied head in the upstream and

downstream reservoirs. A pressure head condition was used in the FEM at the surface of the defect to represent the freely draining outlet below the geomembrane defect.

3.6.5 Soil Vision: SVFLUX/GE

3.6.5.1 Material Inputs

Input requirements for materials are similar to those needed for the SEEP/W models. Saturated input conditions of saturated volumetric water content and specific gravity are required. A volumetric water characteristic curve can be estimate using various estimation functions (e.g. Fredlund and Xing (1994), van Genuchten (1980), van Genuchten and Mualem (1984), and Brooks and Corey (1971)). A function can be estimated by providing the required user inputs or inputting laboratory data and fitting it to the selected estimation function.

An unsaturated hydraulic conductivity function can be completed through the required known input of saturated hydraulic conductivity. The unsaturated hydraulic conductivity can then be estimated using the same fitting function used for the volumetric water characteristic curve. Anisotropy of a material can be specified within the model.

3.6.5.2 Boundary Conditions

The 2D axisymmetric and 3D SVFLUX/GE FEMs use the same boundary conditions as applied in the SEEP/W software.

3.6.5.3 Initial Conditions

For a steady-state analysis, SVFLUX/GE requires an initial head input. The initial head value can be input in a variation of ways. The initial head can be input as a constant value, a grid over the desired region, an expression, or a water table. For the 2D axisymmetric and 3D numerical models a constant input value was used.

3.7 Analysis of Mesh Refinement and Scaled-Up Finite Element Model

3.7.1 Mesh Spacing Refinement

Mesh spacing should be appropriately refined based on model specific parameters and output requirements. Mesh refinement increases the number of nodes for the specified area. Increasing

mesh density for a region will aid in model convergence and accuracy (SoilVision Systems Ltd., 2007).

Mesh refinement was completed for both 2D and 3D finite element models to ensure numerical stability within the models and increase accuracy for the estimated flow rates. Mesh spacing was refined for the geomembrane defect region and the immediate surrounding area within the numerical models. Mesh spacing was gradually refined around the defect to examine when the flow rate converged and no instability within the results occurred. 2D and 3D finite element models required different mesh spacing.

The 2D FEMs mesh spacing was simpler than the 3D models. The two software's used for the 2D models resulted in similar mesh spacing requirements. This mesh spacing was completed by analyzing gradients immediately around the geomembrane defect. The mesh spacing was reduced until the gradient profiles within the 2D FEMs were no longer changing with further mesh refinement. Thus, indicating that there was no numerical instability within the model and the flux rates had converged. Both 2D FEM software's required a mesh spacing of approximately 0.00025m surrounding the defect region. Figure 3.4 illustrates a cross-section the regions created within the 2D FEMs to allow for specification of maximum mesh spacing and better convergence within the model.

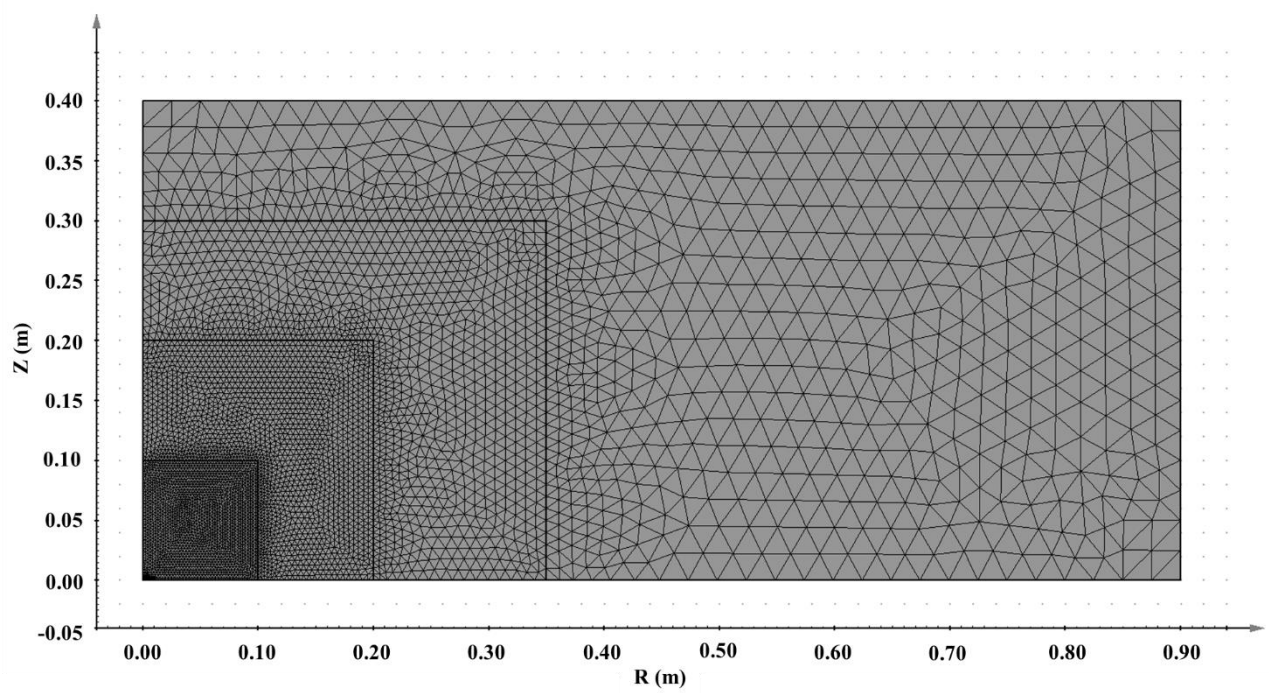

Figure 3.4 2D axisymmetric finite element model mesh distribution (Soil Vision, 2018)

The SoilVision software used for the 3D has automatic mesh refinement, thus the mesh around the defects were automatically refined within each model. However, further manual mesh refinement was required around the defect. Manual input of a mesh spacing for a specific region sets the maximum node spacing that will occur within that boundary (SoilVision Systems Ltd., 2007). Mesh refinement for the 3D FEMs was more difficult than 2D mesh refinement due to the small defect sizes and increased mesh complexity. The various models, circular and elongated defects on flat geomembrane surfaces, required different mesh refinement.

The circular defects on flat geomembrane surfaces were refined to a maximum mesh spacing of 0.0008m. Elongated defects were able to be refined to a maximum mesh spacing of 0.0005m. Figure 3.5 illustrates an overview of the regions created within the 3D FEMs to allow for specification of maximum mesh spacing to be refined closer to the defect. The circular defect on a sloped geomembrane surface were modelled through scaling-up the FEMs due to difficulties in refining the mesh. In addition, circular and rectangular defects on flat geomembrane surfaces were scaled-up to ensure that the meshing was properly refined due to difficulties with the experimentally scaled FEMs.

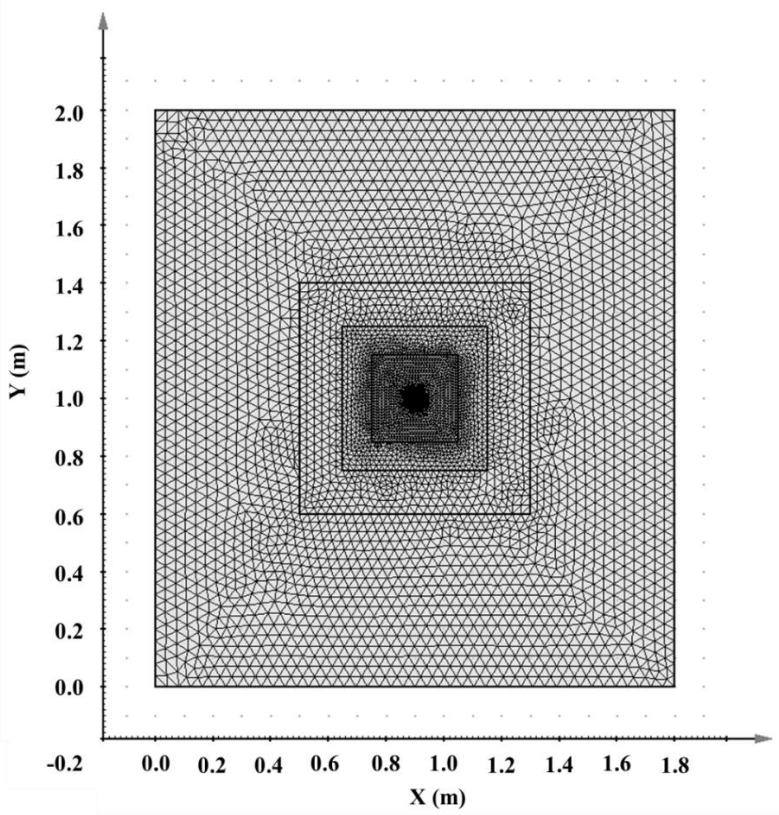

Figure 3.5 3D finite element model mesh distribution (Soil Vision, 2018)

3.7.2 Scaled-Up Finite Element Models

The 3D mesh refinement was difficult due to the small size of the selected defects. Scaled-up models were developed to assist in increasing the accuracy of the 3D models. The scaled-up models allowed mesh refinement to be completed more easily. In addition, the scaled-up FEMs allowed for a comparison between the experimentally scaled FEMs.

This was completed by scaling-up all dimensions by a factor of 10. As a result, a defect of diameter 0.005m was modelled as 0.05m and a head of 0.10m at a boundary condition was then modelled as 1.0m. Material characteristics in the finite element models were not changed. The output flux result from the model then needs to be scaled-down by a factor of 100.

Circular and elongated defects on flat geomembrane surfaces were refined to a maximum mesh spacing of 0.005m and 0.008m, respectively. Circular defects on sloped geomembrane surfaces

were refined to a maximum mesh spacing of 0.005m. Scaled-up models resulted in similar FEM results as the experimentally scaled models which is discussed in Chapter 4.

3.8 Error Calculations

Experimental results are compared to Bonaparte et al. (1989) proposed empirical solution and the FEM estimations. Different equations were used when comparing the experimental results to the semi-empirical estimates and the finite element results.

Percent error calculations can be used to determine the difference between an experimental and theoretical value. When comparing the experimental and finite element results, the following percent error calculation was used:

$$Percent\ Error = \frac{Experimental - Theoretical}{Theoretical} * 100\% \tag{3.6}$$

where the experimental value is the measured value and the theoretical value is the accepted or 'correct' value. Negative percent errors indicate that the theoretical value overestimates the flow rate in comparison to the experimental results, and vice versa.

When the experimental results were compared to the results of the semi-empirical equation proposed by Bonaparte et al. (1989), the following equation was used:

$$Correction\ Factor = \frac{Experimental}{Theoretical} * 100\% \tag{3.7}$$

where the experimental value is the measured value and the theoretical value is the semi-empirical estimation. This equation provides the ratio between the experimental and Bonaparte et al.'s (1989) estimated flow rates. The apparent correction factors better illustrate the relationship between the two flow rates.

A percent difference calculation can be completed when either two experimental or two theoretical values are being compared. Neither value is deemed the actual or 'correct' value. The percent difference calculation is the difference between the two values divided by the arithmetic mean.

$$Percent\ Difference = \frac{|x_1 - x_2|}{\frac{(x_1 + x_2)}{2}} * 100\% \tag{3.8}$$

where x_1 and x_2 are the two values that are being compared.

3.9 Chapter Summary

This chapter described the laboratory program used for the required experimental research. Characteristics of both the sand and geotextile used in the large-scale experiments were determined through completing various laboratory experiments. The assembly of the apparatus along with the applicable initial and boundary conditions were described. Finite element modelling procedures and inputs were outlined in this chapter.

The next chapter discusses the results obtained from the completion of the laboratory program and the finite element modelling. The experimental results are compared to both the empirical solution and analyzed in comparison to the FEMs.

Chapter 4 Presentation of Results & Analysis

4.1 Introduction

This chapter presents the results found through the completion of the laboratory program. Material properties measured during the laboratory analysis are presented in this chapter. Data for circular and elongated (rectangular) defects on a flat geomembrane and a circular defect on sloped geomembranes are shown. The effects of hydraulic head above the defect, horizontal hydraulic gradient across the system, and geomembrane thickness on flow rate through a defect are evaluated. In addition, the influence of sloping of the geomembrane surface on flow through a geomembrane defect was analysed.

The experimental results are compared to the proposed empirical equation by Bonaparte et al. (1989) and developed 2D and 3D finite element model (FEM) estimations for flow through a defect in a geomembrane. The empirical solution is only applicable to circular defects on a flat geomembrane surface.

4.2 Selection of Material

This section outlines the material properties found by the completion of the laboratory program for the sand and geotextiles used for the experimental testing.

4.2.1 Sand Material Properties

4.2.1.1 Sieve Analysis

A sieve analysis was completed to determine the grain size distribution of the sand used for experimental testing. The selected sand was a 40-60 sand mixture where majority of the sand was between 0.425 and 0.250mm in diameter. Figure 4.1 is an illustration of the grain size distribution of the material.

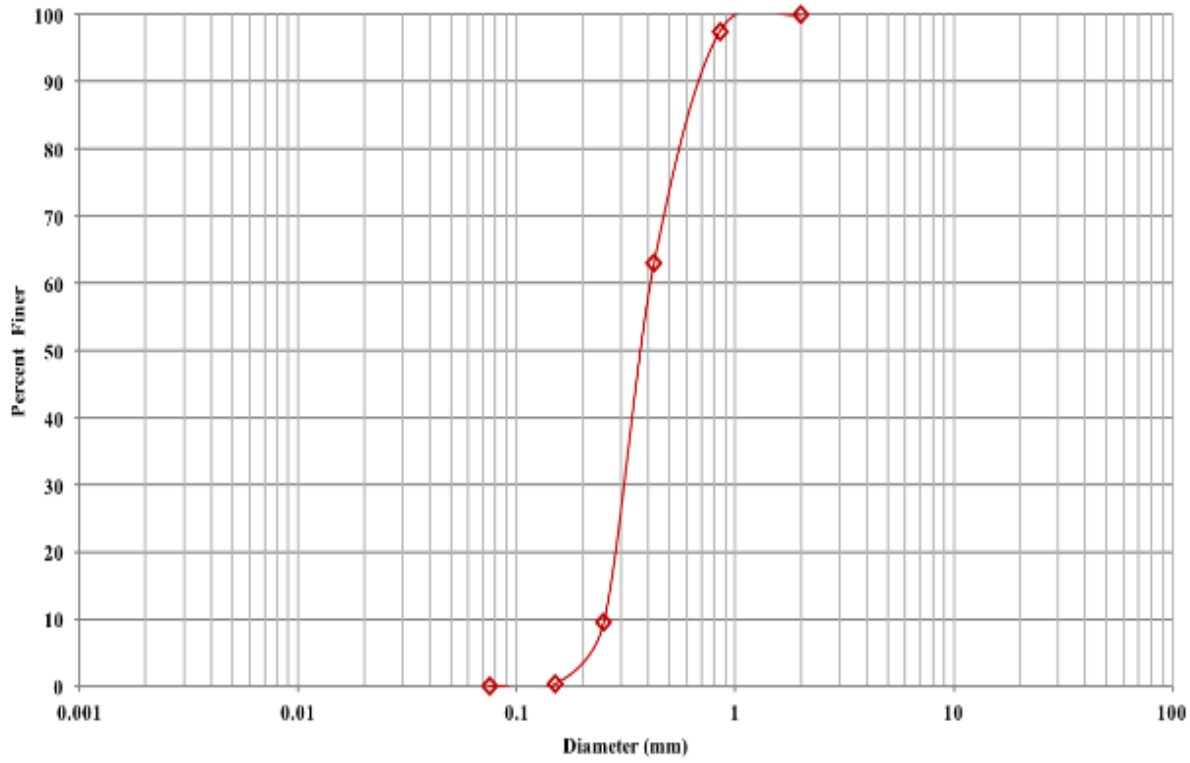

Figure 4.1 Grain size distribution of sand

The D_{10}, D_{30}, and D_{60} of the sand was 0.26, 0.31, and 0.41 respectively. Thus the resulting C_u and C_c where found to be 1.58 and 5.82. According to the Unified Soil Classification System, the material was classified as a coarse grained poorly graded sand (SP).

4.2.1.2 Constant Head Permeameter Test

Constant head permeameter tests are used to determine the hydraulic conductivity characteristic of a material. This laboratory test was completed for the sand (Figures 4.2). A permeameter was completely filled with the selected sand material. The permeameter was slowly saturated from the bottom of the column to the top, ensure no air remain within the voids. The top inlet was then connected to a constant head reservoir. The outlet tube at the bottom of the permeameter was allowed to freely drain. Water was collected from the freely draining outlet tube over a known time to allow for the determination of a flow rate through the sand for a given head.

Figure 4.2 Constant head permeameter filled with sand

Head readings are recorded across the ports along the permeameter column to obtain hydraulic gradients within the sand. The test was completed for numerous different heads within the constant head reservoir and an average was taken of the calculated hydraulic conductivities. The conductivity of the sand was 1.60E-03m/s.

4.2.1.3 Water Retention Curve

The drying water retention curve (WRC) was developed for the sand using a Tempe cell apparatus. The sand was lightly compacted into a consolidation ring using a small steel rod with a flat end to allow for a level surface to be created. The specimen was placed on top of a saturated 1bar (100kPa) porous disk.

A positive pressure was used at the outlet tube below the base of the ceramic disk to allow for the specimen to be saturated from the bottom upwards. The specimen was initial over saturated and the excess water was drained from the specimen to ensure the sample was initial fully saturated. The weight of the apparatus before and after saturation was measured.

An air pressure was not applied to the Tempe cell and was left open to atmosphere. A negative pressure was applied through lowering to the outlet tube in intervals of 0.01 or 0.02m. The suction experienced by the specimen was proportional to the difference in elevation between the specimen and the outlet tube.

Water was allowed to drain from the outlet tube until equilibrium was reached at that specific suction interval. The weight of the apparatus was then measured. The suction interval was increased through lowering the outlet tube. This process of draining water until equilibrium and measuring the weight the apparatus was repeated until the residual water content was reached.

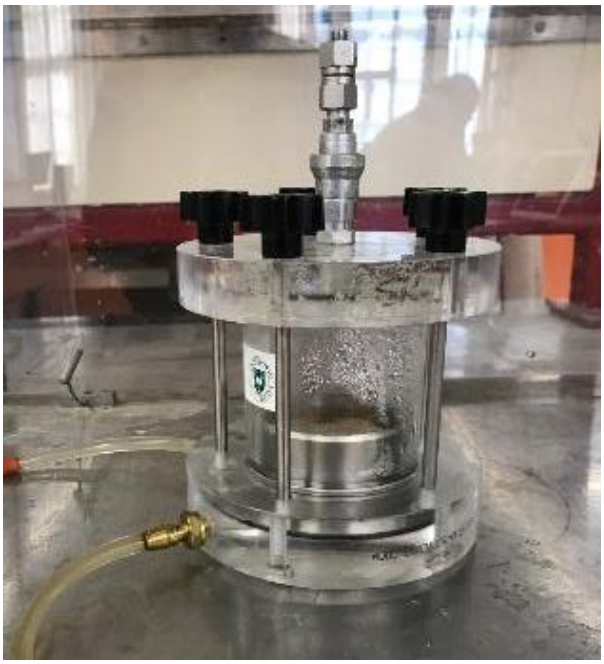

Figure 4.3 Tempe Cell with sand

The measured WRC was then fitted to the Fredlund and Xing (1994) closed form solution. Figure 3.5 is the WRC with the measured experimental WRC of the sand and fitted with the Fredlund and Xing (1994) equation from the SoilVision software. The AEV and saturated volumetric water content were found to be 1kPa and 0.36, respectively.

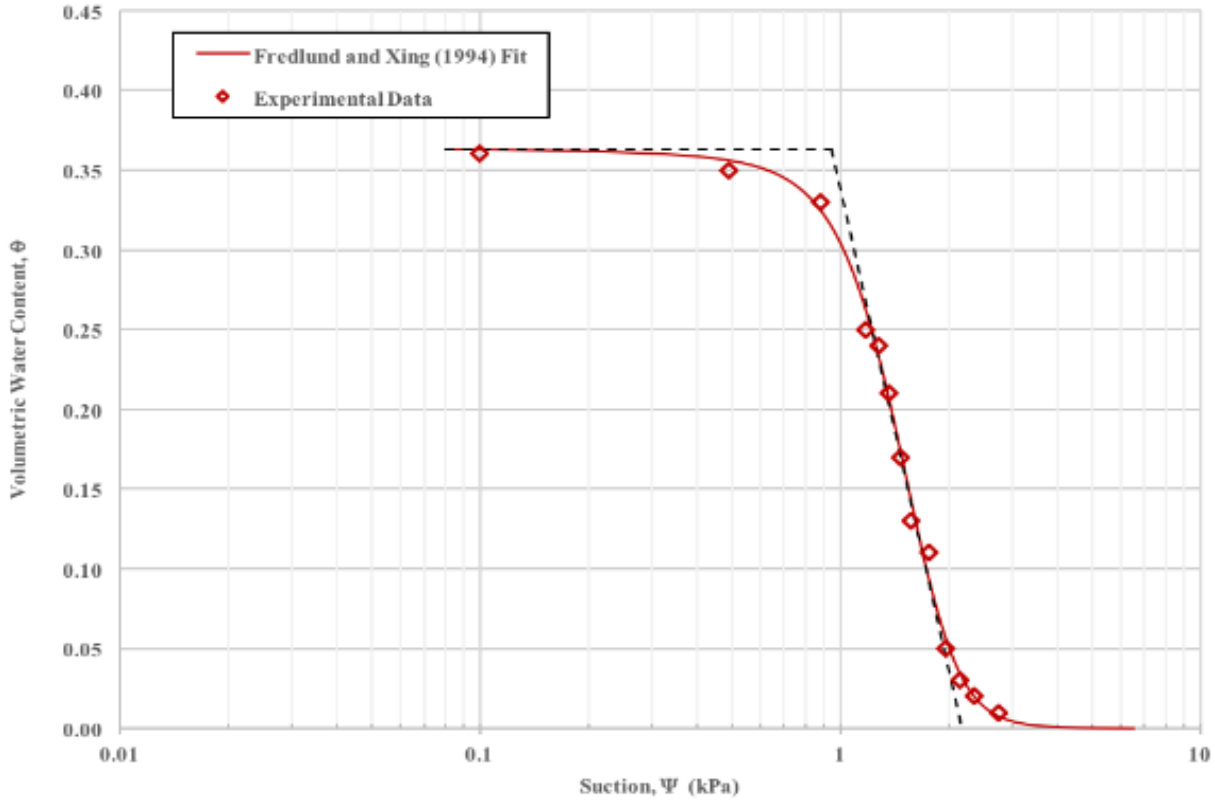

Figure 4.4 Water Retention Curve for sand fitted with Fredlund and Xing (1994) (SoilVision, 2016)

4.2.1.4 Summary of Material Characteristics of the Sand

Table 4.1 compiles all the material properties of the sand used during experimental testing through the completion of Section 3.5 of the laboratory program.

Table B Material properties of sand

Material Characteristic	Value
United Soil Classification System of Material	Coarse grained poorly graded sand (SP)
Specific Gravity, SG	2.65
Hydraulic Conductivity, k	1.60E-03 m/s
Air Entry Value, AEV	1 kPa
Saturated Volumetric Water Content, θ_s	0.36

4.2.2 Nonwoven Needle Punched Geotextile Material Properties

4.2.2.1 Constant Head Permeameter Test

Geotextile disks were cut to the same diameter as the permeameter and stacked to fill the height of the permeameter. This allows for the measurement of the cross-plane hydraulic conductivity to be measured. The same procedure outlined in Section 4.2.1.2 for the sand was followed for the geotextile.

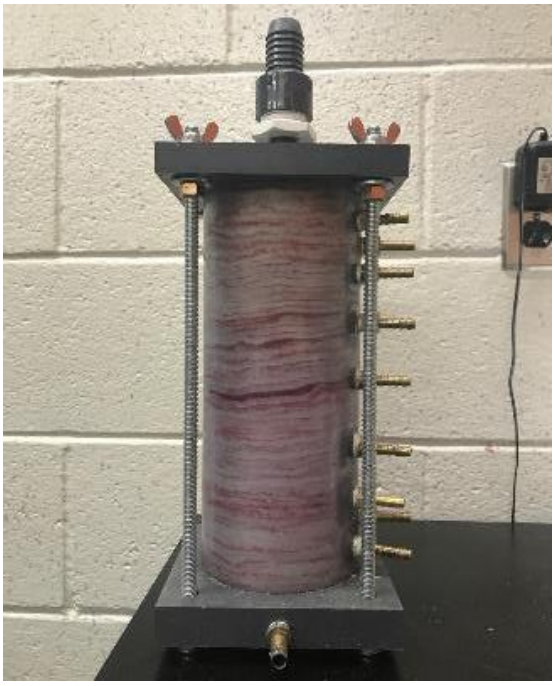

Figure 4.5 Permeameter filled with stacked disks of nonwoven needle punched geotextile

The head within the constant head reservoir was changed multiple times to allow for differing flow rates through the permeameter and an average was taken of the calculated hydraulic conductivities. The hydraulic conductivity of the geotextile was 1.62E-03m/s.

The hydraulic conductivity in the in-plane direction of the geotextile was also measured. This was completed through cutting a cylinder of pottery clay with a low hydraulic conductivity that fit into a permeameter. The clay cylinder was then sliced in half to allow for a piece of geotextile to be placed between the two sides of the cylinder. The sliced edges of the clay cylinder were shaved slightly to compensate for the thickness of the geotextile being inserted between the two halves.

Clay was then smoothed over the edges of the geotextile on the sides of the cylinder to seal the geotextile to ensure no preferential flow paths. Once the clay and geotextile cylinder were assembled it was placed into a permeameter cell. With the hydraulic conductivity of the geotextile being significantly greater than the pottery clay, an in-plane hydraulic conductivity could be measured.

Figure 3.7 shows the setup of the constant head permeameter. The upper compartment was filled with water and the port at the top of the apparatus was connected to a constant head reservoir. The lower compartment was filled with water. An outflow tube was connected to the port on the lower compartment and raised to a known height to allow for a hydraulic gradient and flow rate to be determined. The in-plane hydraulic conductivity of the non-woven geotextile was found to be 6.59E-03m/s.

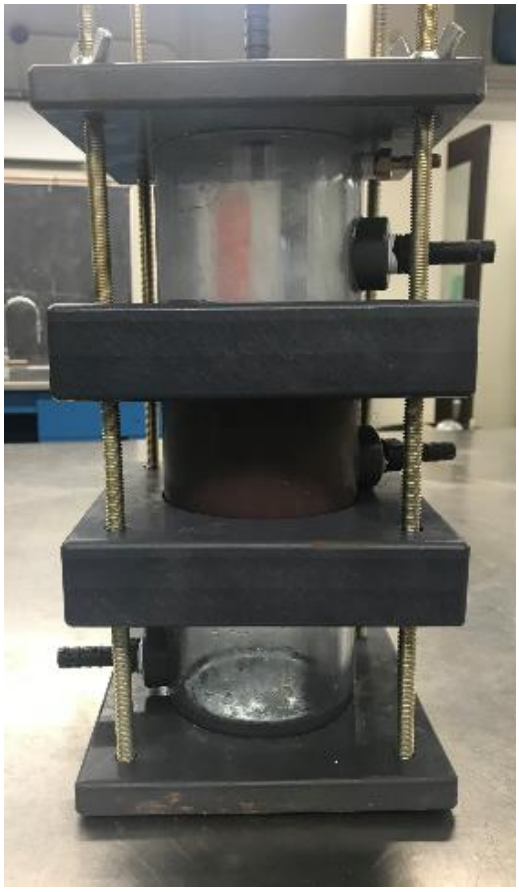

Figure 4.6 Permeameter for the measurement of in-plane hydraulic conductivity of the nonwoven needle punched geotextile

4.2.2.2 Water Retention Curve

The procedure for achieving a water retention curve for the non-woven geotextile was the similar to that used for obtaining a WRC for the sand. A Tempe cell with a larger odometer ring was used for the geotextile testing which was developed at the University of Saskatchewan.

Two nonwoven geotextile disks where stacked in the consolidation ring as the specimen for this testing. Knight and Kotha (2001) determined that the vertical stacking of nonwoven geotextile has minimal influence on the water characteristic curve achieved by a nonwoven geotextile.

The Tempe cell used for the nonwoven needle punched geotextile had a static loading plate where weight could be added to the top of the geotextile. A saturated ceramic disk used for the geotextile testing was 1/2bar (50kPa) porous disk. The outlet tube was again lowered at small intervals.

Figure 4.7 Modified Tempe Cell for geotextile with static loading plate

The drying water characteristic curve (WRC) was developed for the geotextile using a Tempe cell with a static loading plate. Two disks of geotextile were stacked and a weight of 6kPa (3kg) was added to the loading plate on the Tempe cell apparatus. The static load of 6kPa was applied to simulate the weight of the sand (thickness approximately 0.4m) which would be placed on top of the geotextile in the large-scale apparatus during experimental testing. Figure 3.9 is the WCC with the measured experimental WRC of the geotextile and fitted with the Fredlund and Xing (1994) equation from the SoilVision software. The AEV and saturated volumetric water content of the nonwoven geotextile were found to be 0.77kPa and 0.83, respectively.

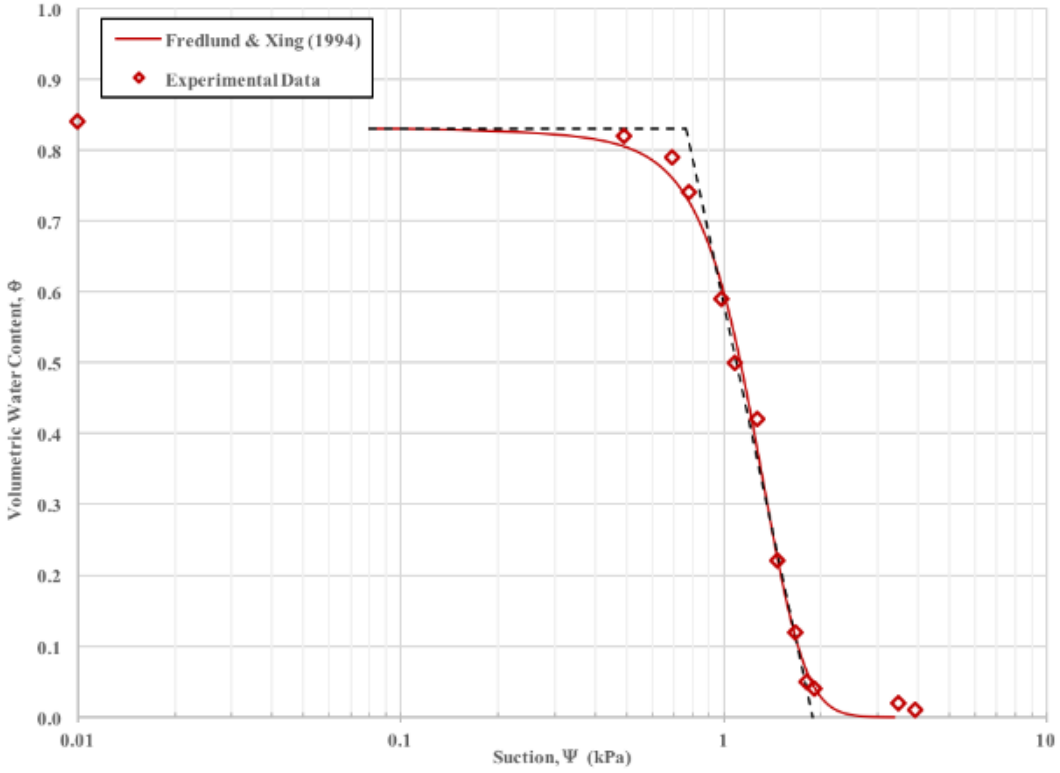

Figure 4.8 Water retention curve for nonwoven needle punched geotextile fitted with Fredlund and Xing (1994) (SoilVision, 2016)

4.2.2.3 Gradient Ratio Test

Gradient ratio test is used to measure the hydraulic gradients of a water saturated soil-geotextile system (American Standards of Testing and Materials, 2011). This test was completed to determine the compatibility of the sand and non-woven needle punched geotextile used in the experimental testing.

The permeameter cell was used to complete this testing as shown in Figure 3.10. A geotextile disk was placed on a metal mesh support above the lower water reservoir. Sand was then placed on top of the geotextile disk in the upper compartment. The permeameter was then saturated from the bottom reservoir upwards to ensure no air was trapped below the geotextile. Once the geotextile and sand were fully saturated with water the flow was reversed; a constant head reservoir is connected to the top port and the outlet port was allowed to drain.

Figure 4.9 Modified permeameter cell used for hydraulic conductivity ratio test

The ports along the length of the permeameter cell were used to measure head readings across the geotextile and within the sand. Thus allowing for the ratio of the two hydraulic gradients to be determined. After allowing the test to run for a length of 3 hours, the hydraulic gradient ratio of the sand geotextile system was equal to 1.02. This indicates that neither piping or clogging was occurring. The sand and nonwoven needle punched geotextile where found to be compatible from this testing.

4.2.2.4 Nominal Thickness of Geotextile

The nominal thickness of a geosynthetic are determined following ASTM D5199 as the thickness of geosynthetics may vary with applied loads. Nominal thickness is completed through determining the thickness of a geotextile under the weight of 2.0kPa (0.29psi) as specified by ASTM D5199. The thickness of the geotextile is to be measured after 5 seconds of the weight being applied.

Circular disks of the non-woven geotextile were cut from different sections of the geotextile roll. Based on the area of the circular disks a weight equalling 2.0kPa ± 0.002kPa was applied to the geotextile. A dial gauge was used to determine the change in thickness of the geotextile after the specified 2.0kPa was applied. Ten circular disks of the non-woven needle punched geotextile were measured for nominal thickness. These values were averaged to obtain a nominal thickness for the geotextile of 4.62mm.

4.2.2.5 Apparent Opening Size of the Non-Woven Needle Punched Geotextile

The apparent opening size (AOS) allows for the determination of the largest opening size of the geotextile. This was done by sieving various soils to a nominal particle size, then using the gradient ratio apparatus to determine if the soil causes clogging or piping of the geotextile. Clogging and piping can be determined through measuring the before and after masses of the soil.

Various soils were sieved to a uniform nominal grain size and tested with the non-woven needle punched geotextile. Soils were sieves to nominal particle diameters of 0.074mm (sieve No. 200), 0.063mm (sieve No. 230), 0.053mm (sieve No. 270), and 0.044mm (sieve No. 325).

Knowing the soils grain size distributions and the passing and retaining sieves the largest particle size passing through the geotextile can be determined. Particles of 0.074mm nominal size were 100% retained on the geotextile. These particles were passing the No. 100 sieve and retained on the No. 200 sieve. Particles of 0.063mm nominal size resulted in 35% passing through the geotextile. These particles were sieved to pass No. 200 sieve and retained on the No. 230 sieve. Thus, the AOS of the non-woven needle punched geotextile was found to be between 0.074 and 0.063mm.

4.2.2.6 Summary of Material Characteristics of the Geotextile

Table 4.2 compiles all the material properties of the nonwoven needle punched geotextile used during experimental testing through the completion of Section 3.5 of the laboratory program.

Table C Material properties of nonwoven needle punched geotextile

Material Characteristic	Value
Fiber Material	Polypropylene
Specific Gravity, SG	0.90
Mass per unit area, MUA	580 g/m^2
Apparent Opening Size, AOS	63-74μm (Sieve No. 230-200)
Void Ratio, e	0.87
Nominal Thickness	4.62 mm
Cross-Plane Hydraulic Conductivity, k	1.62E-03 m/s
In-Plane Hydraulic Conductivity, k	6.59E-03 m/s
Air Entry Value, AEV	0.77 kPa
Saturated Volumetric Water Content, θ_s	0.83

4.2.3 Results for Sizing of Geotextile

Three geotextile sizes were tested within the constant head apparatus. Tests were complete to determine if the size of the geotextile overlying the geomembrane influenced the flow through the geomembrane defect. The geotextiles were secured in place through taping the edges. The results of these trials resulted in similar flow rates for corresponding hydraulic heads above a defect of diameter 0.0025m.

The linear regression analysis performed on these three geotextile sizes with regards to flow rate achieved an R-squared value of 0.987, thus determining the sizing of the geotextile is insignificant.

4.3 Circular Defects on Flat Geomembrane Surfaces

4.3.1 Summary of Experimental Results

Four circular defect sizes were tested using the large-scale constant head apparatus as described in Section 4.2. These defects are classified as small circular defects according to Giroud and Bonaparte (1989a) as the defect areas are less than 1.0E-04m^2. The selected defect sizes for

experimental testing were diameters, d, of approximately 0.0015m (1.77E-06m^2), 0.0025m (4.91E-06m^2), 0.0050m (1.96E-05m^2), and 0.0075m (4.42E-05m^2).

The large-scale constant head apparatus allowed for the hydraulic head and flow rate for each of the geomembrane defects to be measured. Hydraulic heads applied above the geomembrane defect ranged 0.10 to 0.30m. Three selected hydraulic gradients were applied across the geomembrane system.

A back pressure of 0.0m was applied to the bottom boundary condition of the defect for all experimental testing. To examine the influence of this boundary condition three back pressures, 0.0, 0.02, and 0.05m, were applied to a defect of diameter 0.0025m. Completing a statistical analysis on the effects of the various back pressures found that the effect of back pressure on the flow rate was insignificant (F=0.33).

Control tests were completed prior to the start of each defect testing. The control tests were completed to determine the hydraulic conductivity of the sand within the large-scale apparatus (Section 3.5). From these initial tests the hydraulic conductivity of the sand varied only slightly, between 0.0013m/s and 0.0018m/s. The laboratory permeameter test measured the hydraulic conductivity of the sand to be 0.0016m/s (Section 3.3). FEMs were simulated for the various defect sizes with the sand having a hydraulic conductivity of 0.0013m/s, 0.0016m/s, and 0.0018m/s.

The experimental results found that as the defect size increased the flow rate through the defect increased. The flow rate through the defect also increased with increasing hydraulic head above the defect. Experimentally achieved flow rates for the four circular defects are shown in Figure 4.10 and 4.11.

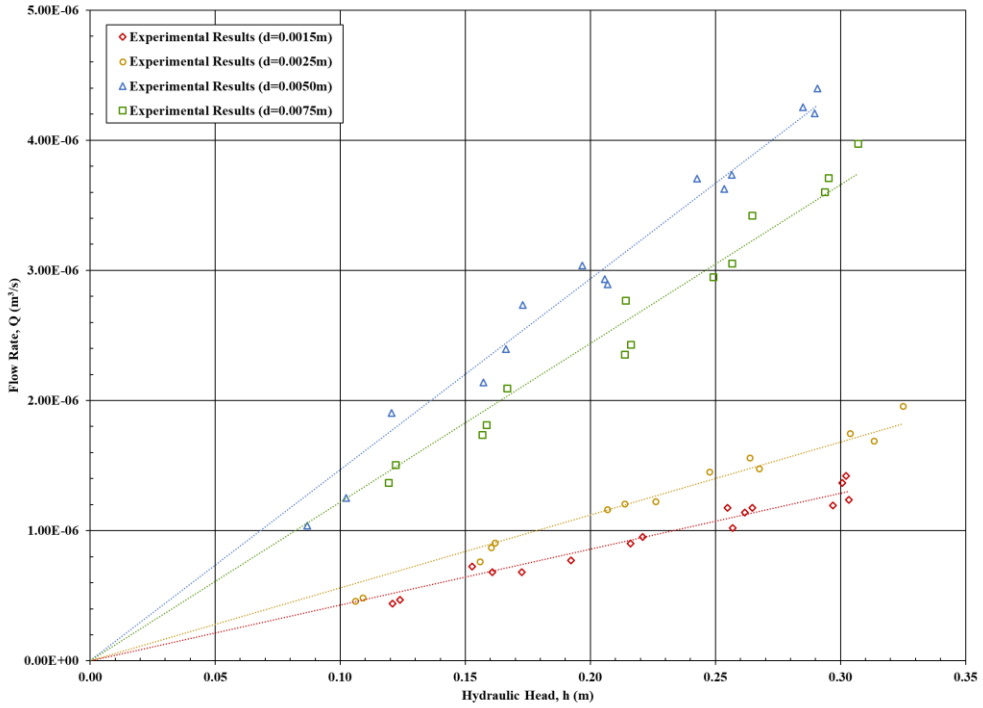

Figure 4.10 Experimental flow rates through four circular geomembrane defects

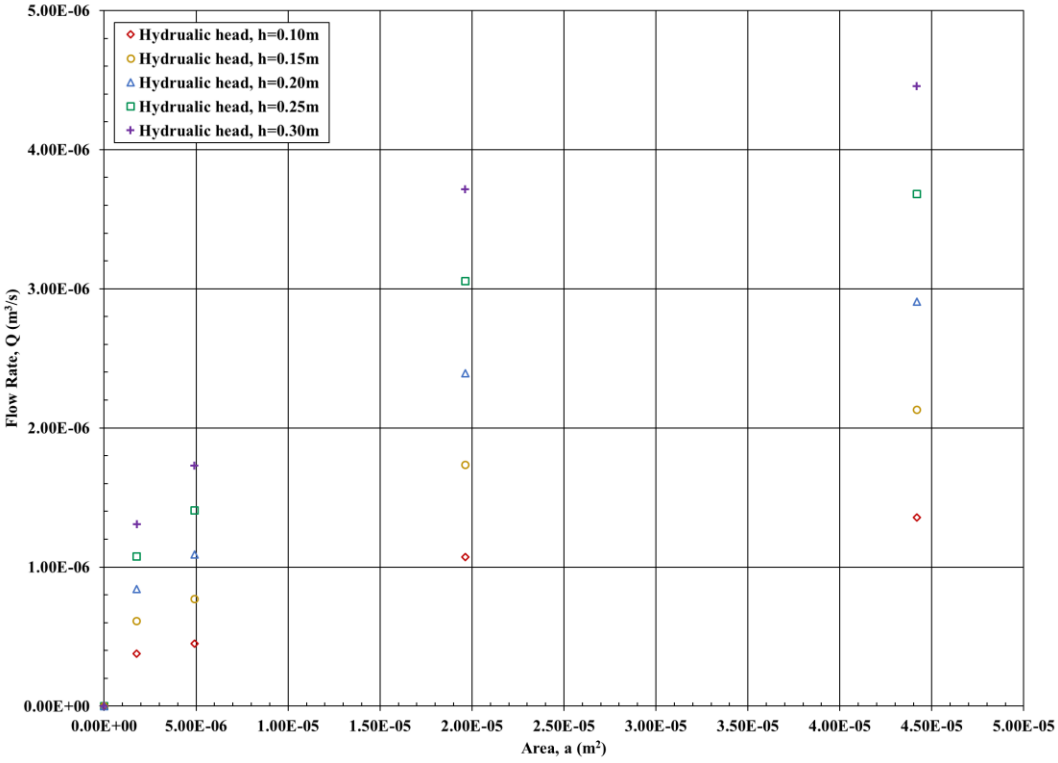

Figure 4.11 Experimental flow rates for the circular defects at hydraulic heads above the defect

A prediction interval of 95% was applied to the data to evaluate the measured experimental data. All the measured data fell within the set prediction interval. The prediction intervals are narrower for the smaller diameter defects (0.0015m and 0.0025m) in comparison to the larger diameter defects (0.0050m and 0.0075m). This is likely due to the smaller defects being easier to maintain an equilibrium in head in comparison to the larger defects. Thus the data for the smaller defects had less scatter in the measurements. The experimental data resulted in R^2 values greater than 0.95 for all circular defects.

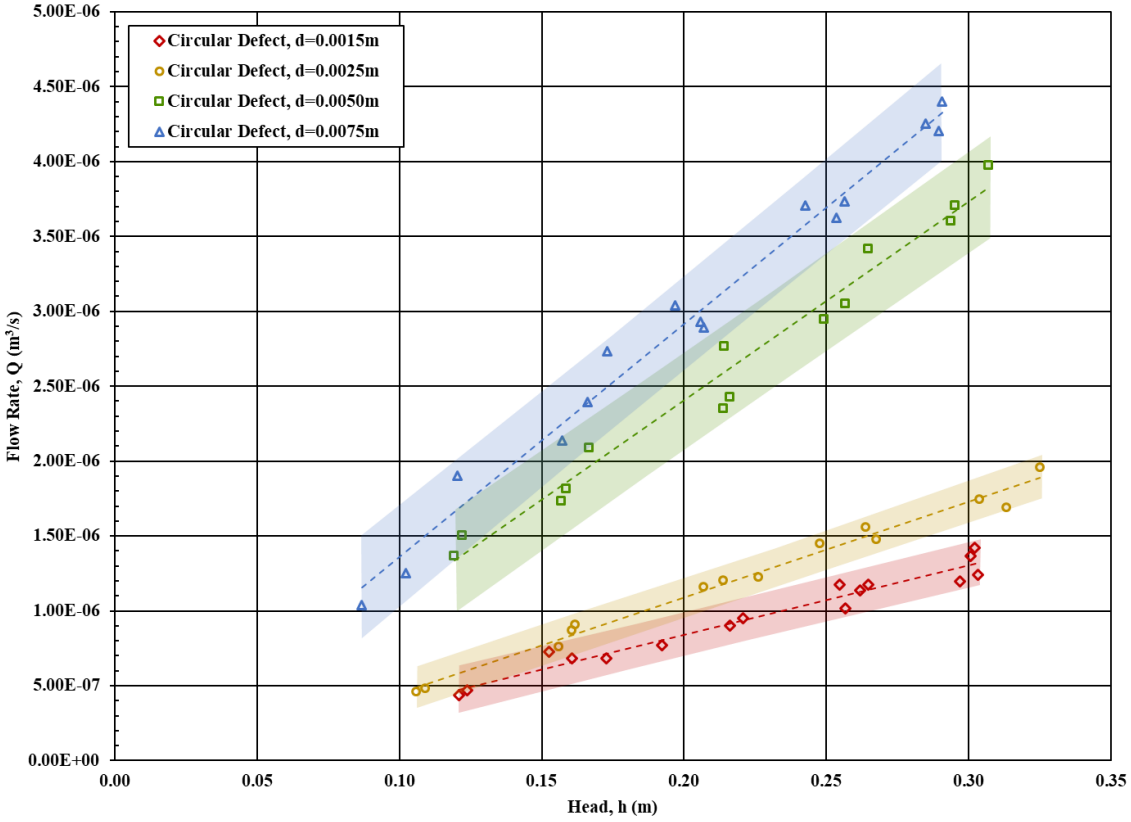

Figure 4.12 Experimental flow rates for four circular defects with 95% prediction intervals

4.3.2 Comparison of the Experimental Results and Empirical Solution

Empirical solutions have been developed for various geomembrane systems. The geomembrane system refers to the characteristics of the overlying and underlying material surrounding the geomembrane. Equation 2.3 proposed by Bonaparte et al. (1989) is the applicable solution for the experimental system within the large-scale constant head apparatus.

This equation is an empirical solution for a system with a lesser permeable material above the geomembrane than that below the geomembrane. The large-scale constant head apparatus was a representation of this system. The overlying sand limited the flow of water through the defect whereas the boundary condition on the underside of the defect was an applied head with no further dissipation of head. Bonaparte et al.'s (1989) proposed equation is for circular defects on flat geomembrane surfaces.

Experimental results were compared to the empirical solution to evaluate how effective the empirical solution was at predicting the flow rate through a defect. Bonaparte et al.'s (1989) proposed equation was evaluated for the four circular defect sizes. The empirical equation resulted in the same trend as the experimental results; Flow rates through a defect increased with increasing head and increasing defect area. Figure 4.13 compare the empirical estimations to the measured experimental results.

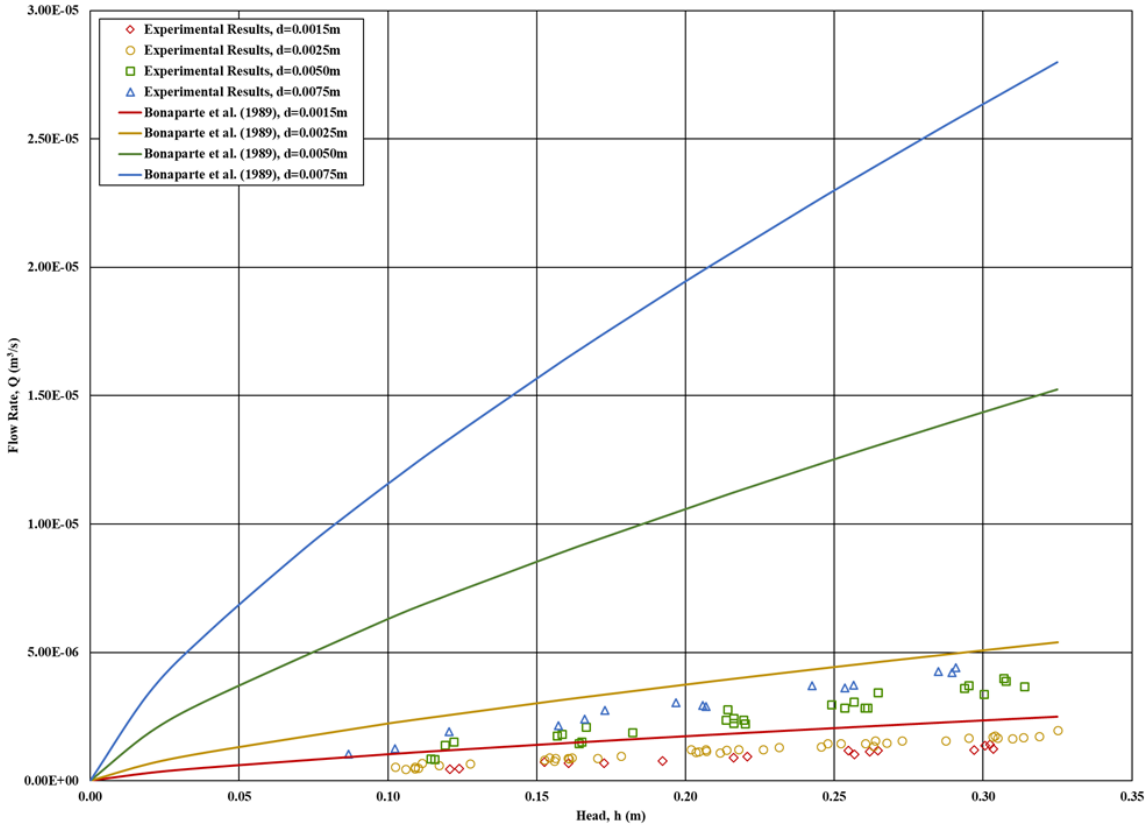

Figure 4.13 Comparison of experimental results and Bonaparte et al. (1989) estimations for circular defects

The empirical solution overestimated the flow rate in comparison to the experimental results. The following table shows the percent error for the experimental defects in comparison to the empirical solution. The correction factor was calculated using Equation 3.7 discussed in Section 3.8. As defect size increases the correction factor between the experimental and empirical results decrease. In addition, for each defect size as the hydraulic head increases the correction factor increases.

Table D Correction factor of experimental results and empirical solution for four circular defects

Defect diameter, d (m)	Defect Area, a (m^2)	Head above Defect, h (m)	Correction Factor
0.0015	1.77E-06	0.10	37%
		0.20	48%
		0.30	55%
0.0025	4.91E-06	0.10	23%
		0.20	29%
		0.30	33%
0.0050	1.96E-05	0.10	13%
		0.20	21%
		0.30	25%
0.0075	4.42E-05	0.10	12%
		0.20	15%
		0.30	17%

3.9.1 4.2.3 Reynolds Number for Flow through a Geomembrane Defect

Determining a Reynolds number for the flow through a geomembrane defect allows for the evaluation of the flow regime occurring within the defect void. Reynolds number for flow through a pipe can be used to calculate the Reynolds number for the flow occurring within the geomembrane defect. De Nevers (1991) stated that Reynolds numbers typically less than 2000 indicate laminar flow, 2000 to 4000 indicate transitional flow, and greater than 4000 indicates turbulent flow.

The use of Equation 2.10 requires the assumption that the average velocity equal to the flow rate through the defect divided by the area of the defect. Table 4.4 summarizes maximum and minimum Reynolds numbers calculated for the defects in 60mil geomembrane. Reynolds numbers were found to decrease within increasing defect size. All Reynolds numbers calculated for the circular and rectangular defects were less than 2000 indicating a laminar flow regime.

Table E Reynolds number for circular and rectangular defects for 60mil geomembrane thickness

Defect Area, a (m^2)	Reynold Number, Re	
Circular Defects		
1.77E-06	Min	419
	Max	1354
4.91E-06	Min	157
	Max	671
1.96E-05	Min	117
	Max	341
4.42E-05	Min	40
	Max	168
Rectangular Defects		
3.3E-05	Min	326
	Max	926
5.4E-05	Min	264
	Max	774

Table 4.5 summarizes the maximum and minimum Reynolds numbers for the circular defects of 0.005m diameter in geomembrane of thicknesses 80 and 120mil. Reynolds numbers indicated laminar flow. Reynolds numbers were found to decrease with increasing geomembrane thickness due to the flow rate through the defect decreased within increasing geomembrane thickness.

Table F Reynolds number for circular defect of diameter 0.005m for different geomembrane thickness

Geomembrane Thickness	Reynold Number, Re	
Circular Defects		
80 mil	Min	64
	Max	261
120 mil	Min	40
	Max	237

4.3.3 Comparison of Experimental Results and Finite Element Model Estimations

4.3.3.1 General

The finite element models were developed based on the experimental apparatus and testing procedures. The constant head permeameter test determined the hydraulic conductivity of the sand to be 0.0016m/s. Through completing control tests prior to each experiment using the large-scale constant head apparatus, the hydraulic conductivity of the sand was measured and found to vary between 0.0013m/s and 0.0018m/s.

During the experimental testing a geotextile was placed over the geomembrane to separate the overlying sand from the defect. The gradient ratio test found that the sand and geotextile were compatible with no piping or clogging occurring. The geotextile had a similar cross-plane hydraulic conductivity to the overlying sand. However, as presented in Chapter 3, the in-plane hydraulic conductivity was greater than the cross-plane direction. The sand and geotextile had similar air entry values of 0.95 and 0.77, respectively. The difference in hydraulic properties of the sand and geotextile were determined to be minimal. The geotextile remained fully saturated throughout experimental testing and thus the influence of the material on the flow rate was assumed to be minimal.

As discussed in Chapter 3, the sizing of the geotextile placed above the geomembrane was tested and found to have a negligible influence on the resulting flow through the geomembrane. It should be noted that for the finite element (FE) analysis the geotextile was not explicitly represented in any of the numerical models that were developed.

The hydraulic effects of the geotextile were not explicitly incorporated within the 2D axisymmetric models. A circular defect of 0.005m was analysed using a 3D FEM at three hydraulic heads with and without the geotextile present, which is further discussed in Section 4.3.3.2. The presence of the geotextile was examined in the 3D FEMs for circular defect on a sloped geomembrane surface. Due to the different in-plane and cross-plane hydraulic conductivities it was assumed that the geotextile may have a greater influence when on a sloped geomembrane surface.

The percent error calculation was used to compare experimental and finite element results. It should be noted that a positive percent error value indicates that the experimental flow rate is larger than the finite element flow rate and a negative percent error indicated the opposite.

4.3.3.2 2-Dimensional Finite Element Model Estimations: GeoStudio and SoilVision

The axisymmetric models were developed in two finite element modelling software to analyze the flow through a defect in 2-dimensions. The 2D models were used to analysis applicable testing configurations for circular defects where neither a slope or hydraulic gradient was present. The FEM setup as described in Section 3.7 was the same for the models developed in both software. The 2D axisymmetric models used the origin as the location of symmetry. This setup allowed for circular defects to be analyzed. SoilVision (2017) and GeoStudio (2018) resulted in similar estimated flow rates. A percent difference calculation was completed using Equation 3.8 discussed in Section 3.8.

The percent difference between the two FEM software estimations were calculated for various defect areas at hydraulic heads of 0.10, 0.20, and 0.30m. Percent difference between the two FEMs ranged between 1 to 3%. It is assumed that the resulting difference between the two software's is due to the use of different units for each program resulting in slightly different input values and model dimensions. Hydraulic gradients could not be applied within the 2D axisymmetric FEMs. The percent difference decreases with increasing defect area. In addition, the percent difference for each defect area are approximately the same for the three applied hydraulic heads.

Table G Percent difference of flow rate for two 2D finite element models for circular defects

Defect Area, a (m^2)	Head above Defect, h (m)	Percent Difference (%)
1.13E-06	0.10	3
	0.20	3
	0.30	3
4.91E-06	0.10	3
	0.20	3
	0.30	3
1.96E-05	0.10	1
	0.20	1
	0.30	1
4.42E-05	0.10	3
	0.20	3
	0.30	3

The 2D FE estimations overestimate the flow rate through all four of the experimentally tested defect sizes. The experimental and 2D FEM flow rates are most comparable for the smaller defect sizes. As the defect size increases the difference between the experimental and FEM results increases. Figure 4.14 shows the comparison of experimental data to the 2D axisymmetric FEM estimations.

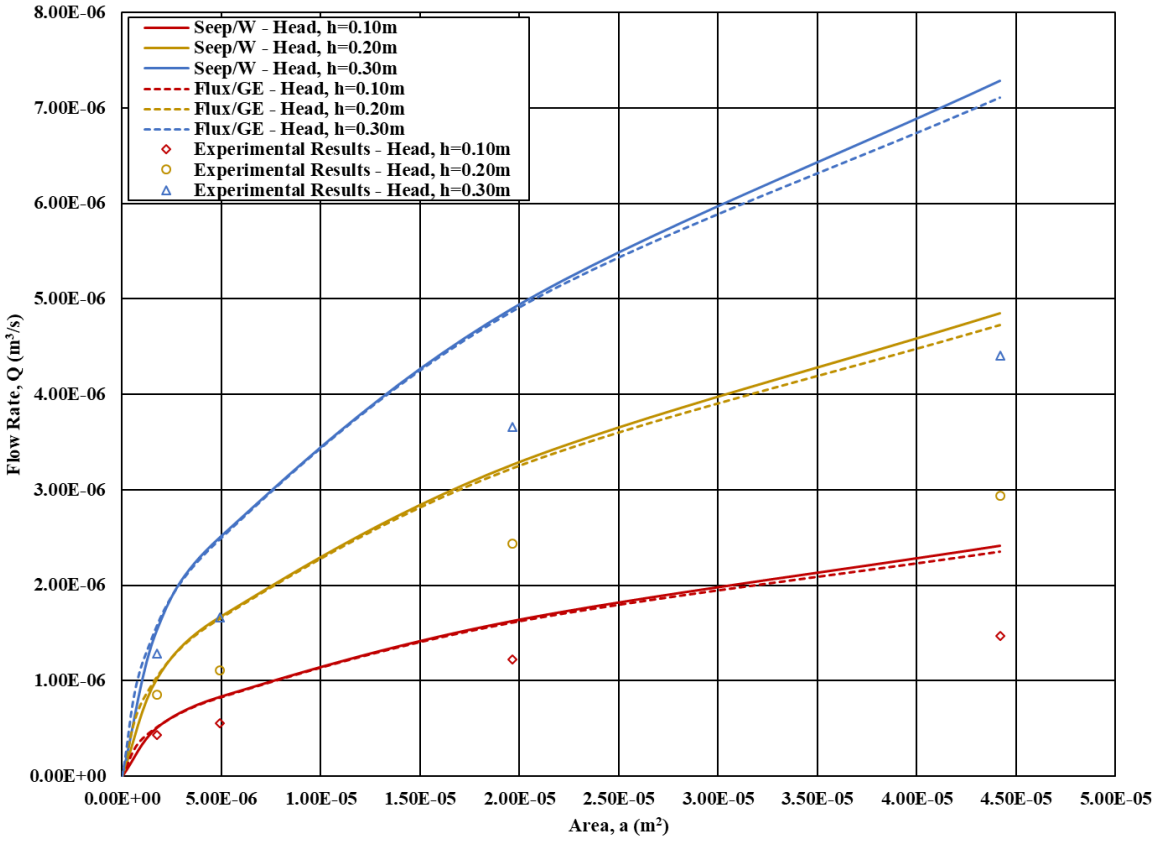

Figure 4.14 Comparison of 2D axisymmetric finite element model and experimental results for circular geomembrane defects

The percent error between the experimental results and the different 2D axisymmetric FEMs are shown in Table 4.7. Percent errors for the four different defect sizes are similar between the two different FEMs.

Table H Percent error of the experimental and 2D axisymmetric finite element modelling results for four circular defects

Defect Area, a (m^2)	Head above Defect, h (m)	Percent Error SEEP/W (%)	Percent Error SVFLUX/GE (%)
1.77E-06	0.10	-17	-14
	0.20	-17	-14
	0.30	-17	-14
4.91E-06	0.10	-34	-32
	0.20	-34	-32
	0.30	-34	-32
1.96E-05	0.10	-25	-24
	0.20	-25	-24
	0.30	-25	-25
4.42E-05	0.10	-39	-38
	0.20	-39	-38
	0.30	-40	-38

The 3D FEM's were developed after determining that the 2D axisymmetric FEM's resulted in an overestimation of flow rate in comparison to the experimental results. The 2D FEMs were not the best evaluation for the flow rate as the flow through a geomembrane defect is a 3-dimensional problem.

4.3.3.3 3-Dimensional Finite Element Model Estimations: SoilVision

SoilVision software had the capability of developing 3D FEM models using SVFLUX/GE. Due to limitations of the FEM software the exact defect sizes used in the experimental testing could not be modeled. Thus defect sizes ranging from a diameter of 0.0006m to 0.0080m were modelled and flow rates for the experimental defect sizes were interpolated. These models were developed without a region of a geotextile located between the defect and the sand.

The 3D FEM's allowed for the experimental setup to be modelled. The effect of horizontal hydraulic gradients across the geomembrane system were determined through the use of 3D modelling. When a hydraulic gradient was applied within the 3D FEMs it was found to have minimal influence on the estimated flow rate through the defect. The resulting head over the defect was the average hydraulic head applied across the system.

Approximately the same three hydraulic gradients were used during experimental testing for the four defects. A multiple variable regression was completed using the statistics program SPSS to analyze the significance of the effects of various factors on the experimental defect flow rate. The hydraulic gradient applied within the overlying material was found to be insignificant (F=0.802) using a confidence interval of 95% when analyzing the defect flow rates.

The effect of the hydraulic head above the defect was significant. The results of the 3D models followed the same trend as the 2D models. As the head above the defect increased, the flow through the defect increased.

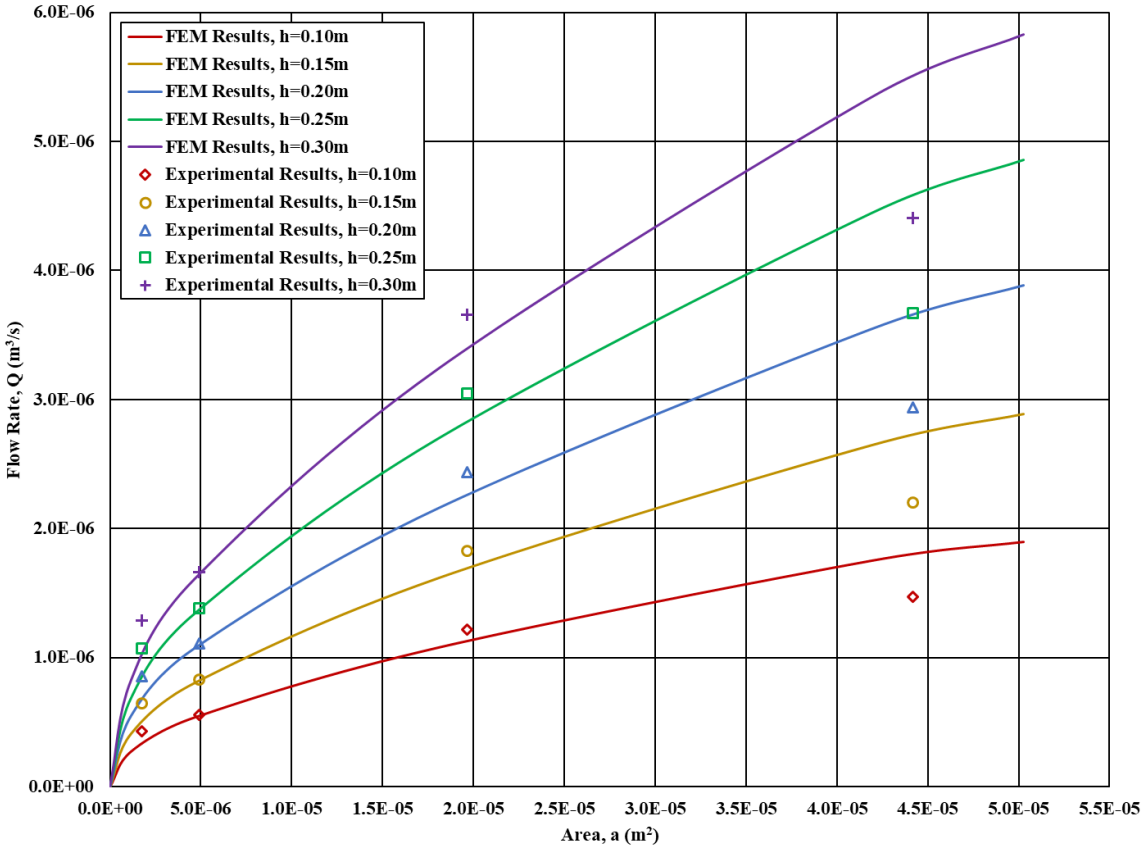

Figure 4.15 Experimental and 3D FEM results with overlying sand having a hydraulic conductivity of 0.0016m/s

Linearly interpolated flow rates were calculated for the FE analysis using a hydraulic conductivity of 0.0016m/s for the corresponding areas of the experimental defect sizes. Defects of diameter 0.0015 and 0.0075m resulted in the highest percent errors. The high percent error for these defects

is due to limitations of FEM mesh spacing and refinement when FE analyses were carried out at the same scale as the experimental apparatus.

Table I Percent error of experimental data and interpolated 3D FEM results for four circular defects

Defect diameter, d (m)	Defect Area, a (m^2)	Hydraulic Head above Defect, h (m)	Percent Error (%)
0.0015	1.77E-06	0.10	34
		0.20	34
		0.30	33
0.0025	4.91E-06	0.10	1
		0.20	1
		0.30	1
0.0050	1.96E-05	0.10	9
		0.20	8
		0.30	8
0.0075	4.42E-05	0.10	-18
		0.20	-19
		0.30	-20

The experimental results were compared to FEMs with the different hydraulic conductivities measured for the overlying sand. The conductivities are shown as the shaded area on the graph for three different hydraulic heads (0.10, 0.20, and 0.30m), where the conductivity of lower bound is 0.0013m/s and the upper bound is 0.0018m/s. Flow rates of the corresponding experimental defect areas were interpolated for the FE results. The percent errors were determined between the experimental and FEMs for the three different hydraulic conductivities (Table 4.9).

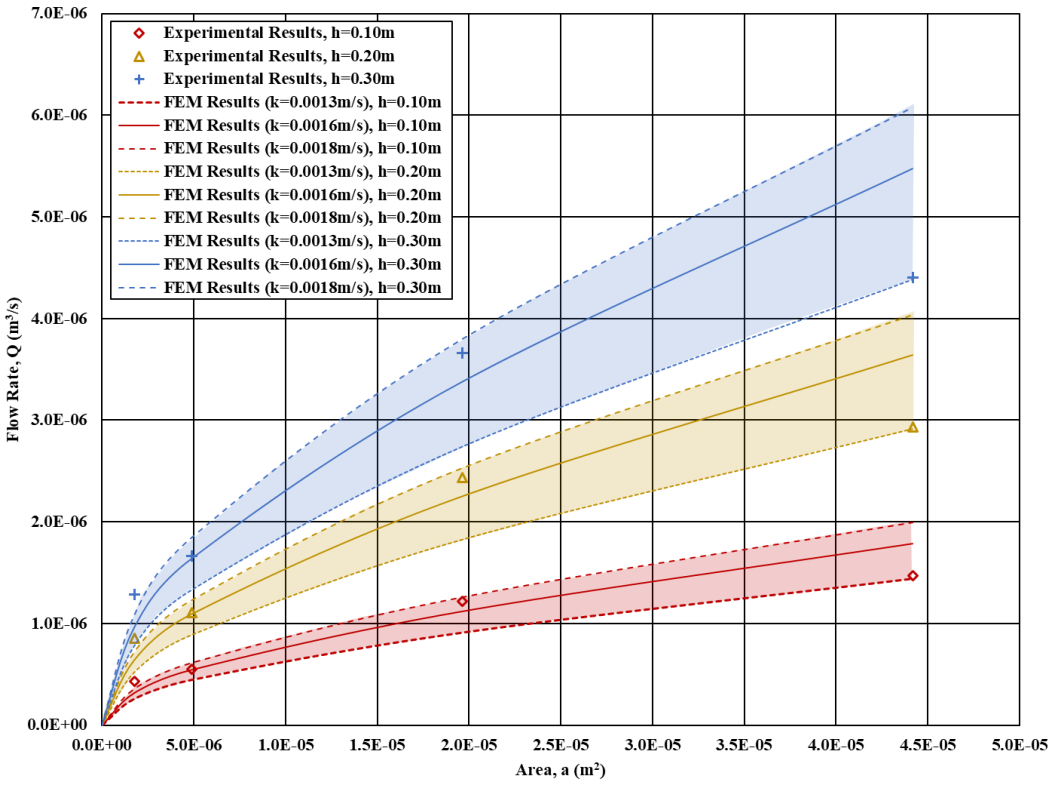

Figure 4.16 Experimental and 3D FEM flow rates for circular defects with overlying sand having three different hydraulic conductivities

Table J Percent error of experimental data and interpolated 3D FEM results for four circular defects with overlying sand having three different hydraulic conductivities

Defect Diameter, d (m)	Defect Area, a (m^2)	Head, h (m)	Percent Error for FEM with k=0.0013m/s (%)	Percent Error for FEM with k=0.0016m/s (%)	Percent Error for FEM with k=0.0018m/s (%)
0.0015	1.77E-06	0.10	65	34	19
		0.20	64	34	19
		0.30	64	33	19
0.0025	4.91E-06	0.10	24	1	-10
		0.20	24	1	-10
		0.30	24	1	-10
0.0050	1.96E-05	0.10	34	9	-3
		0.20	34	8	-4
		0.30	33	8	-4
0.0075	4.42E-05	0.10	2	-18	-26
		0.20	1	-19	-27
		0.30	0	-20	-27

These initial 3D FEM's were scaled to the experimental system dimensions. As discussed in Section 3.8, FEM dimensions were then scaled-up 10 times the size of the experimental system. This allowed for better mesh refinement capabilities due to the small size of the geomembrane defects. The scaled-up models were developed with a hydraulic conductivity of 0.0016m/s for the overlying sand.

The flow rate estimated from the scaled-up FEMs were divided by 100 to scale-down the flow rate. The scaled-up FEMs for the three defects of diameters 0.0025m, 0.0050m, and 0.0075m resulted in a slight decrease in flow rates of those found from the original FEMs. For the smallest defect the scaled-up FEM resulted in the most profound change in flow rate. The scaled-up model allowed for a better estimation of the flow rate due to increased meshing capabilities in the scaled-up model.

Table K Percent error of experimental data and interpolated results for scaled-up 3D finite element models for four circular defects

Defect Diameter, d (m)	Defect Area, a (m^2)	Hydraulic Head above Defect, h (m)	Percent Error for FEM with k=0.0016m/s (%)
0.0015	1.77E-06	0.10	15
		0.20	16
		0.30	17
0.0025	4.91E-06	0.10	2
		0.20	1
		0.30	1
0.0050	1.96E-05	0.10	7
		0.20	6
		0.30	6
0.0075	4.42E-05	0.10	-3
		0.20	-10
		0.30	-12

Hydraulic head readings were taken experimentally using twelve manometers spaced around the geomembrane defect as shown in Section 3.5.2. The manometers allowed for the determination of the hydraulic head profiles surrounding the defect to be measured. Hydraulic head profiles from the FEMs were analyzed in both cross-sectional directions of the apparatus. Examining the

experiment and FEM hydraulic head profiles allows for the confirmation of the comparisons that can be made between the two methods.

Head measurements were completed the same for every experimental trial. Comparing the experimental and FEM head profiles was completed for a 0.0050m diameter defect. The comparison hydraulic head profiles for the 0.0050m diameter defect resulted in percent errors typically within the range of 0 and 4%. The average percent error for all hydraulic head profile readings was 2%.

FEMs allowed for the analysis of the localised hydraulic gradients occurring immediately around the geomembrane defect. The FE analyse Darcian flow through the soil, toward the sink represented by the defined pore pressure boundary condition at the defect. Thus the potential effects of non-Darcian flow and the effects of high localised hydraulic gradient and turbulent flow effects occurring around and within the defect are not taken into consideration.

The FEM hydraulic gradients immediately surrounding the defect were found to increase with increasing hydraulic head above the defect and increase with decreasing defect size. Greater hydraulic heads cause an increase in pressure around the defect, in turn increasing flow through the defect. As the size of the defect decreases the same pressures occur immediately around the defect with less area for the fluid to move through the defect.

Walton and Sagar (1990) state that as the smaller defects experience higher resistances through the stem of the defect than larger defects, as the flow through the larger defects are more independent of defect size. The localised hydraulic gradients near the defect are shown in Table 4.11 for defect sizes similar to those used during the experimental testing.

Table L Results for the 3D scaled-up FEM maximum hydraulic gradients near the circular defects

Defect Diameter (m)	Defect Area, a (m^2)	Hydraulic Head above Defect, h (m)	Maximum Hydraulic Gradient Immediately Surrounding the Defect (m/m)
0.0015	1.77E-06	0.10	80
		0.20	159
		0.30	238
0.0025	4.91E-06	0.10	53
		0.20	106
		0.30	159
0.0049	1.96E-05	0.10	24
		0.20	49
		0.30	73
0.0073	4.42E-05	0.10	16
		0.20	33
		0.30	49

The previous models discussed in this section did not include a region for the geotextile. FEMs were developed for a circular defect of diameter 0.005m with a geotextile present for three hydraulic heads (0.10, 0.20 and 0.30m). These models found that the flow rate and localised hydraulic gradients were larger than the models without the geotextile included. FEMs with varying geomembrane thickness and elongated defects were not analysed for the effect of a geotextile region. However, it could be assumed that the inclusion of a geotextile within all the FEMs on a flat geomembrane surface would have the same result for circular defects and potentially elongated defects. Including the geotextile would thus result in a further overestimation of the estimated flow rates through circular defects in comparison to the experimental results.

4.3.3.4 Effect of Geomembrane Thickness of Flow Rate through a Circular Defect

Geomembrane thickness was as analysed for how it influences flow rate through a defect. Experimental testing was completed using a 0.0050m circular defect for three different geomembrane thicknesses (60, 80, and 120mil). The experimental results found that as the thickness of the geomembrane increased the flow through the defect decreased.

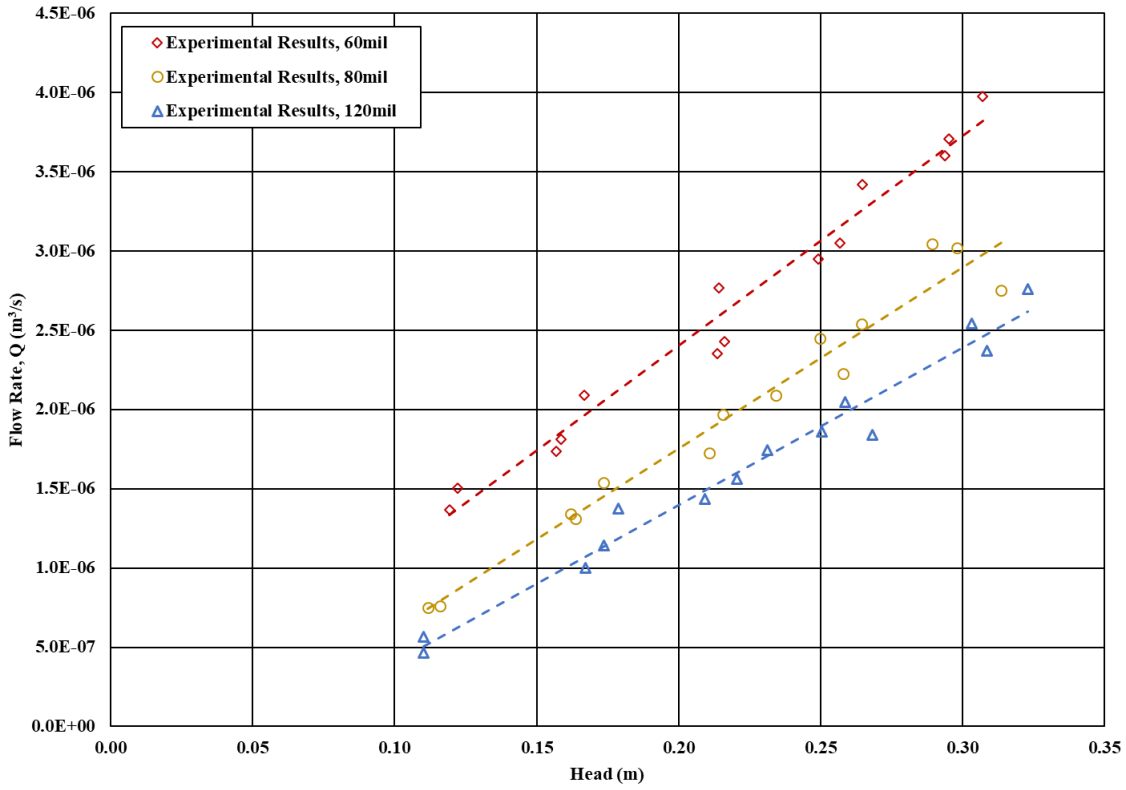

Figure 4.17 Circular defect of diameter 0.0050m with three geomembrane thicknesses

The effect of geomembrane thickness was also evaluated through developing 3D finite element models at experimental scale. The FEMs developed were similar to those discussed in Section 4.3.3. However, an additional surface was created to represent the geomembrane and modified depending on the required thickness. The region within the geomembrane defect itself was also filled with sand, which is not a direct representation of the experimental setup. The zero pressure head boundary condition was applied to the bottom of the sand material in the defect region. The hydraulic conductivity of the sand used for these models was 0.0016m/s.

The FEM flow rates were less than those measured during experimental testing for all three geomembrane thicknesses. However, the FEM and experimental results cannot be directly compared for flow rates. The sand within the geomembrane defect region for the FEM, would influence the resulting flow rates. Infilling of the geomembrane defect will result in a lower flow rate than a defect with no infilling (Walton et al., 1997). Although the sand within the

geomembrane defect influences the flow rate, the FEM resulted in the same trend as the experimental results.

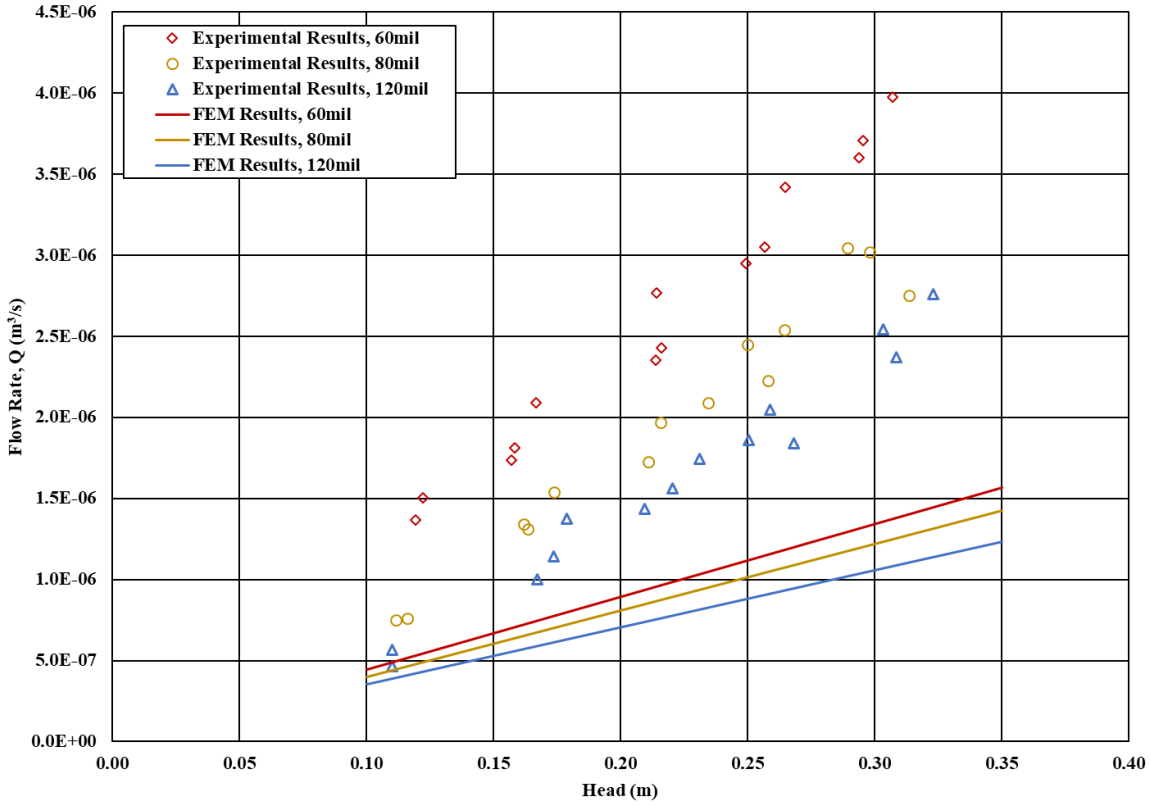

Figure 4.18 Comparison of experimental and FEM results for circular defect of diameter 0.0050m with three geomembrane thicknesses

As the thickness of the geomembrane increased the flow rate through the defect decreased. This is likely due to resistance of the flow as it moves through the stem of the defect (Walton and Sagar, 1990). In turn the hydraulic gradient immediately surrounding the defect is reduced likely due to the decrease in flow rate as the thickness of the geomembrane increases.

Localised hydraulic gradients from the FEMs agree with the findings of Walton and Sagar (1990). The FEM hydraulic gradients for the various thicknesses of geomembrane are found to decrease within increasing thickness. The gradients were also found to increase with increasing hydraulic head above the defect.

Table M FEM maximum hydraulic gradients near the circular defect for three geomembrane thicknesses

Geomembrane Thickness	Hydraulic Head above Defect, h (m)	Maximum Hydraulic Gradient Immediately Surrounding the Defect (m/m)
60mil	0.10	66
	0.20	131
	0.30	197
80mil	0.10	47
	0.20	94
	0.30	141
120mil	0.10	33
	0.20	66
	0.30	98

4.4 Finite Length Elongated Defects on flat Geomembrane Surfaces

4.4.1 Experimental Results

Two elongated defects of areas 3.3E-05m^2 (approximately 0.002m by 0.016m) and 5.4E-05m^2 (approximately 0.002m by 0.0027m) were tested experimentally in the large-scale apparatus. The same set of experimental trials used for the circular defects were completed for the two elongated defect sizes. The elongated defects were placed length-wise with the shorter lengths parallel to the upstream and downstream ends of the apparatus.

Bonaparte et al.'s (1989) proposed solution is only applicable to circular defects. There is no proposed equation for an elongated defect for this geomembrane system. The experimental results for the elongated defects follow the same trend as the circular defects. The larger elongated defect resulted in a greater flow rate. As the hydraulic head above the defect increased the flow rate increased.

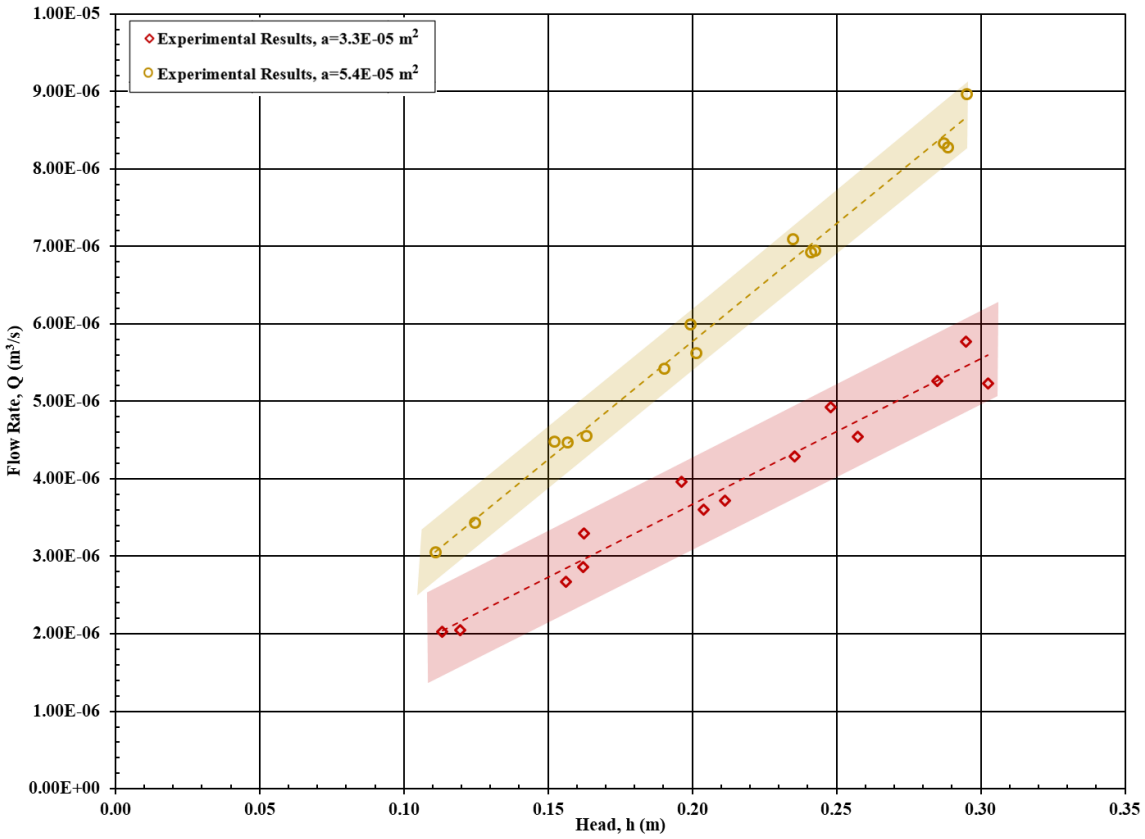

Figure 4.19 Experimental results for elongated defects with 95% prediction interval

4.3.2 Comparison of Experimental Results and Finite Element Model Estimations

The 3D finite element models were developed for the two elongated defects similar to those of the circular defects. The FEM results underestimate the flow rates for both elongated defect sizes when the hydraulic conductivity of the overlying sand was 0.0016m/s. As the defect size and hydraulic head increase the percent error between the experimental and FEM results increases.

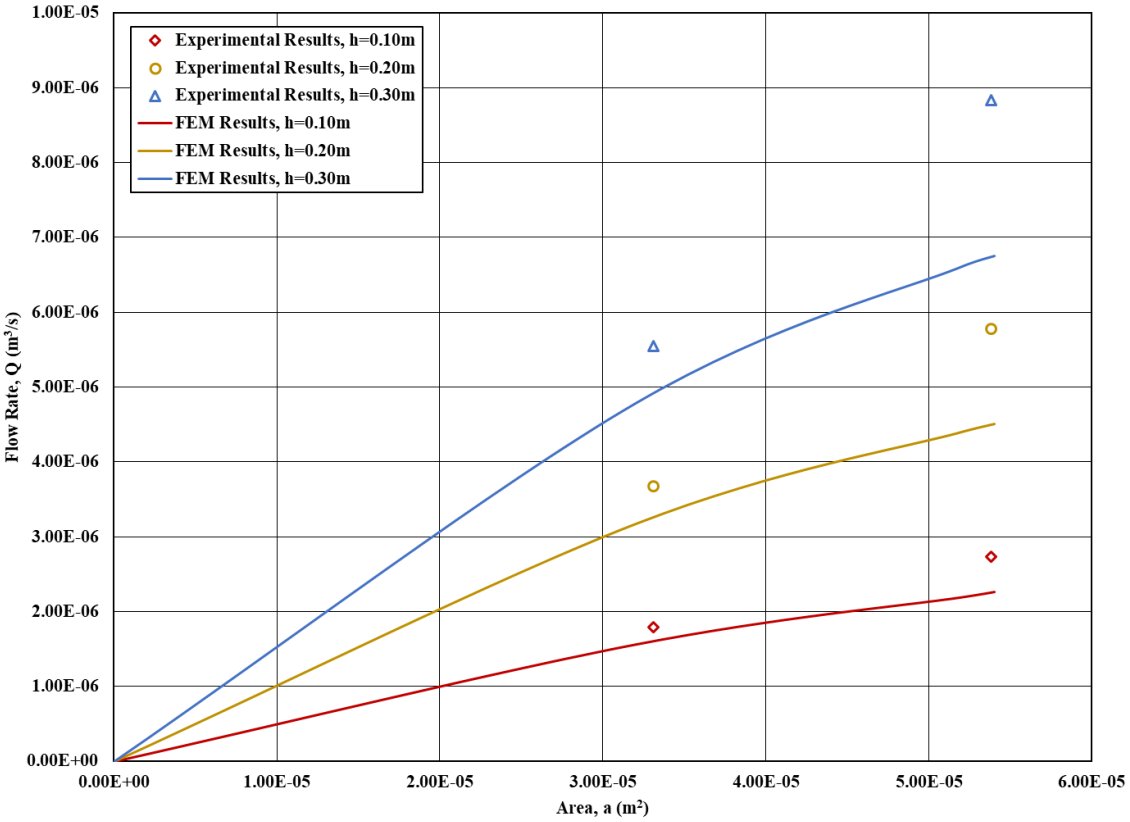

Figure 4.20 Flow rates for experimental and FEM results for elongated defects

The same range of hydraulic conductivities used for the circular defects was applied to the elongated defects at three hydraulic heads (0.10, 0.20, and 0.30m). These FEM results are shown in Figure 4.12. The exact dimensions of the experimentally tested defects could not be analysed using the FEMs. Three areas of 2.4E-05m^2 (dimensions of 0.002m by 0.012m), 4.8E-05m^2 (dimensions of 0.002m by 0.024m), and 5.4E-05m^2 (dimensions of 0.002m by 0.027m) were modelled. Flow rates were then interpolated from the FEM flow rates for the areas tested experimentally.

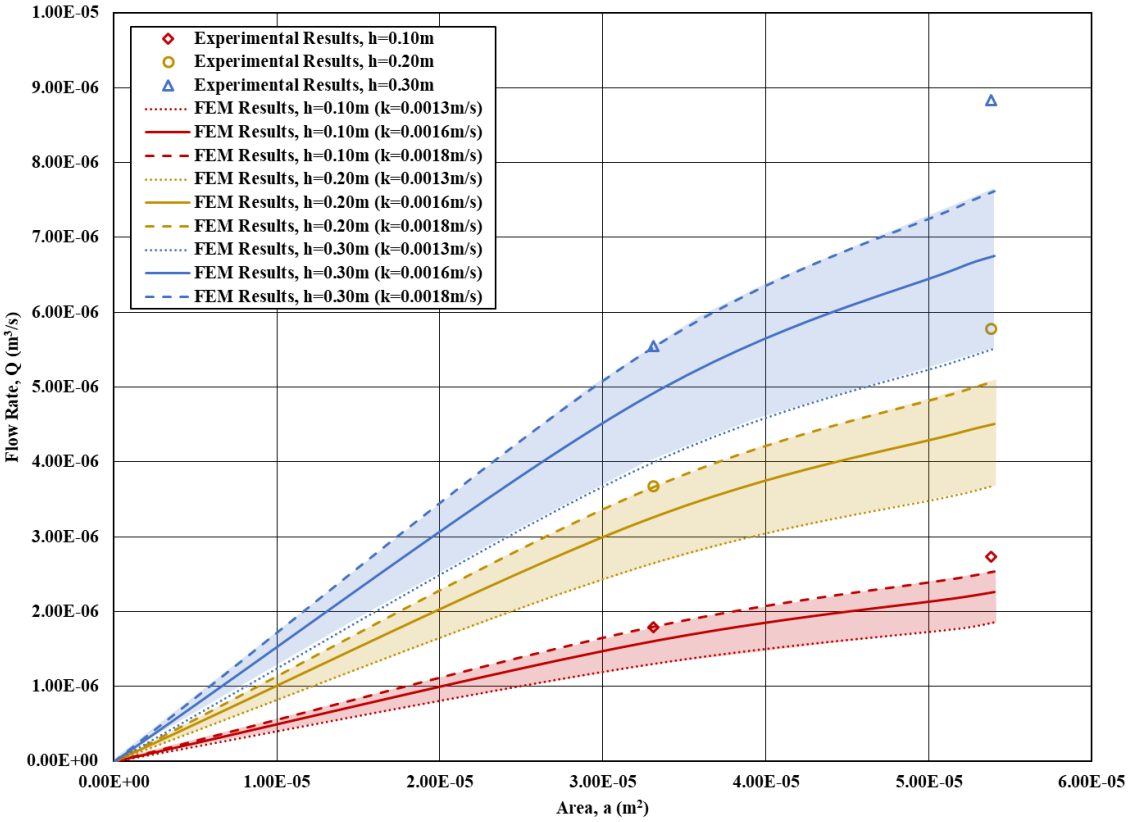

Figure 4.21 Experimental and 3D FEM flow rates for elongated defects with overlying sand having three different hydraulic conductivities

Percent errors were determined for the three hydraulic conductivities used in the finite element models at the experimentally scaled FEMs. The FE results with upper hydraulic conductivity of 0.0018m/s resulted in the best fit for the experimental data. The percent errors for the elongated defects are shown in Table 4.13. FE flow rates were interpolated for experimental defect sizes.

Table N Percent error for elongated defects with overlying sand material at three hydraulic conductivities

Defect Area, a (m^2)	Hydraulic Head above Defect, h (m)	Percent Error for FEM with k=0.0013m/s	Percent Error for FEM with k=0.0016m/s	Percent Error for FEM with k=0.0018m/s
3.3E-05	0.10	38	12	0
	0.20	40	13	1
	0.30	40	14	1
5.4E-05	0.10	48	21	8
	0.20	57	29	14
	0.30	60	31	16

The underestimation of flow rate could be due to the effect of points of singularity within the FEMs. This phenomenon typically occurs when there is an abrupt change in material properties along a boundary or when there is an abrupt change in boundary conditions (Szabo & Babuska, 1991). Boundary conditions where the edges of the defect change suddenly from a no flow condition to a pressure head condition could result in multiple points of singularity.

Points of singularity along the edges of the defect in the FEM could result in lower than expected flow rates. Numerical simulations with circular and elongated defects could be influenced by this effect. The elongated defects would be expected to have a larger number of points of singularity than circular defects due to larger perimeter lengths and straight edges. These points of singularity could be mitigated through beveling or filleting the edges of boundaries of concern. The addition of beveling the defects edges was not analysed within this research.

Scaled-up FEMs were developed for elongated defects of area 2.4E-03m^2, 5.2E-03m^2, and 5.4E-0m^2. Maximum hydraulic gradients immediately surrounding the defect were found for defects at three hydraulic heads. The scaled-up finite element resulted in flow rates that were less than those modelled at the experimental scale. The decrease in flow rates between the models is likely results of better mesh refinement in the scaled-up FEMs.

The trend of the maximum hydraulic gradients immediately surrounding the defects were found to have the same trend as the circular defects. As the hydraulic head increased the localised hydraulic gradient immediately near the defects increased. Although the localised hydraulic gradients were similar for the rectangular defects, the hydraulic gradients decreased within increasing defect area.

Table O Scaled-up FEM maximum hydraulic gradients near the elongated defects

Defect Area, a (m^2)	Hydraulic Head above Defect, h (m)	Maximum Hydraulic Gradient Immediately Surrounding the Defect (m/m)
2.4E-03	0.10	28
	0.20	56
	0.30	84
5.2E-03	0.10	25
	0.20	47
	0.30	68
5.4E-03	0.10	22
	0.20	45
	0.30	67

4.5 Circular Defects on Sloped Geomembrane Surfaces

4.5.1 Experimental Results

A circular defect of diameter 0.0050m was tested in the large-scale constant head apparatus with three applied slopes (2.5%, 5.0%, and 10%). Testing was completed for low hydraulic head with and without horizontal hydraulic gradients. When no horizontal hydraulic gradient is applied the system condition is considered to have minimal vertical flow through the apparatus. A horizontal hydraulic gradient that is greater than zero results in horizontal flow over the top surface of the geomembrane. This was done by setting the ground as the datum.

Figure 4.22 illustrates the comparison of the 0.0050m diameter defect with and without an applied slope and with no horizontal hydraulic gradient across the defect. The results indicate that there is an effect on the flow rate with and without a slope when there is no vertical flow occurring across the apparatus. However, the degree of slope does not appear influence the flow rate for these conditions. Due to the limited number of tests completed for the sloped defects, it cannot be firmly concluded that slope does not influence the flow through a defect where there is no horizontal hydraulic gradient applied.

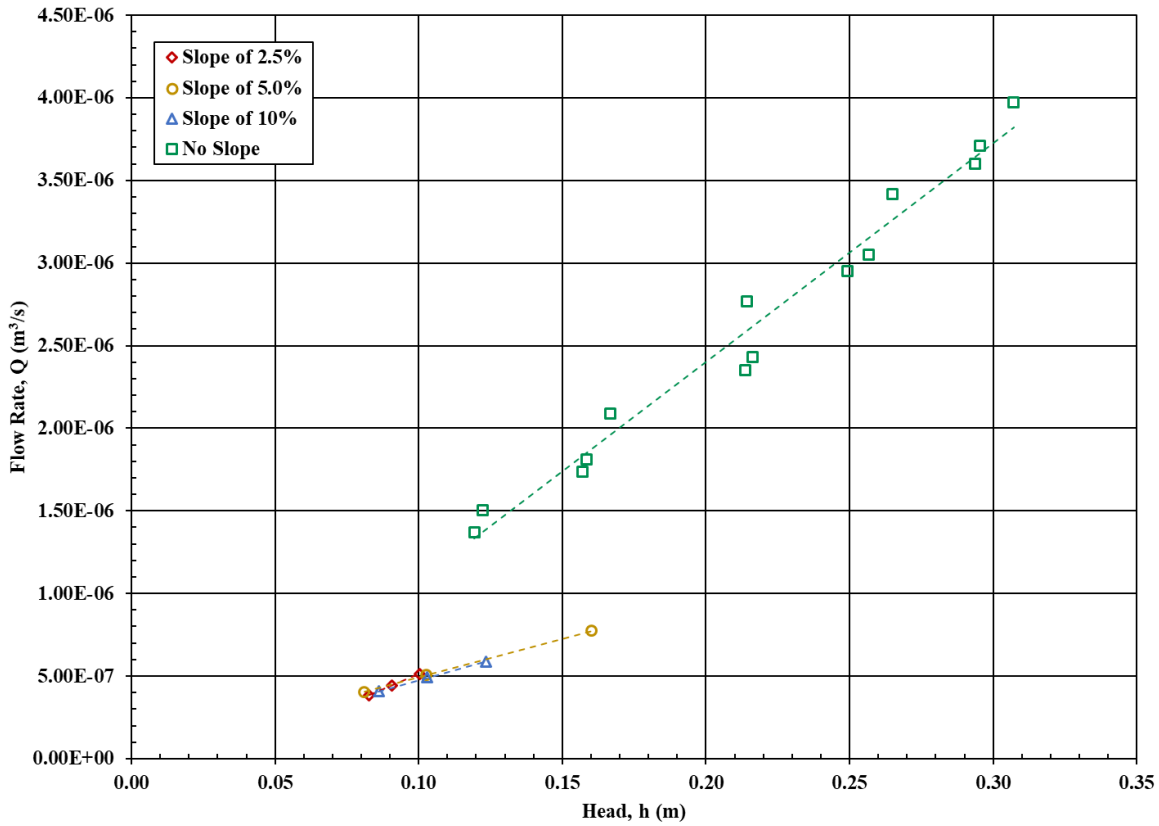

Figure 4.22 Comparison of experimental flow rates for circular defect of diameter 0.0050m with and without an applied slope and no horizontal hydraulic gradient

From the experimental results it can be seen that a horizontal hydraulic gradient has a more significant influence on the flow rate when there is a slope applied to the system. The experimental results indicate that the flow rate through the defect increases when there is flowing conditions across the geomembrane.

Different horizontal hydraulic gradients were applied to the 0.0050m diameter defect for the different slopes. The 2.5% and 5.0% slopes had similar hydraulic gradients ranging between 0.1 and 0.2m/m, and the 10% slope had hydraulic gradients closer to 0.3m/m.

A firm conclusion cannot be stated on the effect of the hydraulic gradient between the results of the different sloped tests due to limited trials. However, the flow rates with horizontal hydraulic gradients greater than zero resulted in similar flow rates for all three slopes. Figure 4.23 shows the experimental testing results for all the sloped trials completed with and without horizontal hydraulic gradients applied across the defect.

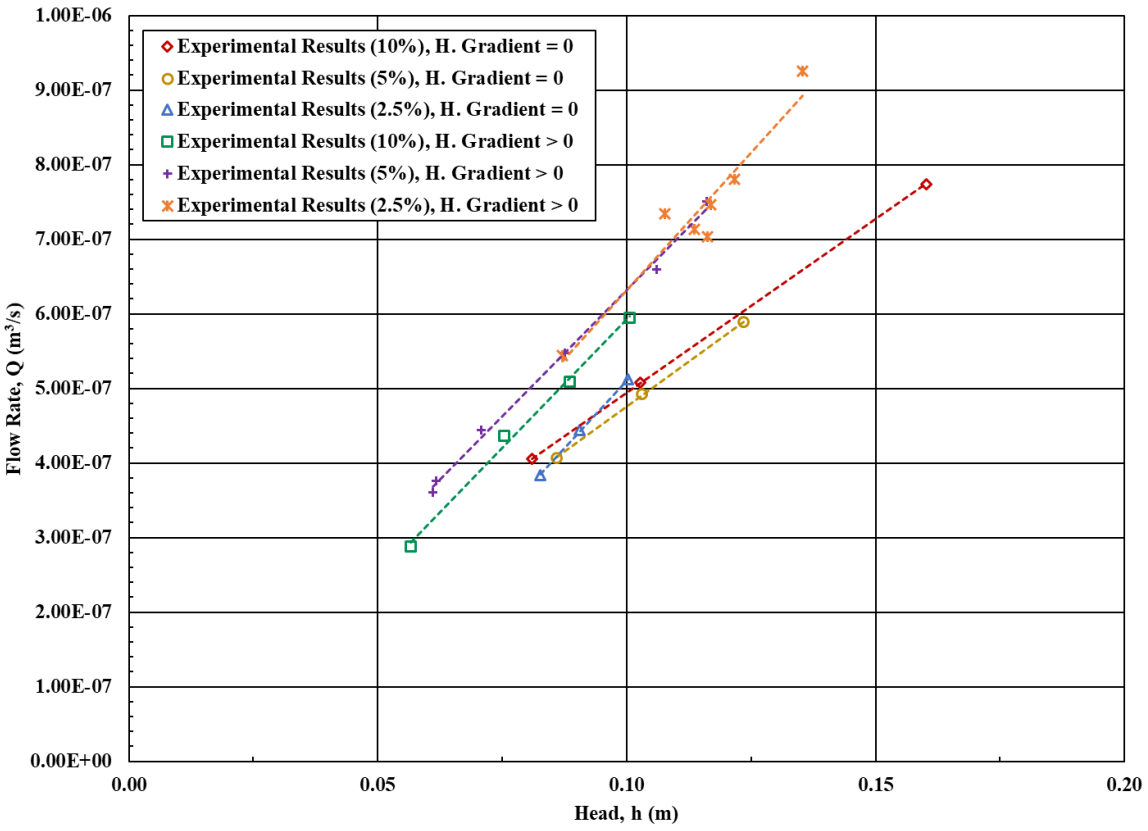

Figure 4.23 Comparison of experimental flow rates for circular defect of diameter 0.0050m with and without horizontal hydraulic gradients across the defect

4.5.2 Comparison of the Experimental Results and Finite Element Model Estimations

The developed 3D FEM results found that the horizontal hydraulic gradient had a minimal effect on the defect flow rate. For all three slopes, the resulting percent error between the FEM flow rates with and without a horizontal hydraulic gradient ranged between 4 to 8%. Figure 4.15 illustrates the FEM results of a 0.0050m diameter defect for three slopes at low hydraulic heads. These models did not include a geotextile region between the defect and the overlying sand.

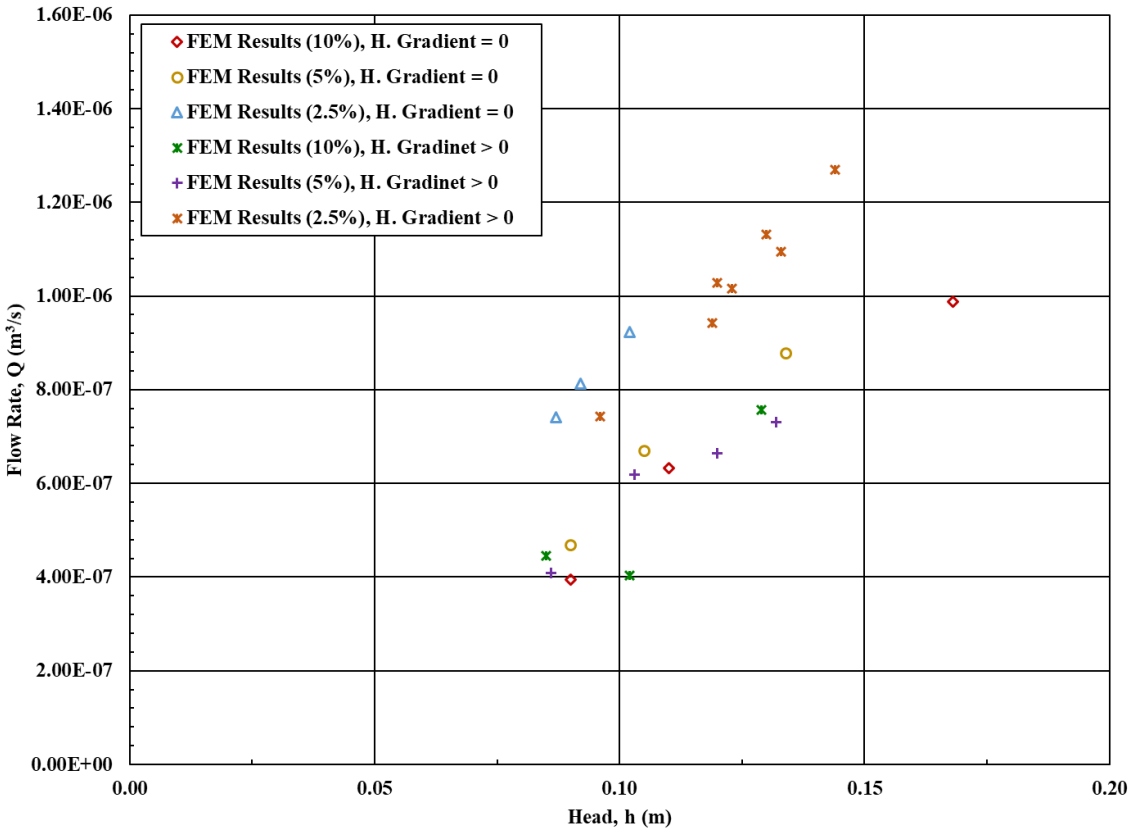

Figure 4.24 FEM results for 0.0050m diameter defect for three slopes with and without horizontal hydraulic gradients

Percent error between the experimental and FE results ranged between absolute values of 1 to 48%, with an average percent error of 24%. Comparing the hydraulic head profiles between the experimental and FEMs resulted in higher percent errors than those found for the defects on a flat geomembrane surface. The percent errors ranged between 0 and 27% with an average percent error of 8%. The large percent errors occurred at the manometers that were furthest from the defect. This is likely due to the increased difficulty in maintaining the desired head throughout the large-scale apparatus.

Localised hydraulic gradients were determined from the FEMs developed for each of the slopes at the various hydraulic heads achieved experimentally (Table 4.15 to 4.17). The results indicate that lower hydraulic heads had lower corresponding hydraulic gradients. The slope of the geomembrane influenced the resulting maximum localised hydraulic gradients within the FEMs ($F = 28.1$).

Table P FEM Maximum hydraulic gradients immediately surrounding the for 0.0050m diameter defect on a 2.5% slope

Hydraulic Head above Defect, h (m)	Horizontal Hydraulic Gradient	Maximum Hydraulic Gradient Immediately Surrounding the Defect (m/m)
0.087	0.01	67
0.108	0.01	88
0.114	0.01	96
0.116	0.01	98
0.117	0.01	102
0.122	0.01	104
0.135	0.01	120
0.083	0.00	67
0.091	0.00	73
0.100	0.00	84

Table Q FEM Maximum hydraulic gradients immediately surrounding the 0.0050m diameter defect on a 5.0% slope

Hydraulic Head above Defect, h (m)	Horizontal Hydraulic Gradient	Maximum Hydraulic Gradient Immediately Surrounding the Defect (m/m)
0.071	0.02	20
0.088	0.01	37
0.106	0.01	60
0.116	0.02	69
0.086	0.00	43
0.103	0.00	45
0.124	0.00	83

Table R FEM Maximum hydraulic gradients immediately surrounding the 0.0050m diameter defect on a 10% slope

Hydraulic Head above Defect, h (m)	Horizontal Hydraulic Gradient	Maximum Hydraulic Gradient Immediately Surrounding the Defect (m/m)
0.057	0.03	18
0.075	0.03	20
0.101	0.03	33
0.081	0.00	67
0.103	0.00	73
0.160	0.00	84

4.5.3 Refined Equation for Flow through a Circular Geomembrane Defect

As shown in Section 4.3.2 the current empirical solution significantly overestimates the flow rate through a circular defect. The Bonaparte et al. (1989) proposed equation does not take into consideration the effect of thickness of the geomembrane on the flow through a defect.

Using a multiple variable regression in SPSS, a new equation was developed to estimate the flow through a geomembrane defect. The developed equation is only applicable to a sand with a hydraulic conductivity of 0.0016m/s, as this is the only material that was analysed in this research.

$$Q = 0.015 * k * t^{-0.64} * a^{0.43} * h^{1.21} \quad (4.1)$$

Where k is hydraulic conductivity equal to 0.0016m/s, t is the geomembrane thickness (m), a is the area of the circular defect (m^2), and h is the hydraulic head above the defect (m).

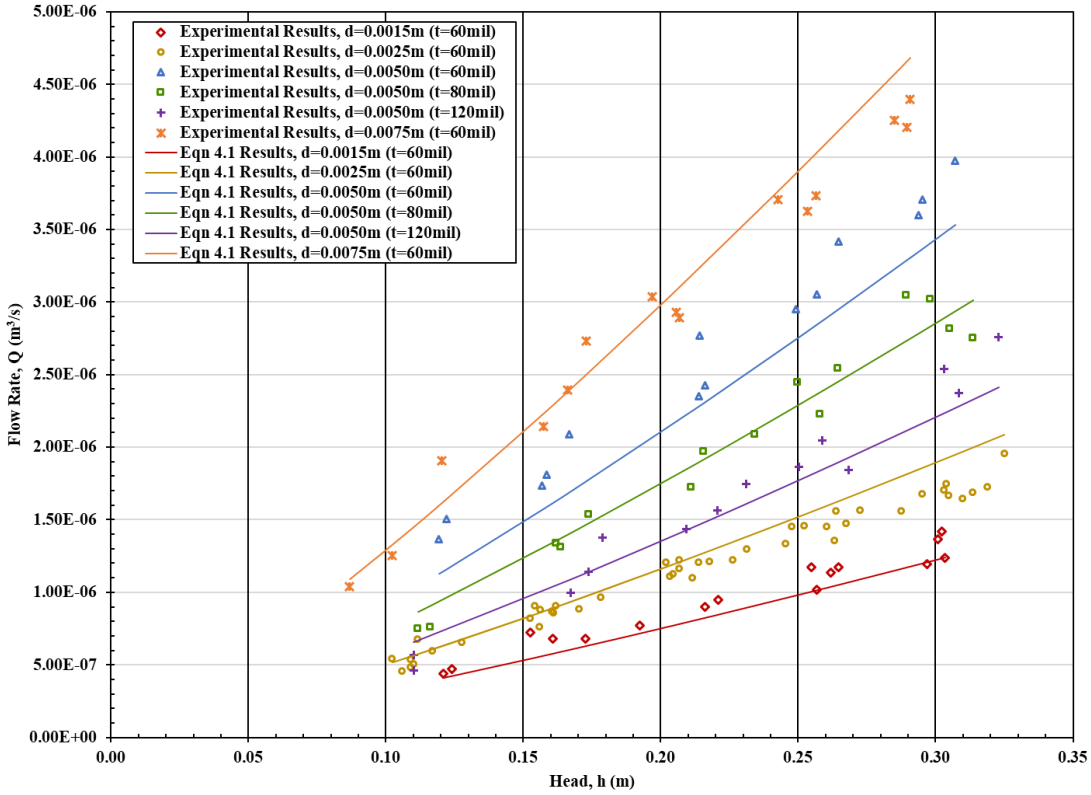

Figure 4.25 Experimental results with Equation 4.1 results for circular defects

4.6 Correction Factors for Bonaparte et al. (1989) Equation for Circular Defects

Comparing the proposed empirical equation to Equation 4.1 allowed for the development of correction factors. The correction factors can be applied to the empirical equation (Equation 2.5) to estimate the flow rate for different circular defect sizes at various hydraulic heads. These corrections are made for a system where the overlying material has a hydraulic conductivity of 0.0016m/s. Figure 4.26 illustrate correction factors for various circular defect sizes with a range of hydraulic heads above the defect. Figure 4.27 illustrates correction factors for different hydraulic heads over a range of defect sizes.

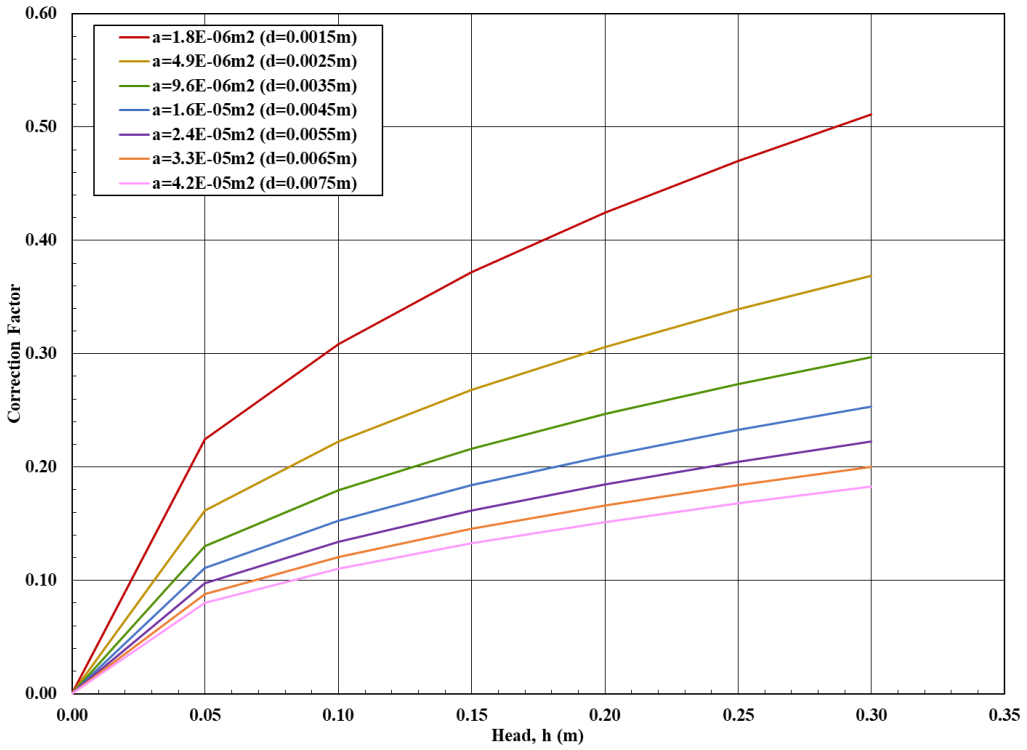

Figure 4.26 Correction factor chart for hydraulic head above the defect for various defect sizes

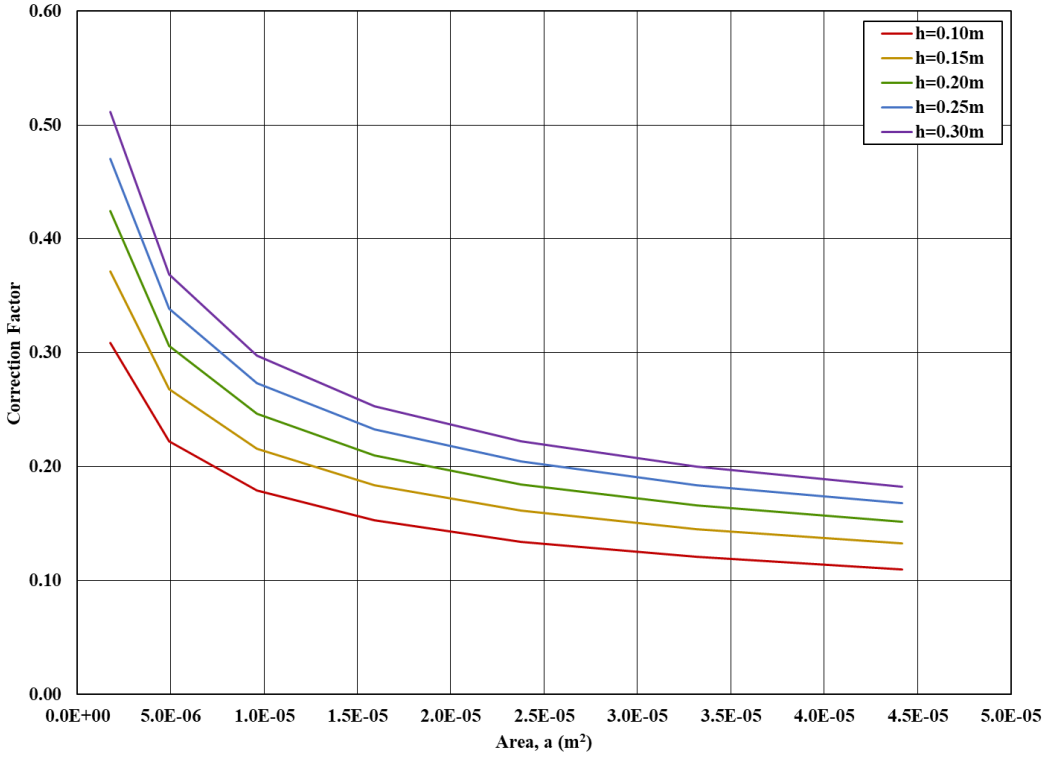

Figure 4.27 Correction factor chart for defect area at various hydraulic head above the defect

4.7 Chapter Summary

Experimental results were evaluated against the applicable empirical equation, 2-dimensional axisymmetric and 3-dimensional finite element models. Defect size and shape, hydraulic head above the defect, hydraulic gradient across the system, geomembrane thickness, and geomembrane slope were all evaluated for their influence on flow through a geomembrane defect.

The proposed empirical solution resulted in the highest overestimation of flow rate through circular defects. This equation was applicable to only circular defects on flat geomembrane surfaces. No empirical solutions are available for comparison of flow rates through rectangular and circular defects on sloped geomembrane surfaces.

Both the 2D and 3D numerical models resulted in overestimations for circular defects on flat geomembrane surfaces. The 3D FEMs provided better estimates of flow than the 2D models. FEMs developed for the circular defect on a sloped geomembrane surface and elongated defects were found to underestimate the flow rate through the geomembrane defect.

Horizontal hydraulic gradient was found to have an insignificant effect on flow rate for both experimental and finite element model results. Hydraulic head profiles obtained from 2D and 3D models were comparable to those measure experimentally. The hydraulic gradients immediately around a geomembrane defect could not be measured experimentally. However, within the 3D FEMs the highest hydraulic gradients were found immediately around the defects.

The localised hydraulic gradients were found to increase with decreasing defect size for both the circular and elongated defects. The smallest circular defect resulted in highest maximum hydraulic gradients. Localised hydraulic gradients were also found to increase with increasing hydraulic head above the geomembrane defect. Localised hydraulic gradients for circular defects on sloped surfaces were found to independent of the slope.

Equation 4.1 was developed from the experimental results measured during the laboratory program using a multiple variable regression analysis. The equation includes the parameters; circular defect size, hydraulic head above the defect, and thickness of the geomembrane. This equation was developed for one material which was used during experimental testing.

5 Summary & Conclusions

5.1 Study Objectives

The objectives of this study are stated in Section 1.2. The purpose of this research was to determine the cause of the discrepancy between the experimental flow rates through geomembrane defects compared to the proposed empirical estimation. The experimental testing was completed using a large-scale constant head apparatus and numerical modelling.

To achieve the project objectives, the research was completed as follows:

- Primary and secondary experimental testing was completed using the large-scale constant head apparatus following the laboratory program outlined in Section 3.3.
- Experimental results were compared to the appropriate proposed solution by Bonaparte et al. (1989).
- Both 2D and 3D finite element models where developed to evaluate the experimental results and determine the immediate conditions occurring around the geomembrane defect.

Chapter 2 outlined the previous research completed on evaluating flow through geomembrane defects and the resulting empirical equations. The results achieved through the completion of the laboratory program are discussed and analyzed in Chapter 4.

5.2 Summary

5.2.1 Empirical Solution Evaluation

The empirical solution applicable to the experimental testing was proposed by Bonaparte et al. (1989). This equation was developed for a circular geomembrane defect being overlain by a lesser permeable medium such as a sand or fine gravel, which is the limiting material as it impedes the flow towards the defect (Bonaparte et al., 1989). An analytical solution developed by Giroud et al. (1997c) was developed as a replacement for the empirical solution, though it was not evaluated for this research as it is not based upon experimental data.

The empirical equation was developed through theoretical analysis and the completion of limited laboratory experiments. The authors selected the lower bound solution to be the equation for radial

flow towards the geomembrane defect and an upper bound solution of Bernoulli's equation. The developed equation was obtained by using the chosen upper and lower bound solutions and averaging the logarithms of the leakage rate (Bonaparte et al., 1989).

Similar to other empirical solutions it is assumed that Darcy's law holds true within the surrounding porous media (Bonaparte et al., 1989; Touze-Foltz et al., 1999; Giroud & Bonaparte, 1989; Giroud et al., 1997b; Walton et al., 1997). The effect of high velocity, localised hydraulic gradients around the defect are not factored into the empirical estimation. The large-scale experimental testing and FEMs allowed for the evaluation of these high velocity hydraulic gradients immediately around the defect.

Comparing the empirical estimation and experimental flow rates for circular geomembrane defects resulted in correction factors ranging between 12 and 55%. The comparison found that as the defect size increased the correction factor increased. Further examination was completed through developing 2D and 3D numerical models.

5.2.2 Large-Scale Constant Head Apparatus Experimental Testing

Data was collected using the large-scale constant head apparatus for four circular defect sizes and two elongated defect sizes on flat geomembrane surfaces and one circular defect size on three different geomembrane slopes. The effect of five different factors was evaluated through experimental testing: hydraulic head above the defect; horizontal hydraulic gradient across the defect; dimensions of the defect (size and shape); geomembrane thickness; and sloping of the geomembrane surface.

The experimental flow rates increased with increasing defect size and increasing hydraulic head over the defect. The general trend of flow rate matched the expected trend found in the literature. The shape of the geomembrane defect influences the flow rate. The elongated defects resulted in higher flow rates than the circular defects of similar area based on experimental and numerical results.

The thickness of the geomembrane was found to have an influence of the flow rate through the defect. Three geomembrane thicknesses (60, 80, and 120mil) were tested with the same size defect (diameter of 0.0050m). As the thickness of the geomembrane increased the flow through the defect

decreased. The thicker the geomembrane the more resistance there is for flow to move through the stem of the defect resulting in a reduction of flow (Walton & Sagar, 1990).

Hydraulic head profiles were measured throughout experimental testing for each geomembrane defect. These profiles ensured that the hydraulic head within the apparatus reached and maintained a steady-state equilibrium. The hydraulic head distribution throughout the apparatus allowed for the determination of horizontal hydraulic gradient across the system. The horizontal hydraulic gradient was found to have an insignificant effect on the flow rate through a defect on a flat geomembrane surface.

However, when a slope was applied to the apparatus the influence of the horizontal hydraulic gradient was significant. A horizontal hydraulic gradient greater than zero across the geomembrane defect resulted in flow rates greater than when the hydraulic gradient was equal to zero. The flow rate through the circular defect for the three slopes tested was similar when the hydraulic gradient was equal to zero.

The non-woven needle punched geotextile used during experimental testing had different in-plane and cross-plane hydraulic conductivities. The geotextile was not specifically included in all the finite element models. The models on interest for including the geotextile were the FEMs with a circular defect on a sloped geomembrane surface due to the greater influence of hydraulic gradient on the flow rate.

Flow velocity and hydraulic gradients immediately surrounding the defect could not be measured within the large-scale apparatus. The discrepancy between the empirical estimation and experimental data was assumed to be due to effects of higher velocity flows and high localised hydraulic gradients occurring immediately around the geomembrane defect. Finite element modelling was used to evaluate the effects that could not be measured directly from the large-scale constant head apparatus.

5.2.3 Finite Element Modelling

5.2.3.1 Circular Defects on a Flat Geomembrane Surface

Numerical modelling was used to examine the experimental results for flow characteristics that could not be determined experimentally. The finite element software SEEP/W (GeoStudio, 2012) was used to develop 2D FEMs and SVFLUX/GE (SoilVision, 2017) was used to develop 2D and 3D numerical models. FEMs were developed to evaluate the flow characteristics occurring immediately around the defect.

The software used to develop the 2D axisymmetric numerical models was found to estimate similar flow rates through circular defects. The slight difference in the estimations between the models was likely due to differences in software calculations for the flow rate measurement. The percent error for the experimental and 2D models ranged between -17 to -40% and -14 to 38% for SVFLUX/GE and SEEP/W models, respectively.

3D finite element models resulted in the best estimation of the flow through circular geomembrane defects. The various hydraulic conductivities used in the FEMs were determined through the completion of constant head permeameter tests within the large-scale apparatus. Evaluating multiple hydraulic conductivities within the FEMs allowed for further evaluation of an addition parameter and influencing factor on the flow rate. The various hydraulic conductivities allowed the FEMs to better match experimental results for different hydraulic heads.

The models allowed for the comparison of hydraulic head profiles to the experimentally measured values. Hydraulic head profiles between the experimentally measured values and FEMs showed similar drawn down effects. The percent error of the hydraulic head profiles ranged between 0 and 3%.

Hydraulic gradients immediately surrounding the defect could be analysed using 3D FEMs. The highest localised hydraulic gradients were found immediately around the geomembrane defect. The maximum hydraulic gradients were found to increase with decreasing defect size and increasing hydraulic head above the defect. These high hydraulic gradients indicate the potential onset of high velocity, non-Darcian flow characteristics occurring in the porous media immediately around the defect.

5.2.3.2 Effect of Geomembrane Thickness on Flow Rate through a Defect

Experimental testing was completed on three geomembrane thicknesses for one size of circular defect. A 0.0050m diameter defect was evaluated for flow rate through 60mil, 80mil, and 120mil smooth geomembrane.

Few authors have evaluated the influence of geomembrane thickness on the flow rate through a defect (Brown et al., 1987; Priyantha et al., 1988; Walton & Sagar, 1990; Benson et al., 1995; Rowe et al., 2016). Some findings indicated geomembrane thickness had an insignificant effect on flow rate or that other factors had a greater influence on flow and thus thickness was not evaluated (Brown et al., 1987; Priyantha et al., 1988; Benson et al., 1995). Another author found that thickness may have a significant effect on the flow rate but due to lack of data no conclusion could be made (Rowe et al., 2016).

Walton and Sagar (1990) analyzed flow through small flaws in membrane liners. The thickness of a geomembrane results in a resistance of flow through the flaw or defect and results in a head loss within the system (Walton & Sagar, 1990). The authors' findings indicated smaller defects result in more resistance through the stem of the defect. In addition, Walton & Sagar (1990) found the size of the defect has a more significant effect on the flow rate through thinner membranes.

The experimental results using the large-scale apparatus demonstrated that the thickness of the geomembrane was significant when evaluating the flow through a defect. As the geomembrane thickness increases the flow through the defect will decrease. The results align with the findings of Walton and Sagar (1990).

The 3D FEMs developed for evaluating the influence of geomembrane thickness support the experimental results. The experimental system and FEM flow rates cannot be directly compared as the geomembrane system are not exactly equivalent. The finite element models required the defect to be infilled with sand. The gradients found using the FEMs were assessed for the different defect sizes and hydraulic heads above the defect.

The FEM gradients correspond to Walton and Sagar's (1990) conclusion that there is a greater resistance of flow through smaller defects. The localised hydraulic gradients were found to increase with decreasing defect size and with increasing head above the defect.

5.2.3.3 Elongated Defect on Flat Geomembrane Surface

The experimental results could not be compared to an empirical solution as currently there are no solutions developed for this geomembrane system for elongated defects. The 3D FEMs developed for the elongated defects resulted in an underestimation of the flow rate. These results differed from the circular defects, which overestimated the flow rate. Applying a range of hydraulic conductivities to the models allowed for the FEMs to better match the experimental flow rates at higher hydraulic conductivities.

The underestimation of flow rate can be due to the effect of points of singularity within the FEMs. Abrupt changes in boundary conditions or material properties can result in these points of singularity (Szabo & Babuska, 1991). Points of singularity along the edges of the defect in the FEM could result in lower than expected flow rates. Both FEMs with circular and elongated defects could be influenced by this effect. Elongated defects could be more highly influenced by these points of singularity than circular defects due to the straight edges and greater perimeters.

5.2.3.4 Circular Defect on a Sloped Geomembrane Surface

The effect of the slope of a geomembrane on the flow rate through a defect has not been examined in the literature. Slope was found to cause a significant decrease in the defect flow rate in comparison to a flat geomembrane surface.

Two scenarios of hydraulic gradients were tested with three applied slopes. When the horizontal hydraulic gradient was equal to zero it was representative of a condition where ponding occurred over a geomembrane liner. When the horizontal hydraulic gradient was greater than zero it corresponded with low head flows over a geomembrane system such as a cover system.

The experimental results found that the flow through the defect was greater when the hydraulic gradient was greater than zero. The non-woven needle punched geotextile had a greater in-plane hydraulic conductivity than its cross-plane conductivity. When the geotextile was included in the FEMs with sloped geomembranes the flow rates were lower than the models without the geotextile. The geotextile addition resulted in lower percent error between the FEMs and experimental results.

The FEMs found that the hydrostatic and flow conditions resulted in the same flow rates regardless of the horizontal hydraulic gradient. The resulting obtained within the models indicated that the applied slope within the models was not an influence of the maximum hydraulic gradients immediately around the defect.

Non-Darcian effects may be the cause of the differences found experimentally with the hydrostatic and flow conditions. However, finite element models do not model the individual pore spaces and thus a firm conclusion cannot be stated on the cause of the differences in flow rates found experimentally.

5.3 Future Research

The completion of this research allowed for the analysis of a geomembrane system comprised of a less permeable medium overlying the geomembrane than the underlying material. This is only one geomembrane system of many that have had empirical solutions developed for evaluating flow through geomembrane defects. Areas that require additional research are summarized below.

The material overlying this geomembrane system is a controlling factor for the flow through the geomembrane defect. Only one soil was analyzed as the overlying material in this research. The newly developed empirical solution is only applicable for a material of hydraulic conductivity 0.0016m/s. Thus more research should be completed on the sensitivity and influence of the overlying materials' hydraulic conductivity and how a material's porosity affects geomembrane defect flow rates.

The limitations of finite element modelling do not allow for examining the potential non-Darcian effects occurring within the pore spaces immediately surrounding the defect. Further modelling should be completed to evaluate these effects. Discrete element modelling would allow for a refined evaluation of fluid flow effects within individual pore spaces. Further modelling would allow for a firm conclusion regarding the influence of turbulent flows within pore spaces.

A geomembrane system like the one analyzed in this research is comparable to a field application of a secondary drainage system. Geomembranes are commonly placed over compacted clay liners or low conductivity material. Further research should be completed using the large-scale constant

head apparatus on other applicable geomembrane systems, such as composite geomembrane barrier systems to determine if the same potential non-Darcian effects are occurring.

Lastly, sloped geomembranes are common in both liner and cover system applications. There is minimal knowledge regarding flow rate through a geomembrane defect on a slope. Further study should be completed on sloped geomembrane defects to allow for a more comprehensive understanding of the influence of slope on defect flow rate.

This research is not applicable to all geomembrane systems. The intent of this research is to provide a better estimation of the expected flow rates through geomembrane defects for the geomembrane system outlined in this research.

References

Barak, A. Z. (1987). Comments on 'High velocity flow in porous media' by Hazzanizadeh and Gray. *Transport in Porous Media, 2*, 533-535.

Barroso, M. (2005). *Fluid migration through geomembrane seams and through the interface between geomembrane and geosynthetic clay liner.* Universite Joseph-Fourier.

Barroso, M., Lopes, M., & Bergamini, G. (2010). Effect of the waste pressure on fluid migration through geomembrane defects. *9th International Conference on Geosynthetics*, (pp. 959-962). Brazil.

Bear, J. (1972). Dynamics of Fluid in Porous Media. *Elzevier*.

Benson, C., Tinjum, J., & Hussin, C. (1995). Leakage Rates for Geomembrane Liners Containing Holes. *Geosynthetics*, *95*, pp. 745-758.

Bonaparte, R., Giroud, J., & Gross, B. (1989). Rates of Leakage Through Landfill Liners. (pp. 18-29). San Diego: Geosynthetics Conference.

Bouazza, A., & Vangpaisal, T. (2006). Laboratory investigation of gas leakage rate through a GM/GCL composite liner due to a circular defect in the geomembrane. *Geotextiles and Geomembranes*, *24*, 110-115.

Bouazza, A., Vangpaisal, T. H.-N., & Kodikara, J. (2008). Analytical modelling of gas leakage rate through a geosynthetic clay liner-geomembrane composite liner due to a circular defect in the geomembrane. *Geotextiles and Geomembranes, 26*, 122-129.

Brown, K., Thomas, J., Lytton, R., Jayawickrama, P., & Bahrt, S. (1987). *Quantification of Leak Rates through Holes in Landfill Liners.* Office of Research and Development, US Environmental Protection Agency.

Buss, S., Butler, A., Johnston, P., Sollars, C., & Perry, R. (1995, August 9). Mechanisms of Leakage through Synthetics Landfill Liner Materials. *J. CIWEM*, 353-359.

Cartaud, F., Touze-Foltz, N., & Duval, Y. (2005). Experimental investigation of the influence of a geotextile beneath the geomembrane in a composite liner on the leakage through a hole in the geomembrane. *Geotextiles and Geomembranes, 23*, 117-143.

Chai, J.-C., Miura, N., & Hayashi, S. (2005). Large-scale Tests for leachate flow through composite liner due to geomemrbane defects. *Geosynthetics International, 12*(3), 134-144.

Chilton, T. H., & Colburn, A. P. (1931). Pressure drop in packed tubes. *Industrial and Engineering Chemistry, 23*(8), 913-919.

Chou, A., Rowe, R. K., & Brachman, R. W. (2017). A test to assess erosion through a geomembrane defect. *Canadian Geotechnical Society*. Ottawa.

Davila, L., & Palmeira, E. (2014). Study of flow through mechanical damages in PVC geomembranes under high hydraulic heads. *10th International Conference on Geosynthetics*, (pp. 2528-2534). Berlin.

De Nevers, N. (1991). *Fluid mechanics for chemical engineers (2nd ed.).* New York: McGraw-Hill.

El-Zien, A., McCarroll, I., & Touze-Foltz, N. (2012). Three-Dimensional finite element analyses of seepage and contaminant transport through composite geosynthetics clay liners with multiple defects. *Geotextiles and Geomembranes, 33*, 34-42.

Faure, Y. H. (n.d.). Design of drain beneath geomembranes: discharge estimation and flow patterns in case of leak. *International Conference on Geomembranes, 2*, pp. 463-468.

Foose, G. J. (1997). *Leakage Rates and Chemical Transport through Composite Landfill Liners.* Madison: University of Wisconsin.

Foose, G., Benson, C., & Edil, T. (2001). Predicting Leakage through Composite Landfill Liners. *J. Geotech. Geoenvironmental Engineering, 127*, 510-520.

Fourar, M., Radilla, G., Lenormand, R., & Moyne, C. (2004). On the non-linear behavior of a laminar single-phase flow through two and three-dimensional porous media. *Advances in Water Resources, 27*, 669-677.

Fredlund, D., & Xing, A. (1994). Equations for the soil-water characteristic curve. *Canadian Geotechnical Journal, 31*, 521-532.

Fukuoka, M. (1986). Large scale permeability tests for geomembrane-subgrade system. *3rd International Conference on Geotextiles. 3*, pp. 917-922. Balkema Publishers.

Gan, L., Shen, Z., Yan, Z., & Ren, H. (2014). Numerical Simulation of Gemembrane Defect Leakage by Saturated-unsaturated Seepage Method. *Advanced Materials Research, 904*, 474-478.

Giroud, J. (1997). Equations for Calculating the Rate of Liquid Migration Through Composite Liners due to Geomembrnae Defects. *Geosynthetics International, 4*(3-4), 335-348.

Giroud, J., & Bonaparte, R. (1989a). Leakage through Liners Constructed with Geomembranes -- Part 1. Geomembrane Liners. *Geotextiles and Geomembranes, 8*, 27-67.

Giroud, J., & Bonaparte, R. (1989b). Leakage through Liners Constructed with Geomembranes-- Part II. Composite Liners. *Geotextiles and Geomembranes, 8,* 71-111.

Giroud, J., Badu-Tweneboah, K., & Bonaparte, R. (1992). Rate of Leakage Through a Composite Liner due to Geomembrane Defects. *Geotextiles and Geomembranes, 11*(1), 1-28.

Giroud, J., Badu-Tweneboah, K., & Soderman, K. (1995). Theoretical analysis of geomembrane puncture. *Geosynthetics International*, 1019-1048.

Giroud, J., Gross, B., Bonaparte, R., & McKelvey, J. (1997a). Leachate flow in leakage collection layers due to defects in geomembrane liners. *Geosynthetics International, 4*(3-4), 215-292.

Giroud, J., Khatami, A., & Badu-Tweneboah, K. (1989). Evaluation of the Rate of Leakage through Composite Liners. *Geotextiles and Geomembranes, 8*(4), 337-340.

Giroud, J., Khire, M., & McKelvey, J. (1997b). Rate of leachate migration through a defect in a geomembrane underlain by a saturated permeable medium. *Geosynthetics International, 4*(3-4), 323-334.

Giroud, J., Khire, M., & Soderman, K. (1997c). Liquid Migration through Defects in a Geomembrane Overlain and Underlain by Permeable Media. *Geosynthetics International, 4*(3-4), 293-321.

Giroud, J., King, T., Sanglerat, T., Hadj-Hamou, T., & Khire, M. (1997d). Rate of liquid migration through defects in a geomembrane placed on a semi-permeable medium. *Geosynthetics International, 4*(3-4), 349-372.

Hassanizadeh, M. S., & Gray, W. G. (1987). High velocity flow in porous media. *Transport in Porous Media, 2*, 521-531.

Katsumi, T., Benson, C., Foose, G., & Kamon, M. (2001). Performance-based design of landfill liners. *Engineering Geology, 60*, 139-148.

Knight, M. A., & Kotha, S. M. (2001). Measurement of geotextile-water characteristic curves using a controlled outflow capillary pressure cell. *Geosynthetics International , 8*(3), 271-282.

Ma, H., & Ruth, D. W. (1993). The microscopic analysis of high forchheimer number flow in porous media. *Transport in Porous Media, 13*, 139-160.

Mei, C. C., & Auriault, J. L. (1991). The effect of weak inertia on flow through a porous media. *Journal of Fluid Mechanics, 222*, 647-663.

Muller, W. W. (2006). 7.5 Influence of Holes in Geomembranes. In W. W. Muller, *HDPE Geomembranes in Geotechnics* (pp. 283-302). Springer.

Nararro, V., Candel, M., Yustres, A., & Garcia, B. (2008). Seepage through side slopes of small water impoundments. *Geosynthetics International, 15*(4), 296-303.

Priyantha, W., Jayawickrama, K. W., Thomas, J. C., & Lytton, R. L. (1988). Leakage Rates through Flaws in Membrane Liners. *Journal of Environmental Engineering, 114*(6), 1401-1420.

Rowe, R. K., & Booker, J. R. (1998, November). Theoretical solutions for calculating leakage through composite liner systems. *Geotechnical Research Centre Report*.

Sherard, J. L. (1985). The upstream zone in concrete-face rockfill dams. In J. B. Sherard (Ed.), *Symposium on Concrete Face Rockfill Dams - Design, Construction, and Performance*, (pp. 618-641).

SoilVision Systems Ltd. (2007). *SVFlux Users Manual.* Saskatoon.

Szabo, B., & Babuska, I. (1991). *Finite Element Analysis.* John Wiley & Sons, INC.

Touze-Foltz, N., & Giroud, J. (2003). Empirical equations for calculating the rate of liquid flow through composite liners due to geomembrane defects. *Geosynthetics International, 10*(6), 215-233.

Touze-Foltz, N., Rowe, R., & Duquennoi, C. (1999). Liquid Flow Through Composite Liners due to Geomembrane Defects: Analytical Solutions for Axi-Symmetric and Two-Dimensional Problems . *Geosynthetics International, 6*(6), 455-479.

Touze-Foltz, N., Rowe, R., & Navarro, N. (2001). Liquid flow through composite liners due to geomembrane defects: nonuniform hydraulic transmissivity at the liner interface. *Geosynthetics International*, 1-26.

van Genuchten, M. T. (1980). A closed form equation for predicting the hydraulic conductivity of unsaturated soils. *Soil Science Society of American Journal, 44*, 892-989.

Walton, J. C., & Sagar, B. (1990). Aspects of Fluid Flow through Small Flaws in Membrane Liners. *Environmental Science and Technology, 24*, 920-924.

Walton, J., Rahman, M., Casey, D., Picornell, M., & Johnson, F. (1997). Leakage through flaws in geomembrane liners. *Journal of Geotechnical and Geoenvironmental Engineering, 123*, 534-539.

Weber, C., & Zornberg, J. (2005). Leakage through Liners under High Hydraulic Heads. *Geosynthetics Research and Development in Progress*.

Zeng, Z., & Grigg, R. (2006). A criterion for non-darcy flow in porous media. *Transport in Porous Media, 63*, 57-69.

APPENDIX A: MATERIAL PROPERTIES

Table A.1 Grain Size Distribution of Sand

Sieve No.	Sieve Aperture (mm)	Percent Passing (%)
10	2.00	100
20	0.841	98
40	0.425	63
45	0.355	44
60	0.250	8
80	0.177	1
100	0.149	0
200	0.075	0

Table A.2 Soil Water Characteristic Values for Sand

Suction (kPa)	Volumetric Water Content
0.10	0.36
0.49	0.35
0.88	0.33
1.18	0.25
1.28	0.24
1.37	0.21
1.47	0.17
1.57	0.13
1.77	0.11
1.96	0.05
2.16	0.03
2.35	0.02
2.75	0.01

Table A.3 Soil Water Characteristic Values for Non-Woven Needle Punched Geotextile

Suction (kPa)	Volumetric Water Content
0.01	0.84
0.49	0.82
0.69	0.79
0.78	0.74
0.98	0.59
1.08	0.50
1.27	0.42
1.47	0.22
1.67	0.12
1.81	0.05
1.91	0.04
3.48	0.02
3.92	0.01

Table A.4 Sand and Geotextile Gradient Ratio Testing

Time (min)	Hydraulic Head Readings					Gradient Ratio
	Port 1	Port 2	Port 3	Port 4	Port 5	
0.5	8.2	13.2	18.4	22.7	27.0	0.96
15	8.1	13.4	19.0	22.7	26.5	0.95
20	8.1	13.5	18.9	22.7	26.9	1.00
25	8.2	13.6	18.8	22.8	26.9	1.04
30	8.2	13.6	18.7	22.9	27.1	1.06
35	8.2	13.7	18.7	22.9	27.0	1.10
60	8.2	13.6	18.7	22.9	27.1	1.06
120	8.2	13.6	18.9	22.9	27.1	1.02
Average						1.02

APPENDIX B: EXPERIMENTAL RESULTS

Table B.1 Experimental Results for a Circular Defect of Diameter 0.0015m with 60mil Geomembrane

Horizontal Hydraulic Gradient (m/m)	Hydraulic Head above Defect, h (m)	Flow Rate through Defect, Q (m^3/s)	Back Pressure (m)
0.000	0.121	4.39E-07	0
0.000	0.153	7.24E-07	0
0.000	0.192	7.72E-07	0
0.000	0.257	1.02E-06	0
0.000	0.262	1.14E-06	0
0.000	0.297	1.20E-06	0
0.000	0.301	1.37E-06	0
0.025	0.124	4.70E-07	0
0.025	0.173	6.81E-07	0
0.025	0.216	9.01E-07	0
0.025	0.265	1.17E-06	0
0.075	0.161	6.81E-07	0
0.075	0.221	9.51E-07	0
0.075	0.255	1.18E-06	0
0.075	0.302	1.42E-06	0
0.075	0.303	1.24E-06	0

Table B.2 Experimental Results for a Circular Defect of Diameter 0.0025m with 60mil Geomembrane

Horizontal Hydraulic Gradient (m/m)	Hydraulic Head above Defect, h (m)	Flow Rate through Defect, Q (m^3/s)	Back Pressure (m)
0.000	0.109	4.82E-07	0.00
0.000	0.109	5.36E-07	0.05
0.000	0.117	5.96E-07	0.02
0.000	0.154	9.04E-07	0.05
0.000	0.156	8.76E-07	0.02
0.000	0.161	8.68E-07	0.00
0.000	0.202	1.21E-06	0.05
0.000	0.204	1.11E-06	0.02
0.000	0.207	1.16E-06	0.00
0.000	0.231	1.30E-06	0.02
0.000	0.248	1.45E-06	0.00
0.000	0.295	1.67E-06	0.02
0.000	0.303	1.70E-06	0.05
0.000	0.325	1.96E-06	0.00
0.025	0.102	5.40E-07	0.02
0.025	0.106	4.57E-07	0.00
0.025	0.110	5.03E-07	0.05
0.025	0.153	8.18E-07	0.02
0.025	0.156	7.60E-07	0.00
0.025	0.161	8.59E-07	0.05
0.025	0.204	1.12E-06	0.02
0.025	0.207	1.22E-06	0.05
0.025	0.214	1.20E-06	0.00
0.025	0.246	1.33E-06	0.02
0.025	0.261	1.45E-06	0.05
0.025	0.264	1.56E-06	0.00
0.075	0.112	6.75E-07	0.05
0.075	0.128	6.55E-07	0.02
0.075	0.162	9.05E-07	0.00
0.075	0.170	8.84E-07	0.02
0.075	0.178	9.64E-07	0.05
0.075	0.212	1.10E-06	0.02
0.075	0.218	1.21E-06	0.05
0.075	0.226	1.22E-06	0.00
0.075	0.252	1.46E-06	0.05
0.075	0.263	1.36E-06	0.02
0.075	0.268	1.48E-06	0.00
0.075	0.288	1.56E-06	0.02

Table B.2 (Continued) Experimental Results for a Circular Defect of Diameter 0.0025m with 60mil Geomembrane

Horizontal Hydraulic Gradient (m/m)	Hydraulic Head above Defect, h (m)	Flow Rate through Defect, Q (m^3/s)	Back Pressure (m)
0.075	0.304	1.75E-06	0.00
0.075	0.305	1.67E-06	0.05
0.075	0.310	1.64E-06	0.02
0.075	0.314	1.69E-06	0.00
0.075	0.319	1.72E-06	0.05

Table B.3 Experimental Results for a Circular Defect of Diameter 0.0050m with 60mil Geomembrane

Horizontal Hydraulic Gradient (m/m)	Hydraulic Head above Defect, h (m)	Flow Rate through Defect, Q (m^3/s)	Back Pressure (m)
0.000	0.122	1.50E-06	0
0.000	0.157	1.73E-06	0
0.000	0.216	2.43E-06	0
0.000	0.257	3.05E-06	0
0.000	0.295	3.71E-06	0
0.025	0.119	1.37E-06	0
0.025	0.159	1.81E-06	0
0.025	0.214	2.35E-06	0
0.025	0.249	2.95E-06	0
0.075	0.167	2.09E-06	0
0.075	0.214	2.77E-06	0
0.075	0.265	3.42E-06	0
0.075	0.294	3.60E-06	0
0.075	0.307	3.97E-06	0

Table B.4 Experimental Results for a Circular Defect of Diameter 0.0050m with 80mil Geomembrane

Horizontal Hydraulic Gradient (m/m)	Hydraulic Head above Defect, h (m)	Flow Rate through Defect, Q (m^3/s)	Back Pressure (m)
0.000	0.112	7.50E-07	0
0.000	0.164	1.31E-06	0
0.000	0.216	1.97E-06	0
0.000	0.250	2.45E-06	0
0.000	0.289	3.04E-06	0
0.025	0.116	7.60E-07	0
0.025	0.174	1.54E-06	0
0.025	0.211	1.73E-06	0
0.025	0.258	2.23E-06	0
0.025	0.314	2.75E-06	0
0.075	0.162	1.34E-06	0
0.075	0.234	2.09E-06	0
0.075	0.265	2.54E-06	0
0.075	0.298	3.02E-06	0
0.075	0.305	2.82E-06	0

Table B.5 Experimental Results for a Circular Defect of Diameter 0.0050m with 120mil Geomembrane

Horizontal Hydraulic Gradient (m/m)	Hydraulic Head above Defect, h (m)	Flow Rate through Defect, Q (m^3/s)	Back Pressure (m)
0.000	0.110	5.66E-07	0
0.000	0.174	1.14E-06	0
0.000	0.209	1.44E-06	0
0.000	0.250	1.86E-06	0
0.000	0.323	2.76E-06	0
0.025	0.110	4.63E-07	0
0.025	0.167	9.99E-07	0
0.025	0.221	1.56E-06	0
0.025	0.259	2.05E-06	0
0.025	0.303	2.54E-06	0
0.075	0.179	1.37E-06	0
0.075	0.231	1.74E-06	0
0.075	0.268	1.84E-06	0
0.075	0.309	2.37E-06	0

Table B.6 Experimental Results for a Circular Defect of Diameter 0.0075m with 60mil Geomembrane

Horizontal Hydraulic Gradient (m/m)	Hydraulic Head above Defect, h (m)	Flow Rate through Defect, Q (m^3/s)	Back Pressure (m)
0.000	0.087	1.04E-06	0
0.000	0.121	1.90E-06	0
0.000	0.173	2.73E-06	0
0.000	0.197	3.04E-06	0
0.000	0.243	3.71E-06	0
0.025	0.102	1.25E-06	0
0.025	0.166	2.40E-06	0
0.025	0.206	2.93E-06	0
0.025	0.291	4.40E-06	0
0.075	0.157	2.14E-06	0
0.075	0.207	2.89E-06	0
0.075	0.254	3.62E-06	0
0.075	0.257	3.73E-06	0
0.075	0.285	4.25E-06	0
0.075	0.290	4.21E-06	0

Table B.7 Experimental Results for an Elongated Defect of Area 3.31E-05 m^2 with 60mil Geomembrane

Horizontal Hydraulic Gradient (m/m)	Hydraulic Head above Defect, h (m)	Flow Rate through Defect, Q (m^3/s)	Back Pressure (m)
0.000	0.120	2.05E-06	0
0.000	0.156	2.67E-06	0
0.000	0.204	3.60E-06	0
0.000	0.236	4.29E-06	0
0.000	0.285	5.27E-06	0
0.025	0.113	2.03E-06	0
0.025	0.162	2.86E-06	0
0.025	0.211	3.72E-06	0
0.025	0.257	4.54E-06	0
0.075	0.302	5.23E-06	0
0.075	0.163	3.30E-06	0
0.075	0.196	3.97E-06	0
0.075	0.248	4.92E-06	0
0.075	0.295	5.77E-06	0

Table B.8 Experimental Results for an Elongated Defect of Area 5.38E-05 m^2 with 60mil Geomembrane

Horizontal Hydraulic Gradient (m/m)	Hydraulic Head above Defect, h (m)	Flow Rate through Defect, Q (m^3/s)	Back Pressure (m)
0.000	0.125	3.43E-06	0
0.000	0.163	4.56E-06	0
0.000	0.190	5.43E-06	0
0.000	0.241	6.92E-06	0
0.000	0.287	8.33E-06	0
0.025	0.111	3.05E-06	0
0.025	0.157	4.47E-06	0
0.025	0.201	5.62E-06	0
0.025	0.243	6.94E-06	0
0.075	0.289	8.27E-06	0
0.075	0.152	4.48E-06	0
0.075	0.200	6.00E-06	0
0.075	0.235	7.10E-06	0
0.075	0.295	8.96E-06	0

Table B.9 Experimental Results for a Circular Defect of Diameter 0.0050m with Slope of 2.5% with 60mil Geomembrane

Horizontal Hydraulic Gradient (m/m)	Hydraulic Head above Defect, h (m)	Pressure Head above Defect, h_p (m)	Flow Rate through Defect, Q (m^3/s)	Back Pressure (m)
0.01	0.112	0.087	5.44E-07	0
0.01	0.133	0.108	7.35E-07	0
0.01	0.139	0.113	7.13E-07	0
0.01	0.141	0.116	7.03E-07	0
0.01	0.142	0.117	7.47E-07	0
0.01	0.147	0.122	7.80E-07	0
0.01	0.160	0.136	9.25E-07	0
0.00	0.125	0.099	5.12E-07	0
0.00	0.116	0.090	4.44E-07	0
0.00	0.108	0.082	3.83E-07	0

Table B.10 Experimental Results for a Circular Defect of Diameter 0.0050m with Slope of 5.0% with 60mil Geomembrane

Horizontal Hydraulic Gradient (m/m)	Hydraulic Head above Defect, h (m)	Pressure Head above Defect, h_p (m)	Flow Rate through Defect, Q (m^3/s)	Back Pressure (m)
0.01	0.111	0.061	3.60E-07	0
0.02	0.166	0.116	7.50E-07	0
0.01	0.156	0.106	6.60E-07	0
0.02	0.121	0.071	4.44E-07	0
0.02	0.112	0.062	3.76E-07	0
0.02	0.138	0.088	5.47E-07	0
0.00	0.174	0.122	5.89E-07	0
0.00	0.153	0.102	4.93E-07	0
0.00	0.136	0.086	4.07E-07	0

Table B.11 Experimental Results for a Circular Defect of Diameter 0.0050m with Slope of 10% with 60mil Geomembrane

Horizontal Hydraulic Gradient (m/m)	Hydraulic Head above Defect, h (m)	Pressure Head above Defect, h_p (m)	Flow Rate through Defect, Q (m^3/s)	Back Pressure (m)
0.03	0.157	0.057	2.88E-07	0
0.03	0.201	0.101	5.95E-07	0
0.03	0.189	0.089	5.08E-07	0
0.03	0.175	0.075	4.37E-07	0
0.00	0.259	0.160	7.74E-07	0
0.00	0.203	0.103	5.08E-07	0
0.00	0.181	0.081	4.05E-07	0

Table B.12 Experimental Head Readings for Circular Defects of Diameter 0.0015m Length-Wise in the Large-Scale Constant

Distance from Defect Located at 0 (m)	Manometer Head Reading (m)													
	Trial 1	Trial 2	Trial 3	Trial 4	Trial 5	Trial 6	Trial 7	Trial 8	Trial 9	Trial 10	Trial 12	Trial 13	Trial 14	Trial 15
-0.35	0.122	0.153	0.198	0.265	0.306	0.129	0.182	0.224	0.273	0.310	0.187	0.247	0.280	0.326
-0.15	0.120	0.152	0.194	0.262	0.304	0.125	0.176	0.219	0.266	0.306	0.166	0.224	0.261	0.310
-0.05	0.118	0.150	0.190	0.259	0.300	0.121	0.171	0.214	0.263	0.299	0.160	0.216	0.248	0.296
0.05	0.119	0.149	0.192	0.260	0.297	0.121	0.170	0.214	0.262	0.298	0.157	0.215	0.250	0.299
0.15	0.120	0.150	0.193	0.261	0.299	0.124	0.169	0.215	0.263	0.302	0.151	0.214	0.244	0.297
0.35	0.121	0.152	0.196	0.262	0.301	0.119	0.165	0.212	0.260	0.299	0.137	0.200	0.240	0.288

Table B.13 Experimental Head Readings for Circular Defects of Diameter 0.0015m Width-Wise in the Large-Scale Constant

Distance from Defect Located at 0 (m)	Manometer Head Reading (m)													
	Trial 1	Trial 2	Trial 3	Trial 4	Trial 5	Trial 6	Trial 7	Trial 8	Trial 9	Trial 10	Trial 12	Trial 13	Trial 14	Trial 15
-0.30	0.124	0.156	0.193	0.264	0.303	0.126	0.176	0.217	0.267	0.304	0.164	0.225	0.258	0.307
-0.15	0.123	0.155	0.192	0.263	0.301	0.125	0.175	0.216	0.266	0.303	0.163	0.223	0.257	0.306
-0.05	0.121	0.152	0.190	0.260	0.299	0.123	0.171	0.214	0.264	0.300	0.160	0.219	0.252	0.298
0.05	0.119	0.152	0.188	0.260	0.298	0.123	0.170	0.214	0.260	0.299	0.159	0.220	0.253	0.300
0.15	0.121	0.154	0.190	0.262	0.300	0.124	0.173	0.216	0.265	0.303	0.161	0.222	0.255	0.306
0.30	0.122	0.157	0.191	0.264	0.301	0.127	0.174	0.218	0.267	0.304	0.164	0.225	0.259	0.308

Table B.14 Experimental Head Readings for Circular Defects of Diameter 0.0025m (Back Pressure of 0.0m) Length-Wise in the Large-Scale Constant Head Apparatus

Distance from Defect Located at 0 (m)	Manometer Head Reading (m)													
	Trial 1	Trial 2	Trial 3	Trial 4	Trial 5	Trial 6	Trial 7	Trial 8	Trial 9	Trial 10	Trial 12	Trial 13	Trial 14	Trial 15
-0.35	0.111	0.159	0.205	0.248	0.328	0.112	0.163	0.218	0.274	0.313	0.181	0.246	0.288	0.334
-0.15	0.110	0.158	0.204	0.246	0.326	0.110	0.160	0.216	0.269	0.306	0.171	0.237	0.276	0.323
-0.05	0.108	0.157	0.201	0.244	0.324	0.105	0.154	0.210	0.257	0.296	0.160	0.224	0.264	0.311
0.05	0.110	0.161	0.207	0.247	0.329	0.095	0.149	0.210	0.258	0.299	0.143	0.209	0.249	0.295
0.15	0.109	0.160	0.206	0.246	0.326	0.101	0.155	0.214	0.266	0.302	0.156	0.221	0.262	0.306
0.35	0.107	0.158	0.204	0.246	0.324	0.106	0.157	0.216	0.263	0.301	0.162	0.224	0.264	0.311

Table B.15 Experimental Head Readings for Circular Defects of Diameter 0.0025m (Back Pressure of 0.0m) Width-Wise in the Large-Scale Constant Head Apparatus

Distance from Defect Located at 0 (m)	Manometer Head Reading (m)													
	Trial 1	Trial 2	Trial 3	Trial 4	Trial 5	Trial 6	Trial 7	Trial 8	Trial 9	Trial 10	Trial 12	Trial 13	Trial 14	Trial 15
-0.30	0.111	0.164	0.211	0.253	0.325	0.110	0.157	0.216	0.268	0.306	0.161	0.226	0.270	0.316
-0.15	0.110	0.163	0.210	0.251	0.324	0.108	0.156	0.215	0.265	0.304	0.160	0.225	0.269	0.314
-0.05	0.109	0.162	0.208	0.250	0.322	0.105	0.152	0.210	0.257	0.302	0.159	0.222	0.263	0.310
0.05	0.107	0.160	0.207	0.246	0.323	0.104	0.153	0.211	0.259	0.302	0.161	0.224	0.265	0.312
0.15	0.108	0.161	0.209	0.247	0.324	0.106	0.157	0.214	0.264	0.307	0.163	0.227	0.270	0.314
0.30	0.109	0.163	0.211	0.249	0.326	0.110	0.159	0.216	0.266	0.309	0.165	0.229	0.271	0.316

Table B.16 Experimental Head Readings for Circular Defects of Diameter 0.0025m (Back Pressure of 0.02m) Length-Wise in the Large-Scale Constant Head Apparatus

Distance from Defect Located at 0 (m)	Manometer Head Reading (m)														
	Trial 1	Trial 2	Trial 3	Trial 4	Trial 5	Trial 6	Trial 7	Trial 8	Trial 9	Trial 10	Trial 11	Trial 12	Trial 13	Trial 14	Trial 15
-0.35	0.119	0.157	0.210	0.245	0.298	0.111	0.162	0.213	0.253	0.299	0.143	0.191	0.230	0.277	0.320
-0.15	0.118	0.156	0.206	0.241	0.295	0.107	0.157	0.207	0.247	0.294	0.134	0.180	0.220	0.270	0.314
-0.05	0.117	0.152	0.200	0.229	0.293	0.098	0.150	0.202	0.241	0.285	0.126	0.170	0.210	0.262	0.308
0.05	0.120	0.158	0.208	0.224	0.291	0.105	0.144	0.198	0.242	0.280	0.114	0.147	0.195	0.246	0.282
0.15	0.118	0.157	0.204	0.226	0.295	0.099	0.150	0.202	0.245	0.284	0.124	0.164	0.206	0.259	0.300
0.35	0.116	0.150	0.201	0.227	0.296	0.098	0.151	0.204	0.245	0.286	0.125	0.169	0.209	0.261	0.305

Table B.17 Experimental Head Readings for Circular Defects of Diameter 0.0025m (Back Pressure of 0.02m) Width-Wise in the Large-Scale Constant Head Apparatus

Distance from Defect Located at 0 (m)	Manometer Head Reading (m)														
	Trial 1	Trial 2	Trial 3	Trial 4	Trial 5	Trial 6	Trial 7	Trial 8	Trial 9	Trial 10	Trial 11	Trial 12	Trial 13	Trial 14	Trial 15
-0.35	0.118	0.160	0.203	0.233	0.298	0.103	0.153	0.206	0.247	0.290	0.128	0.171	0.213	0.265	0.319
-0.15	0.117	0.159	0.202	0.232	0.297	0.102	0.152	0.205	0.246	0.287	0.127	0.170	0.212	0.264	0.317
-0.05	0.115	0.156	0.200	0.228	0.293	0.100	0.151	0.202	0.241	0.284	0.125	0.167	0.209	0.260	0.310
0.05	0.114	0.156	0.201	0.224	0.291	0.100	0.152	0.203	0.244	0.285	0.127	0.169	0.210	0.260	0.311
0.15	0.116	0.157	0.203	0.233	0.296	0.102	0.154	0.205	0.247	0.287	0.129	0.172	0.212	0.266	0.313
0.35	0.117	0.158	0.204	0.234	0.298	0.104	0.155	0.206	0.248	0.289	0.130	0.175	0.214	0.268	0.319

Table B.18 Experimental Head Readings for Circular Defects of Diameter 0.0025m (Back Pressure of 0.05m) Length-Wise in the Large-Scale Constant Head Apparatus

Distance from Defect Located at 0 (m)	Manometer Head Reading (m)														
	Trial 1	Trial 2	Trial 3	Trial 4	Trial 5	Trial 6	Trial 7	Trial 8	Trial 9	Trial 10	Trial 11	Trial 12	Trial 13	Trial 14	Trial 15
-0.35	0.109	0.155	0.206	0.276	0.308	0.120	0.166	0.212	0.272	0.314	0.130	0.196	0.238	0.272	0.336
-0.15	0.108	0.154	0.202	0.274	0.306	0.115	0.164	0.209	0.266	0.307	0.119	0.186	0.228	0.261	0.326
-0.05	0.106	0.152	0.198	0.273	0.297	0.111	0.159	0.204	0.258	0.299	0.110	0.177	0.216	0.249	0.315
0.05	0.110	0.156	0.200	0.275	0.304	0.099	0.157	0.203	0.253	0.300	0.094	0.159	0.201	0.235	0.308
0.15	0.110	0.155	0.197	0.274	0.302	0.106	0.158	0.207	0.256	0.303	0.105	0.173	0.211	0.246	0.315
0.35	0.109	0.154	0.195	0.272	0.300	0.110	0.160	0.206	0.257	0.304	0.110	0.175	0.215	0.250	0.318

Table B.19 Experimental Head Readings for Circular Defects of Diameter 0.0025m (Back Pressure of 0.05m) Width-Wise in the Large-Scale Constant Head Apparatus

Distance from Defect Located at 0 (m)	Manometer Head Reading (m)														
	Trial 1	Trial 2	Trial 3	Trial 4	Trial 5	Trial 6	Trial 7	Trial 8	Trial 9	Trial 10	Trial 11	Trial 12	Trial 13	Trial 14	Trial 15
-0.35	0.111	0.155	0.206	0.272	0.306	0.111	0.163	0.209	0.263	0.307	0.112	0.180	0.218	0.254	0.320
-0.15	0.110	0.154	0.205	0.271	0.305	0.110	0.162	0.207	0.262	0.306	0.111	0.179	0.216	0.253	0.319
-0.05	0.109	0.152	0.204	0.267	0.302	0.109	0.159	0.203	0.260	0.303	0.109	0.177	0.215	0.249	0.311
0.05	0.108	0.156	0.201	0.270	0.301	0.109	0.160	0.204	0.258	0.303	0.111	0.177	0.216	0.250	0.315
0.15	0.109	0.155	0.204	0.273	0.303	0.111	0.161	0.207	0.260	0.306	0.113	0.179	0.218	0.252	0.321
0.35	0.110	0.154	0.205	0.275	0.305	0.112	0.162	0.210	0.261	0.307	0.114	0.182	0.221	0.255	0.322

Table B.20 Experimental Head Readings for Circular Defects of Diameter 0.0050m on 60mil Geomembrane Length-Wise in the Large-Scale Constant Head Apparatus

Distance from Defect Located at 0 (m)	Manometer Head Reading (m)														
	Trial 1	Trial 2	Trial 3	Trial 4	Trial 5	Trial 6	Trial 7	Trial 8	Trial 9	Trial 10	Trial 11	Trial 12	Trial 13	Trial 14	Trial 15
-0.35	0.126	0.166	0.216	0.262	0.302	0.120	0.168	0.222	0.261	0.306	0.185	0.234	0.283	0.320	0.126
-0.15	0.124	0.164	0.215	0.256	0.298	0.118	0.160	0.217	0.255	0.297	0.172	0.221	0.271	0.311	0.124
-0.05	0.119	0.160	0.212	0.250	0.290	0.114	0.155	0.210	0.246	0.288	0.166	0.213	0.263	0.301	0.119
0.05	0.123	0.166	0.215	0.266	0.298	0.110	0.147	0.212	0.244	0.289	0.150	0.195	0.247	0.291	0.123
0.15	0.120	0.166	0.217	0.263	0.296	0.114	0.154	0.214	0.249	0.290	0.160	0.207	0.258	0.301	0.120
0.35	0.116	0.161	0.212	0.250	0.292	0.115	0.153	0.207	0.246	0.283	0.162	0.205	0.253	0.299	0.116

Table B.21 Experimental Head Readings for Circular Defects of Diameter 0.0050m on 60mil Geomembrane Width-Wise in the Large-Scale Constant Head Apparatus

Distance from Defect Located at 0 (m)	Manometer Head Reading (m)														
	Trial 1	Trial 2	Trial 3	Trial 4	Trial 5	Trial 6	Trial 7	Trial 8	Trial 9	Trial 10	Trial 11	Trial 12	Trial 13	Trial 14	Trial 15
-0.35	0.125	0.168	0.221	0.260	0.300	0.120	0.163	0.217	0.255	0.298	0.170	0.219	0.270	0.313	0.125
-0.15	0.123	0.165	0.220	0.258	0.297	0.117	0.162	0.215	0.253	0.296	0.169	0.218	0.268	0.311	0.123
-0.05	0.120	0.160	0.214	0.249	0.291	0.112	0.156	0.210	0.240	0.287	0.165	0.210	0.261	0.300	0.120
0.05	0.120	0.162	0.213	0.247	0.290	0.111	0.155	0.208	0.238	0.290	0.164	0.208	0.259	0.299	0.120
0.15	0.124	0.166	0.219	0.259	0.294	0.116	0.164	0.216	0.250	0.300	0.168	0.220	0.272	0.310	0.124
0.35	0.125	0.167	0.221	0.261	0.296	0.119	0.165	0.217	0.253	0.302	0.170	0.221	0.273	0.313	0.125

Table B.22 Experimental Head Readings for Circular Defects of Diameter 0.0050m on 80mil Geomembrane Length-Wise in the Large-Scale Constant Head Apparatus

Distance from Defect Located at 0 (m)	Manometer Head Reading (m)														
	Trial 1	Trial 2	Trial 3	Trial 4	Trial 5	Trial 6	Trial 7	Trial 8	Trial 9	Trial 10	Trial 11	Trial 12	Trial 13	Trial 14	Trial 15
-0.35	0.113	0.170	0.221	0.254	0.298	0.125	0.180	0.220	0.267	0.321	0.180	0.259	0.286	0.334	0.113
-0.15	0.112	0.166	0.218	0.252	0.293	0.120	0.175	0.214	0.263	0.316	0.168	0.244	0.272	0.316	0.112
-0.05	0.110	0.158	0.212	0.244	0.280	0.113	0.170	0.209	0.255	0.309	0.161	0.232	0.261	0.301	0.110
0.05	0.114	0.169	0.219	0.252	0.296	0.112	0.166	0.203	0.248	0.308	0.148	0.218	0.252	0.281	0.114
0.15	0.112	0.163	0.215	0.248	0.293	0.115	0.175	0.211	0.259	0.316	0.158	0.229	0.262	0.300	0.112
0.35	0.109	0.158	0.212	0.244	0.282	0.113	0.173	0.208	0.255	0.312	0.160	0.228	0.259	0.297	0.109

Table B.23 Experimental Head Readings for Circular Defects of Diameter 0.0050m on 80mil Geomembrane Width-Wise in the Large-Scale Constant Head Apparatus

Distance from Defect Located at 0 (m)	Manometer Head Reading (m)														
	Trial 1	Trial 2	Trial 3	Trial 4	Trial 5	Trial 6	Trial 7	Trial 8	Trial 9	Trial 10	Trial 11	Trial 12	Trial 13	Trial 14	Trial 15
-0.35	0.113	0.166	0.219	0.254	0.293	0.117	0.178	0.213	0.260	0.316	0.163	0.237	0.266	0.309	0.113
-0.15	0.111	0.165	0.218	0.252	0.290	0.115	0.176	0.212	0.259	0.315	0.162	0.235	0.264	0.307	0.111
-0.05	0.109	0.159	0.210	0.248	0.281	0.114	0.171	0.209	0.256	0.310	0.160	0.230	0.260	0.299	0.109
0.05	0.110	0.160	0.209	0.246	0.282	0.113	0.169	0.209	0.255	0.309	0.159	0.229	0.259	0.298	0.110
0.15	0.113	0.164	0.216	0.251	0.290	0.117	0.175	0.211	0.258	0.315	0.162	0.235	0.266	0.308	0.113
0.35	0.114	0.165	0.219	0.253	0.294	0.118	0.176	0.212	0.260	0.316	0.163	0.236	0.267	0.310	0.114

Table B.24 Experimental Head Readings for Circular Defects of Diameter 0.0050m on 120mil Geomembrane Length-Wise in the Large-Scale Constant Head Apparatus

Distance from Defect Located at 0 (m)	Manometer Head Reading (m)														
	Trial 1	Trial 2	Trial 3	Trial 4	Trial 5	Trial 6	Trial 7	Trial 8	Trial 9	Trial 10	Trial 11	Trial 12	Trial 13	Trial 14	Trial 15
-0.35	0.114	0.176	0.210	0.253	0.325	0.123	0.173	0.228	0.270	0.314	0.190	0.250	0.290	0.335	0.114
-0.15	0.110	0.175	0.208	0.251	0.323	0.120	0.169	0.223	0.265	0.309	0.188	0.238	0.274	0.320	0.110
-0.05	0.109	0.173	0.207	0.246	0.320	0.115	0.165	0.218	0.254	0.295	0.173	0.230	0.262	0.307	0.109
0.05	0.114	0.175	0.211	0.253	0.326	0.100	0.164	0.217	0.241	0.287	0.161	0.215	0.252	0.291	0.114
0.15	0.111	0.174	0.209	0.252	0.324	0.105	0.167	0.221	0.257	0.304	0.165	0.219	0.259	0.301	0.111
0.35	0.109	0.172	0.206	0.245	0.320	0.113	0.165	0.218	0.251	0.296	0.171	0.225	0.263	0.302	0.109

Table B.25 Experimental Head Readings for Circular Defects of Diameter 0.0050m on 120mil Geomembrane Width-Wise in the Large-Scale Constant Head Apparatus

Distance from Defect Located at 0 (m)	Manometer Head Reading (m)														
	Trial 1	Trial 2	Trial 3	Trial 4	Trial 5	Trial 6	Trial 7	Trial 8	Trial 9	Trial 10	Trial 11	Trial 12	Trial 13	Trial 14	Trial 15
-0.35	0.111	0.175	0.213	0.253	0.325	0.113	0.169	0.223	0.264	0.308	0.180	0.230	0.270	0.310	0.111
-0.15	0.109	0.174	0.210	0.250	0.323	0.108	0.167	0.220	0.262	0.306	0.176	0.228	0.265	0.308	0.109
-0.05	0.108	0.172	0.208	0.249	0.320	0.102	0.165	0.218	0.257	0.303	0.170	0.226	0.261	0.305	0.108
0.05	0.107	0.171	0.208	0.250	0.319	0.103	0.166	0.217	0.257	0.302	0.170	0.227	0.263	0.305	0.107
0.15	0.109	0.173	0.210	0.251	0.325	0.108	0.168	0.221	0.263	0.306	0.173	0.229	0.268	0.309	0.109
0.35	0.110	0.175	0.212	0.252	0.326	0.113	0.170	0.222	0.264	0.309	0.175	0.230	0.270	0.310	0.110

Table B.26 Experimental Head Readings for Circular Defects of Diameter 0.0075m Length-Wise in the Large-Scale Constant Head Apparatus

Distance from Defect Located at 0 (m)	Manometer Head Reading (m)													
	Trial 1	Trial 2	Trial 3	Trial 4	Trial 5	Trial 6	Trial 7	Trial 8	Trial 9	Trial 10	Trial 12	Trial 13	Trial 14	Trial 15
-0.35	0.124	0.183	0.208	0.254	0.304	0.110	0.184	0.230	0.274	0.304	0.186	0.235	0.284	0.309
-0.15	0.122	0.172	0.201	0.246	0.296	0.106	0.175	0.212	0.262	0.293	0.168	0.218	0.265	0.297
-0.05	0.116	0.168	0.192	0.236	0.283	0.100	0.130	0.199	0.251	0.278	0.155	0.205	0.249	0.284
0.05	0.125	0.174	0.199	0.244	0.294	0.094	0.163	0.198	0.249	0.277	0.136	0.190	0.234	0.278
0.15	0.122	0.171	0.197	0.243	0.293	0.100	0.168	0.202	0.254	0.281	0.150	0.200	0.246	0.285
0.35	0.116	0.169	0.190	0.236	0.283	0.098	0.164	0.197	0.246	0.276	0.148	0.199	0.244	0.280

Table B.27 Experimental Head Readings for Circular Defects of Diameter 0.0075m Width-Wise in the Large-Scale Constant Head Apparatus

Distance from Defect Located at 0 (m)	Manometer Head Reading (m)													
	Trial 1	Trial 2	Trial 3	Trial 4	Trial 5	Trial 6	Trial 7	Trial 8	Trial 9	Trial 10	Trial 12	Trial 13	Trial 14	Trial 15
-0.30	0.123	0.176	0.199	0.247	0.295	0.106	0.174	0.210	0.262	0.291	0.160	0.209	0.258	0.295
-0.15	0.123	0.175	0.198	0.246	0.294	0.104	0.173	0.210	0.261	0.290	0.158	0.208	0.257	0.294
-0.05	0.118	0.169	0.192	0.235	0.282	0.101	0.164	0.199	0.251	0.277	0.153	0.202	0.249	0.282
0.05	0.115	0.167	0.188	0.233	0.279	0.099	0.160	0.201	0.253	0.277	0.151	0.199	0.241	0.282
0.15	0.120	0.174	0.198	0.244	0.291	0.104	0.168	0.204	0.256	0.286	0.160	0.208	0.255	0.293
0.30	0.122	0.178	0.200	0.247	0.295	0.106	0.171	0.207	0.259	0.289	0.162	0.210	0.260	0.296

Table B.28 Experimental Head Readings for Elongated Defects of Area 2.4E-05m^2 Length-Wise in the Large-Scale Constant Head Apparatus

Distance from Defect Located at 0 (m)	Manometer Head Reading (m)													
	Trial 1	Trial 2	Trial 3	Trial 4	Trial 5	Trial 6	Trial 7	Trial 8	Trial 9	Trial 10	Trial 12	Trial 13	Trial 14	Trial 15
-0.35	0.127	0.162	0.212	0.249	0.295	0.126	0.175	0.225	0.273	0.324	0.196	0.225	0.280	0.334
-0.15	0.121	0.158	0.206	0.237	0.283	0.119	0.167	0.216	0.263	0.310	0.174	0.207	0.261	0.311
-0.05	0.114	0.153	0.196	0.226	0.273	0.108	0.156	0.203	0.248	0.295	0.160	0.192	0.241	0.287
0.05	0.128	0.162	0.211	0.250	0.295	0.105	0.158	0.209	0.257	0.299	0.140	0.180	0.229	0.272
0.15	0.120	0.159	0.206	0.237	0.287	0.112	0.162	0.212	0.258	0.302	0.156	0.191	0.240	0.286
0.35	0.115	0.152	0.197	0.224	0.277	0.109	0.157	0.203	0.250	0.292	0.158	0.188	0.235	0.281

Table B.29 Experimental Head Readings for Elongated Defects of Area 2.4E-05m^2 Width-Wise in the Large-Scale Constant Head Apparatus

Distance from Defect Located at 0 (m)	Manometer Head Reading (m)													
	Trial 1	Trial 2	Trial 3	Trial 4	Trial 5	Trial 6	Trial 7	Trial 8	Trial 9	Trial 10	Trial 12	Trial 13	Trial 14	Trial 15
-0.30	0.123	0.159	0.207	0.240	0.291	0.117	0.167	0.216	0.263	0.308	0.167	0.202	0.255	0.303
-0.15	0.120	0.154	0.204	0.234	0.285	0.113	0.162	0.214	0.258	0.304	0.165	0.198	0.251	0.299
-0.05	0.113	0.149	0.195	0.226	0.274	0.108	0.154	0.202	0.247	0.289	0.151	0.184	0.237	0.281
0.05	0.114	0.150	0.197	0.227	0.277	0.110	0.157	0.203	0.249	0.291	0.152	0.185	0.238	0.282
0.15	0.119	0.156	0.207	0.235	0.288	0.115	0.163	0.215	0.259	0.306	0.165	0.200	0.252	0.298
0.30	0.122	0.160	0.210	0.241	0.293	0.118	0.167	0.217	0.264	0.309	0.167	0.202	0.256	0.305

Table B.30 Experimental Head Readings for Elongated Defects of Area 4.8E-05m^2 Length-Wise in the Large-Scale Constant Head Apparatus

Distance from Defect Located at 0 (m)	Manometer Head Reading (m)													
	Trial 1	Trial 2	Trial 3	Trial 4	Trial 5	Trial 6	Trial 7	Trial 8	Trial 9	Trial 10	Trial 12	Trial 13	Trial 14	Trial 15
-0.35	0.130	0.170	0.203	0.254	0.300	0.125	0.170	0.217	0.262	0.310	0.183	0.231	0.268	0.339
-0.15	0.126	0.164	0.194	0.244	0.289	0.118	0.162	0.207	0.251	0.301	0.164	0.214	0.247	0.313
-0.05	0.120	0.158	0.176	0.228	0.269	0.104	0.152	0.190	0.228	0.263	0.139	0.190	0.215	0.276
0.05	0.131	0.169	0.202	0.253	0.300	0.103	0.147	0.202	0.245	0.285	0.137	0.188	0.229	0.283
0.15	0.126	0.165	0.195	0.243	0.290	0.108	0.156	0.199	0.247	0.287	0.146	0.196	0.233	0.289

Table B.31 Experimental Head Readings for Elongated Defects of Area 4.8E-05m^2 Width-Wise in the Large-Scale Constant Head Apparatus

Distance from Defect Located at 0 (m)	Manometer Head Reading (m)													
	Trial 1	Trial 2	Trial 3	Trial 4	Trial 5	Trial 6	Trial 7	Trial 8	Trial 9	Trial 10	Trial 12	Trial 13	Trial 14	Trial 15
-0.30	0.128	0.170	0.196	0.250	0.302	0.118	0.162	0.208	0.248	0.300	0.159	0.209	0.245	0.310
-0.15	0.124	0.164	0.190	0.240	0.290	0.113	0.157	0.204	0.242	0.292	0.154	0.201	0.235	0.300
-0.05	0.118	0.152	0.176	0.229	0.270	0.104	0.152	0.194	0.231	0.283	0.142	0.185	0.220	0.273
0.05	0.119	0.153	0.186	0.236	0.276	0.103	0.153	0.195	0.233	0.284	0.143	0.187	0.221	0.272
0.15	0.126	0.166	0.192	0.242	0.291	0.114	0.156	0.205	0.243	0.291	0.156	0.200	0.240	0.301
0.30	0.129	0.172	0.197	0.250	0.299	0.117	0.163	0.208	0.249	0.299	0.161	0.210	0.246	0.310

APPENDIX C: FINITE ELEMENT RESULTS

Table C.1 Finite Element Modelling Results for GeoSlope 2-Dimensional Axisymmetric Analysis of Circular Defects

Defect Area, a (m^2)	Hydraulic Head above Defect, h (m)	SEEP/W Flow Rate (m^3/s)
1.77E-06	0.1	5.14E-07
	0.2	1.03E-06
	0.3	1.55E-06
4.91E-06	0.1	8.33E-07
	0.2	1.67E-06
	0.3	2.50E-06
1.96E-05	0.1	1.63E-06
	0.2	3.26E-06
	0.3	4.90E-06
4.42E-05	0.1	2.41E-06
	0.2	4.85E-06
	0.3	7.28E-06

Table C.2 Finite Element Modelling Results for SoilVision 2-Dimensional Axisymmetric Analysis of Circular Defects

Defect Area, a (m^2)	Hydraulic Head above Defect, h (m)	SVFLUX Flow Rate (m^3/s)
1.17E-06	0.1	4.25E-07
	0.2	8.50E-07
	0.3	1.27E-06
2.63E-06	0.1	6.09E-07
	0.2	1.22E-06
	0.3	1.83E-06
4.67E-06	0.1	8.10E-07
	0.2	1.62E-06
	0.3	2.44E-06
1.96E-05	0.1	1.61E-06
	0.2	3.23E-06
	0.3	4.87E-06
4.42E-05	0.1	2.35E-06
	0.2	4.73E-06
	0.3	7.11E-06

Table C.3 Finite Element Modelling Results for 3-Dimensional SVFLUX/GE Analysis of Circular Defects

Defect Area, a (m^2)	Hydraulic Head above Defect, h (m)	Hydraulic Conductivity of Sand		
		k=0.0013m/s	k=0.0016m/s	k=0.0018m/s
		Flow Rate (m^3/s)	Flow Rate (m^3/s)	Flow Rate (m^3/s)
1.17E-06	0.10	2.23E-07	2.75E-07	3.09E-07
	0.15		4.14E-07	
	0.20	4.49E-07	5.52E-07	6.22E-07
	0.25		6.91E-07	
	0.30	6.75E-07	8.30E-07	9.34E-07
4.67E-05	0.10	4.38E-07	5.38E-07	6.05E-07
	0.15		8.07E-07	
	0.20	8.75E-07	1.08E-06	1.21E-06
	0.25		1.35E-06	
	0.30	1.31E-06	1.61E-06	1.82E-06
1.81E-05	0.10	8.75E-07	1.08E-06	1.21E-06
	0.15		1.62E-06	
	0.20	1.75E-06	2.16E-06	2.43E-06
	0.25		2.70E-06	
	0.30	2.63E-06	3.24E-06	3.64E-06
4.19E-05	0.10	1.42E-06	1.75E-06	1.97E-06
	0.15		2.65E-06	
	0.20	2.88E-06	3.54E-06	3.99E-06
	0.25		4.44E-06	
	0.30	4.35E-06	5.34E-06	6.02E-06
5.03E-05	0.10	1.49E-06	1.89E-06	2.07E-06
	0.15		2.89E-06	4.14E-06
	0.20	2.99E-06	3.89E-06	
	0.25		4.86E-06	
	0.30	4.49E-06	5.83E-06	6.22E-06

Table C.4 Scaled-Up Finite Element Modelling Results for 3-Dimensional SVFLUX/GE Analysis of Circular Defects

Defect Area, a (m^2)	Hydraulic Head above Defect, h (m)	Scaled-Up Flow Rate (m^3/s)
1.54E-04	1.0	3.59E-05
	2.0	7.11E-05
	3.0	1.06E-04
4.52E-04	1.0	5.27E-05
	2.0	1.06E-04
	3.0	1.59E-04
1.81E-04	1.0	1.09E-04
	2.0	2.19E-04
	3.0	3.30E-04
2.83E-03	1.0	1.41E-04
	2.0	2.84E-04
	3.0	4.27E-04
4.54E-03	1.0	1.52E-04
	2.0	3.28E-04
	3.0	5.04E-04

Table C.5 Finite Element Modelling Results for 3-Dimensional SVFLUX/GE Analysis of Circular Defect of Diameter 0.0048m with Geomembrane Thickness Region

Geomembrane Thickness	Hydraulic Head above Defect, h (m)	Flow Rate through Defect, Q (m^3/s)
60 mil	0.10	4.46E-07
	0.20	8.94E-07
	0.30	1.34E-06
80 mil	0.10	4.01E-07
	0.20	8.10E-07
	0.30	1.22E-06
120 mil	0.10	3.52E-07
	0.20	7.05E-07
	0.30	1.06E-06

Table C.6 Finite Element Modelling Results for 3-Dimensional SVFLUX/GE Analysis of Elongated Defects

Defect Area, a (m^2)	Hydraulic Head above Defect, h (m)	Hydraulic Conductivity of Sand		
		k=0.0013m/s	k=0.0016m/s	k=0.0018m/s
		Flow Rate (m^3/s)	Flow Rate (m^3/s)	Flow Rate (m^3/s)
3.20E-05	0.10	1.27E-06	1.56E-06	1.75E-06
	0.20	2.58E-06	3.17E-06	3.57E-06
	0.30	3.89E-06	4.78E-06	5.38E-06
5.20E-05	0.10	1.78E-06	2.19E-06	2.46E-06
	0.20	3.57E-06	4.40E-06	4.95E-06
	0.30	5.37E-06	6.61E-06	7.43E-06
5.40E-05	0.10	1.86E-06	2.26E-06	2.54E-06
	0.20	3.69E-06	4.50E-06	5.08E-06
	0.30	5.51E-06	6.75E-06	7.62E-06

Table C.7 Scaled-Up Finite Element Modelling Results for 3-Dimensional SVFLUX/GE Analysis of Elongated Defects

Defect Area, a (m^2)	Hydraulic Head above Defect, h (m)	Hydraulic Conductivity of Sand k=0.0016m/s
		Flow Rate (m^3/s)
2.40E-03	1.0	1.39E-04
	2.0	2.80E-04
	3.0	4.20E-04
4.80E-03	1.0	2.61E-04
	2.0	5.49E-04
	3.0	8.37E-04
4.80E-03	1.0	2.51E-04
	2.0	5.33E-04
	3.0	8.15E-04

Table C.8 Finite Element Modelling Results for 3-Dimensional SVFLUX/GE Analysis of Circular Defects on Sloped Geomembrane Surfaces

Slope (%)	Hydraulic Head above Defect, h (m)	Horizontal Hydraulic Gradient (m/m)	Flow Rate through Defect, Q (m^3/s)
2.5	0.087	0.01	7.42E-07
2.5	0.108	0.01	8.13E-07
2.5	0.114	0.01	9.23E-07
2.5	0.116	0.01	7.43E-07
2.5	0.117	0.01	9.42E-07
2.5	0.122	0.01	1.03E-06
2.5	0.135	0.01	1.02E-06
2.5	0.083	0.00	1.13E-06
2.5	0.091	0.00	1.10E-06
2.5	0.100	0.00	1.27E-06
5.0	0.071	0.02	4.09E-07
5.0	0.088	0.01	6.18E-07
5.0	0.106	0.01	6.65E-07
5.0	0.116	0.02	7.31E-07
5.0	0.086	0.00	4.69E-07
5.0	0.103	0.00	6.69E-07
5.0	0.124	0.00	8.66E-07
10	0.057	0.03	4.46E-07
10	0.075	0.03	7.57E-07
10	0.101	0.03	4.03E-07
10	0.081	0.00	3.95E-07
10	0.103	0.00	6.32E-07
10	0.16	0.00	9.87E-07